MAJOR MERGERS BETWEEN GALAXIES
Their Role in the High-Redshift Universe
and
Two Nearby Cases Studies

DISSERTATION

der Fakultät für Physik
der Ludwig-Maximilians-Universität München
zur Erlangung des Grades
Doktor der Naturwissenschaften
Dr. rer. nat.

vorgelegt von
Hauke Engel
aus Troisdorf

September 2010

Für meine Eltern.

The effort to understand the universe is one of the very few things that lifts human life a little above the level of farce, and gives it some of the grace of tragedy.
        –Steven Weinberg

Zusammenfassung

Eine der grundlegenden Fragen, deren Beantwortung sich Astrophysiker verschrieben haben, ist zu verstehen, wie sich Galaxien im Laufe der Zeit verändern. Ein wichtiger Prozess in diesem Zusammenhang ist die gegenseitige Anziehung und das schlussendliche Verschmelzen von zwei Galaxien ähnlicher Masse ('major merger' im Englischen). Solche Zusammenstöße und daraus resultierendes Verschmelzen von gasreichen Spiralgalaxien im Besonderen werden für das Auslösen von Phasen hoher Sternentstehungsraten ('star bursts'), Quasaren, und die Entstehung von elliptischen Galaxien verantwortlich gehalten. Unser Verständnis der Details dieser Verschmelzungsvorgänge, und der Rolle, welche diese Prozesse im jungen (hochrotverschobenen) Universum spielen, ist momentan jedoch noch sehr unvollständig.

Das Ziel dieser Dissertation ist es, zur Klärung dieser Fragen einen Beitrag zu leisten. Hierzu benutzen wir mit Hilfe adaptiver Optik gewonnene nahinfrarote Integralfeldspektroskopie- und Bilddaten und Millimeterwellenlängen-Interferometrie-Daten von zwei lokalen, prototypischen major mergers und von einer Anzahl von submillimeterwellenlängen-leuchtstarken hochrotverschobenen Galaxien ('SMGs' im Folgenden).

Nach einem einführenden Überblick über das Feld (Kapitel 1) und benutzte Techniken (Kapitel 2), gehen wir in Kapitel 3 der Frage nach, welche Vorgänge die außerordentlichen Helligkeiten von SMGs auslösen. Wir analysieren hochaufgelöste interferometrische CO-Linien-Beobachtungen von zwölf SMGs (für vier von diesen werten wir neue, vormals unpublizierte Daten aus), und zeigen, dass mindestens acht dieser Systeme morphologische und kinematische Signaturen von Kollisions- und Verschmelzungsprozessen aufweisen. Das Masseverhältnis von jenen Systemen, die aus zwei interagierenden Galaxien bestehen, ist 1:3 oder geringer, d.h. diese sind major mergers. Dann erörtern wir die Frage, inwieweit lokale $L_{IR} \geq 10^{12} L_\odot$- und hochrotverschobene $S_{850\mu m}$-selektierte major mergers die gleichen Kollisions- und Verschmelzungsphasen durchmustern, und vergleichen ihre jeweiligen Verhältnisse von binären zu bereits verschmolzenen Systemen. Daraus folgern wir, dass die meisten, wenn nicht gar alle, jener unserer SMGs, die morphologisch und kinematisch entweder isolierte Scheibengalaxien oder bereits verschmolzene major mergers sein könnten, in der Tat ebenfalls major mergers sein müssen. Weiterhin vergleichen wir die dynamischen Massen und Gasmassen unserer SMGs mit publizierten stellaren Massen verschiedener Autoren, und zeigen, dass unsere Daten die stellaren Massen am unteren Ende der publizierten Werte bestätigen. Dies wiederum unterstützt kosmologische Modelle, in denen SMGs durch major mergers entstehen. Zusammenfassend können wir also überzeugend zeigen, dass die meisten (wenn nicht gar alle) dieser Systeme – welche zu den hellsten Galaxien im jungen Universum gehören – Kollisionen und Verschmelzungen von gasreichen Galaxien ähnlicher Masse sind.

Dann wenden wir uns zwei nahen prototypischen verschmelzenden Galaxienpaaren

zu; NGC 6240 und Arp 220. Aufgrund ihrer relativen Nähe (96 bzw. 77 Mpc) bieten sie eine seltene Möglichkeit, momentan verschmelzende Galaxien im Detail zu studieren. Hierzu werten wir mit Hilfe adaptiver Optik gewonnene nahinfrarote Integralfeldspektroskopie- und Bilddaten und Millimeterwellenlängen-Interferometrie-Daten der Zentralregionen dieser Systeme aus. Mit Hilfe von archivierten *HST*-Daten zeigen wir, dass die Auswirkungen von Extinktion auf optische und nahinfrarote Daten dieser gasreichen major mergers am besten durch das empirische Gesetz von Calzetti et al. (2000) korrigiert werden.

Im Fall von NGC 6240 (Kapitel 4) konzentrieren wir uns hauptsächlich auf die stellaren Bewegungen und die verschiedenen Sternentstehungsgenerationen, die Kollisionsgeometrie und -phase, und der Ursprung und die Natur der Nuklei. Wir diskutieren Eingrenzungen der möglichen Kollisionsgeometrien und -phasen, und nutzen diese, um unsere Beobachtungen bezugnehmend auf typische Sternentstehungsentwicklungen in major mergers zu interpretieren. Wir zeigen, dass weniger als ein Drittel von NGC 6240's außerordentlicher Luminosität von der durch die Kollision hervorgerufenen Sternentstehung herrührt. Weiterhin berechnen wir die Masse der beiden Nuklei mithilfe von Jeans-Modellen. Dies, und das Vorhandensein einer alten Sternenpopulation, zeigt, dass die Nuklei Überbleibsel der bulges der Kollisionspartner sind.

Arp 220 (Kapitel 5) ist im K-Band sehr stark durch Extinktion beeinflusst; wie wir zeigen können, sehen wir weniger als 10% des tatsächlich ausgesandten Lichts im Nahinfraroten. Junge (ca. 10 Myr alte) Sterne sind für $\sim 50\%$ der K-Band-Luminosität verantwortlich; die andere Hälfte kommt von einer alten ($\gtrsim 1$ Gyr) Sternengeneration, die damit höchstwahrscheinlich vor die Kollision datiert. Die Nuklei sind auch hier sehr wahrscheinlich Reste der bulges der verschmelzenden Galaxien. Im westlichen Nukleus liegt das kinematischen Zentrum der Sternbewegungen auf der Position einer möglichen Signatur einer Akkretionsscheibe eines superschweren schwarzen Loches. Im östlichen Nukleus, in welchem die K-Band-Indikatoren aufgrund der starken Extinktion ein weniger klares Bild abgeben, zeigen die (tieferreichenden) Millimeterwellenbeobachtungen, dass die CO(2-1)-Emission und -Kinematik am besten durch zwei kompakte Quellen, welche um den Ursprung der Emission von heißem Staub kreisen, modelliert werden kann – ähnlich dem westlichen Nukleus.

Zusammenfassend haben wir eine Reihe von wichtigen Ergebnissen erzielt, welche unser Verständnis der Mechanismen und der Bedeutung von major mergers verbessert und erweitert haben; insbesondere ihre Rolle als Auslöser der höchsten Galaxienluminositäten im hochrotverschobenen Universum, und im Bezug auf die Sternentstehungsgeschichte, das Luminositäts- und Massebudget von fortgeschrittenen Verschmelzungen von gasreichen Galaxien ähnlicher Masse im lokalen Universum.

Abstract

One of the fundamental questions astrophysicists attempt to answer is how galaxies evolve over time. A key process in this context is the gravitational attraction and eventual merging of two near-equal mass galaxies, a so-called major merger. Profoundly transformative events, major mergers substantially affect virtually all properties of a galaxy on a timescale of several hundred million years. Mergers between two gas-rich disk galaxies in particular are believed to be responsible for triggering galaxy-wide starbursts, quasar activity, and the creation of elliptical galaxies. However, we still lack a good understanding both of the details of the merger process, and the role of major mergers at high redshifts, when the universe was roughly half its current age.

The aim of this thesis is to address these shortcomings. To this end, we utilise adaptive optics assisted near-infrared imaging and integral field spectroscopy data and millimetre interferometry data of two nearby prototypical major mergers and of a population of submillimetre-bright high-redshift galaxies.

We first give an overview of the field (Chapter 1) and techniques used (Chapter 2). In Chapter 3 we then investigate the mechanisms that lead to the exceptional luminosities of a class of high redshift galaxies known as 'Submillimetre-luminous Galaxies' (SMGs hereafter). Subarcsecond interferometric CO line emission data of 12 SMGs (for four of which we present new data) are employed to show that morphologically and kinematically, at least eight of them show strong indications of being mergers. For those systems consisting of two spatially separated galaxies, we find that the mass ratios of the merger partners are 1:3 or closer to unity, i.e. that these systems are major mergers. We then discuss the extent, to which local $L_{IR} \geq 10^{12} L_{\odot}$- and high-redshift $S_{850\mu m}$-selected major mergers sample the same merger stages, and compare their respective ratios of binary to coalesced systems. From this we infer that most, if not all, of those SMGs in our sample which morphologically and kinematically could be either isolated disk galaxies or late-stage, coalesced major mergers, must indeed be major mergers. We also compare our dynamical and gas mass measurements of our SMG sample to the stellar masses derived by other authors, lending strong support to the lower end of the range of published values. This in turn supports cosmological models in which SMGs arise through major mergers. We can thus convincingly show that most, if not all, of these systems – representing the brightest galaxies in the early universe – are mergers between near-equal mass, gas rich galaxies.

We then turn to two nearby prototypical merging galaxies; NGC 6240 and Arp 220. Due to their proximity (96 and 77 Mpc, respectively), they afford a rare opportunity to study on-going mergers in detail. To this end, we utilise adaptive optics assisted near-infrared integral field spectroscopic and interferometric millimetre CO line data of their central regions. From archival *HST* data, we show that the Calzetti et al. (2000) reddening law is the appropriate formalism to use when correcting for the

effects of extinction in these gas-rich major mergers.

For NGC 6240 (Chapter 4), we concentrate primarily on the stellar kinematics and stellar populations, the merger stage and geometry, and the nature and origin of the nuclei. We discuss constraints on the merger phase and geometry, and use these to interpret the observables in light of typical merger star formation histories. We are able to show that less than a third of NGC 6240's prodigious luminosity is due to the merger-induced starburst. We furthermore derive the mass of the two nuclei via Jeans modelling, which, in combination with the presence of a prominent old stellar population, indicate that the nuclei are remnants of the progenitor galaxies' bulges.

Arp 220 (Chapter 5) we find to be severely affected by extinction in the K-band. We are able to quantify that we are only seeing less than 10% of the emitted stellar light. A young starburst contributes at least $\sim 50\%$ of the K-band luminosity, with the remainder most likely due to a population $\gtrsim 1\,\mathrm{Gyr}$ old. The nuclei are most likely the remainders of the progenitor's bulges – in the western nucleus, the kinematic centre of the stellar kinematics is coincident with the hot dust emission posited to be the signature of an accreting central black hole, and in the eastern nucleus, which in the K-band tracers displays a less clear-cut picture due to strong extinction, we find mm-wavelength CO(2-1) emission to be best fitted by two compact, unresolved sources rotating around localised hot dust emission, akin to the western nucleus.

We thus have obtained several key results, which significantly advance our understanding of the mechanisms and importance of major mergers; in particular their role as triggers of the highest galactic luminosities in the high-redshift universe, and the star formation history, mass and luminosity budget of advanced, pre-coalescence present-day major mergers.

Publications

Chapters 3, 4 and 5 are all almost exact reproductions of papers submitted to or to be submitted to refereed journals:

- Engel H., Davies R. I., Genzel R., Tacconi L. J., Hicks E. K. S., Sturm E., Naab T., Johansson P. H., Karl S. J., Max C. E., Medling A., van der Werf P. P., 2010, A&A, in press

- Engel H., Tacconi L. J., Davies R. I., Neri R., Smail I., Chapman S. C., Genzel R., Cox P., Greve T. R., Ivison R. J., Blain A., Bertoldi F., Omont A., 2010, ApJ, in press

- Engel H., Davies R. I., Genzel R., Tacconi L. J., 2010, ApJ, to be submitted

In addition, the following publications partially resulted from work done by the author of this thesis:

- Medling A., Ammons M., Max C. E., Davies R., Engel H., 2009, AAS, 213, 437.01

- Davies R. I., Maciejewski W., Hicks E. K. S., Tacconi L. J., Genzel R., Engel H., 2009, ApJ, 702, 114

- Friedrich S., Davies R. I., Hicks E. K. S., Engel H., Müller Sánchez F., Genzel R., Tacconi L. J., 2010, A&A, in press

- Davies R. I., Engel H., Hicks E. K. S., Förster-Schreiber N., Genzel R., Tacconi L. J., Eisenhauer F., Rabien S., 2010, contribution to "Adaptive Optics Systems II", SPIE 7736-51

- Davies R. I., Hicks E. K. S., Schartmann M., Genzel R., Tacconi L. J., Engel H., Burkert A., Krause M., Sternberg A., Müller Sánchez F., Maciejewski W., 2010, Co-Evolution of Central Black Holes and Galaxies, Proceedings of the International Astronomical Union, IAU Symposium, Volume 267, p. 283-289

- Medling A., Ammons S. M., Max C. E., Davies R. I., Engel H., Canalizo G., 2010, ApJ, to be submitted

Contents

List of Tables

List of Figures

Chapter 1

Introduction

1.1 Setting the Scene

In the past decades, a coherent cosmological picture has emerged, which successfully explains an impressive range of observations, from the cosmic microwave background (Spergel et al. 2003, 2007; Dunkley et al. 2009), baryon acoustic oscillation imprints in the large scale structure (Eisenstein et al. 2005; Percival et al. 2007), the magnitude-redshift relation of type Ia supernovae (Riess et al. 1998, 2004, 2007; Perlmutter et al. 1999) to the mass function, baryon fraction, and evolution in number density of galaxy clusters (White et al. 1993; Bahcall et al. 2003; Bahcall & Bode 2003; Gladders et al. 2007; Vikhlinin et al. 2009). In this flat Λ cold dark matter (Blumenthal et al. 1984; Komatsu et al. 2009) concordance cosmology, the mass in the universe consists of 4.4% baryons, 21.4% non-baryonic dark matter, and 74.2% dark energy in the form of an Einsteinian 'cosmological constant' (Einstein 1917), or something with similar effect (Frieman et al. 2008 and references therein).

The behaviour of the still elusive dark matter particles, which interact only gravitationally, is well understood and thus dark matter structure formation can be modelled in numerical simulations (e.g. Davis et al. 1985; Springel et al. 2005b). Dark matter forms a so-called 'cosmic web' of massive haloes connected by filaments, which grew out of quantum fluctuations in the energy density of the rapidly expanding early universe that were amplified by gravity. Under the hierarchical clustering paradigm (White & Rees 1978; Mo & White 1996), merging of small building blocks leads to the formation of progressively larger dark matter structures. It is on this scaffolding that baryonic structure formation takes place. Baryons accrete into dark matter potential wells, where they condense, cool, and collapse to form stars and galaxies (Rees & Ostriker 1977; Silk 1977; White & Rees 1978; Fall & Efstathiou 1980). When two dark matter haloes merge, the baryonic condensations at their centres experience dynamical friction and sink to the centre of the potential well. It is thus expected that, especially at higher redshifts, mergers between galaxies are a frequent occurrence (e.g. Fakhouri & Ma 2008; Stewart et al. 2008).

However, the baryonic processes, which ultimately lead to the rich panoply of phenomena observable in our universe across the electromagnetic spectrum, are complex and in large parts still not well understood. Through which processes did the galaxies that we observe today form and evolve? Which mechanisms were driving stellar mass assembly and luminosity density at different cosmic epochs? Significant progress towards answering these questions has been made possible by the advancements in instrumentation and detector technology, which are allowing us to probe ever deeper into the universe and let us observe galaxies at different cosmic epochs. Moreover, observations at infrared and sub-millimetre wavelengths now allow the observation of dust-obscured galaxies, which escape detection in the optical and ultraviolet regimes that have long dominated traditional astronomy.

1.2   Ultraluminous Infrared Galaxies and Submillimetre Galaxies

The first far-infrared all-sky survey, carried out by the *Infrared Astronomical Satellite (IRAS)* (Neugebauer et al. 1984a), resulted in the detection of vast numbers of nearby objects previously undetected at optical wavelengths (Neugebauer et al. 1984b; Soifer et al. 1987). Subsequent investigation of the most infrared-luminous sources via optical and near-infrared imaging revealed that the fraction of strongly interacting/merger systems increases with increasing infrared luminosity; ranging from $\sim 10\%$ at $L_{IR} = 10^{10.5-11} L_\odot$ to nearly 100% at $L_{IR} \geq 10^{12} L_\odot$ (Sanders et al. 1988b; Melnick & Mirabel 1990; Sanders & Mirabel 1996; Murphy et al. 1996; Clements et al. 1996; Veilleux et al. 2002). The prodigious luminosities of these so-called UltraLuminous Infrared Galaxies and Luminous Infrared Galaxies (ULIRGs, $L_{IR} \geq 10^{12} L_\odot$, and LIRGs, $L_{IR} = 10^{11-11.9} L_\odot$, Sanders & Mirabel 1996) are due predominantly to the dust-reprocessed emission of obscured star formation activity (Sanders & Mirabel 1996; Genzel et al. 1998b). Detailed studies of prototypical (U)LIRGs can be found in Chapters 4 & 5. However, despite these superlative luminosities, LIRGs and ULIRGs only contribute a negligible fraction to the overall present day galactic energy budget (Magnelli et al. 2009 & Fig. 1.1). The reason for this is that the major mergers giving rise to this phenomenon are relatively rare events today, with the majority of galaxies evolving secularly (e.g. Maller et al. 2006; Bell et al. 2006). However, due to their proximity they are key to further our understanding of the merger process, providing us with exquisite observational data of on-going mergers.

The *Cosmic Background Explorer* satellite (*COBE*, Boggess et al. 1992) detected an extragalactic sub-millimetre background with an integrated intensity comparable to or larger than that of the integrated UV/optical light of galaxies (Puget et al. 1996; Dwek et al. 1998; Hauser et al. 1998; Lagache et al. 1999), indicating that a very significant fraction of high-redshift star formation is dust-obscured. This was confirmed by results from observations carried out with the *Spitzer Space Telescope*
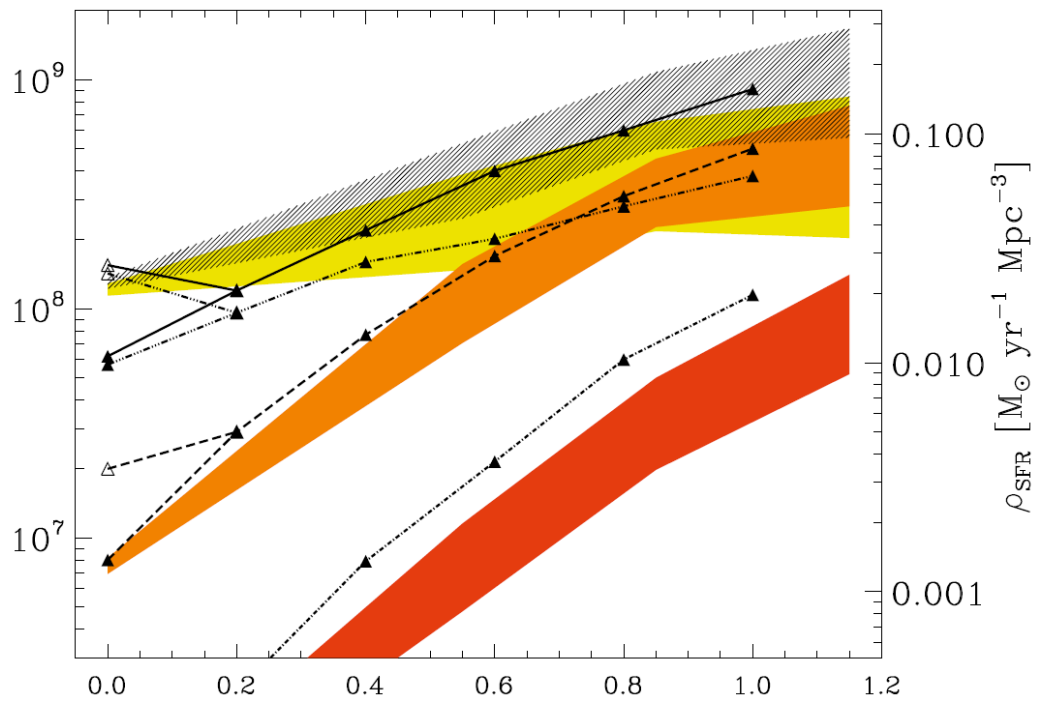
Figure 1.1: From Magnelli et al. (2009): Evolution of the total co-moving infrared energy density (grey), and the contributions from normal galaxies ($L_{IR} = 10^{7-10.99}$, yellow), LIRGs ($L_{IR} = 10^{11-11.99}$, orange), and ULIRGs ($L_{IR} = 10^{\geq 12}$, red).

(Werner et al. 2004), showing that at $z \sim 1$ the infrared luminosity density is five times higher than the UV luminosity density (Magnelli et al. 2009). And indeed, the *Infrared Space Observatory (ISO)* (Kessler et al. 1996) and the *Submillimetre Common User Bolometer Array (SCUBA)* (Holland et al. 1999) have uncovered significant populations of infrared-luminous galaxies at redshifts of $z < 1$ and $z \sim 1$-4, respectively (Genzel & Cesarsky 2000; Coppin et al. 2006). Studies with *ISO* and more recently *Spitzer* found that the relative and absolute contribution of LIRGs and ULIRGs to the star formation and luminosity density of galaxies increases dramatically with redshift; presently both classes combined account for only $\sim 2\%$ of the bolometric luminosity density compared to LIRGs contributing more than half and ULIRGs $\sim 10\%$ at $z \sim 1$ (Soifer & Neugebauer 1991; Kim & Sanders 1998; Xu 2000; Chary & Elbaz 2001; Lagache et al. 2003; Le Floc'h et al. 2005; Magnelli et al. 2009); the comoving number density of ULIRGs increases by two magnitudes in the same redshift interval (Chary & Elbaz 2001; Le Floc'h et al. 2005; Magnelli et al. 2009) and ULIRGs may dominate the cosmic star formation density at $z \sim 2$ (Caputi et al. 2007).

This trend towards a larger fraction of star formation being dust-obscured at high redshift is embedded in the redshift evolution of the overall cosmic star formation rate; results from different tracers are converging on a flat or gradually declining total star formation rate between $z \sim 3$ and $z \sim 1$, and a steeper decline between $z \sim 1$ and $z = 0$ (Chary & Elbaz 2001; Schiminovich et al. 2005; Hopkins & Beacom 2006; Magnelli et al. 2009 & Fig. 1.2).

It is thus clear that redshifts around $z \sim 2$ constitute a key epoch of cosmic stellar mass assembly, and that infrared-luminous and -ultraluminous galaxies play an important role.

It is for these reasons that the population of so-called sub-millimetre galaxies (SMGs, see Blain et al. 2002 for a review) detected by *SCUBA* has been the subject of intense study in recent years. Detection via their sub-millimetre emission ($S_{850\mu m} > 5\,\mathrm{mJy}$ is the canonical criterium) was followed up by precise localisation via radio interferometry (Ivison et al. 2002; Chapman et al. 2003) and redshift determination in the optical/UV (Chapman et al. 2003, 2005; Swinbank et al. 2004), allowing subsequent observations in a broad range of wavelength regimes. This class of galaxies is characterised by prodigious star formation rates ($\sim 1000\,M_\odot\,yr^{-1}$) and enormous bolometric luminosities, the majority of which is emitted as dust-reprocessed radiation in the far-IR ($L_{IR} \gtrsim 5 \times 10^{12} L_\odot$) (Blain et al. 2002; Smail et al. 2002; Chapman et al. 2005). Since the sub-millimetre band samples a part of the spectral energy distribution (SED) that falls with wavelength, the apparent brightness of SMGs is largely invariant over a large redshift range, enabling observations sampling a large epoch; the majority of detected SMGs lie in the redshift range $z \sim 1.5$-3 (Aretxaga et al. 2007). Several authors have investigated the power source of these exceedingly luminous galaxies, using spectroscopy in the near-IR (Swinbank et al. 2004), optical and X-ray (Alexander et al. 2005), and mid-IR (Lutz et al. 2005; Valiante et al. 2007; Pope et al. 2008a; Menéndez-Delmestre et al. 2009) to differentiate between starburst
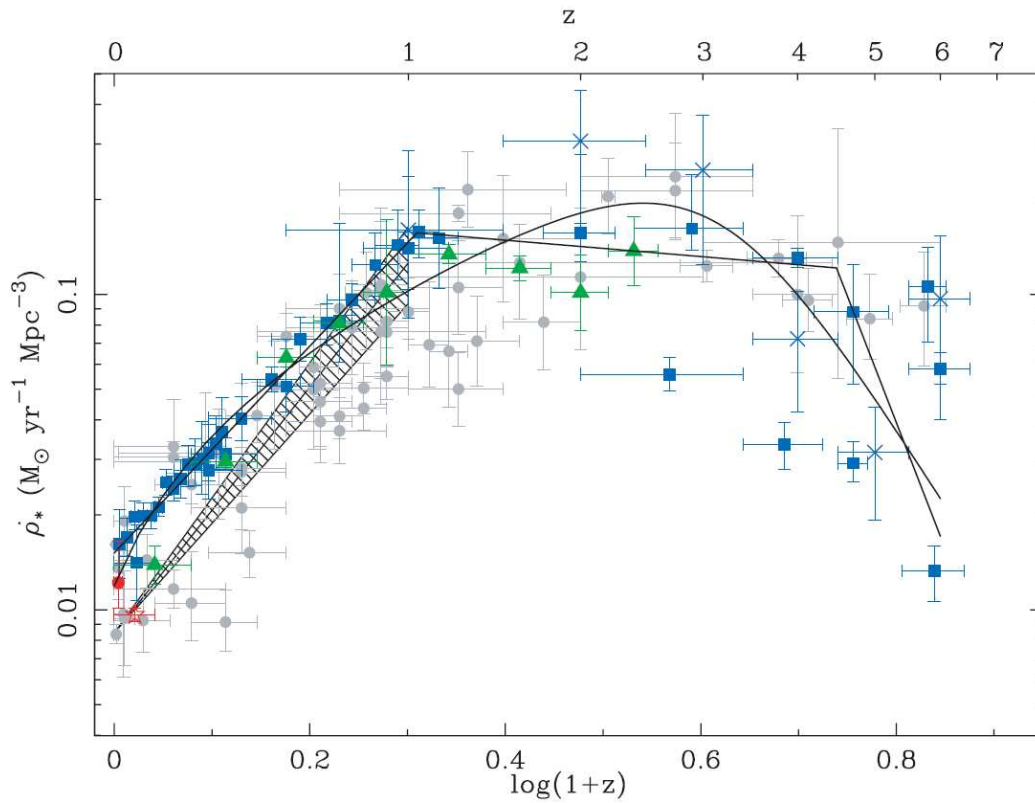
Figure 1.2: From Hopkins & Beacom (2006): Evolution of the star formation rate density with redshift, bringing together results from $24\,\mu m$ (green triangles), $1.4\,\mathrm{GHz}$ (open red star, Hα (red circle), UV (blue squares), Hubble Ultra-Deep Field estimates (blue crosses), and the compilation of Hopkins (2004).

and AGN contributions; the emerging consensus is that, analogous to local ULIRGs, starbursts are the primary power source of SMGs, with AGN being present in a large fraction but not making a significant energetic contribution.

Besides their energy source, another key question is what triggers the extraordinary luminosities of these objects. A number of authors have suggested that at least some SMGs may be interacting or merging systems. However, these conclusions are based primarily on irregular or complex morphologies seen in rest-frame UV *HST* images (Chapman et al. 2003, 2004; Smail et al. 2004; Swinbank et al. 2006). Two *caveats* need to be borne in mind regarding these results; UV emission is strongly affected by extinction, and hence UV images may not reliably track the underlying galaxy. Furthermore, morphological studies alone may be misleading – high-redshift galaxies are clumpy and irregular, which may either be the result of on-going mergers (Lotz et al. 2006; Conselice et al. 2008) or the consequence of clumpy star formation in a kinematically more coherent structure such as an underlying rotating disk (Förster-Schreiber et al. 2006, 2009; Genzel et al. 2006; Elmegreen et al. 2007). Hence one needs spatially resolved maps and kinematics of a tracer that is not affected by dust extinction to properly assess morphologies and kinematics. Interferometric CO line observations are well-suited for this objective; employing these Tacconi et al. (2006, 2008) find SMGs to display either double/multiple morphologies with complex, disturbed gas motions indicative of on-going mergers, or to be extremely dense, compact, rotating disks. The high gas densities of the latter argue for them to be end-stage major mergers, however the spatial resolution is insufficient to definitively distinguish between coalesced major mergers and quiescent disk galaxies. At present it is thus still unclear whether SMGs form a homogeneous class of objects, or whether their high luminosities can be achieved through a variety of pathways. This question is the topic of Chapter 3.

1.3 Major Mergers; their role in stellar mass assembly...

The question of the nature of SMGs in particular coincides with a renewed debate about the role of major mergers in galaxy formation and evolution in general. The conventional picture of galaxy formation posits that gas falling into a dark matter halo will be shock-heated to approximately the halo virial temperature, then radiate away its thermal energy and eventually settle into a centrifugally supported disk and form stars (White & Rees 1978; Fall 1979; Blumenthal et al. 1984; White & Frenk 1991; Kauffmann et al. 1993; Mo et al. 1998). Mergers of approximately equal-mass disks result in the formation of a spheroidal system (Toomre & Toomre 1972; Barnes & Hernquist 1992), which may re-acquire a disk through subsequent gas accretion. In this picture, galaxies are thus expected to grow through recursive mergers, which are the primary driver of star formation and the forming of a bulge. However, recent

observational results and theoretical developments seem to require a revision of this cosmological framework. If galaxies assembled hierarchically in a bottom-up fashion, one would expect the largest galaxies to have formed last, and thus be evolutionary younger than their smaller brethren. However, this expectation is not borne out by observations of the local universe: the most massive ($M_\star > 10^{11} M_\odot$) galaxies by and large are all early type (Brinchmann & Ellis 2000; Bundy et al. 2005) and have stopped forming stars long ago (Kauffmann et al. 2003; Trager et al. 2000). At higher red-shifts ($z \sim 1.5\text{-}3.5$), observations of rest-frame UV/optical magnitude-selected galaxies (termed 'BX/BM' Adelberger et al. 2004; Steidel et al. 2004 and 'sBzK' galaxies Daddi et al. 2004a,b, respectively) have shown these luminous ($10^{11-12.5} L_\odot$), star-forming ($10\text{-}300\ M_\odot\,\mathrm{yr}^{-1}$) galaxies to contribute significantly to the cosmic star formation activity and stellar mass density at these redshifts (Reddy et al. 2005; Rudnick et al. 2006; Grazian et al. 2007). Their observed correlation between stellar mass and star formation rate points towards sustained, steady star formation rather than short bursts being the dominant growth mode of these galaxies (Noeske et al. 2007; Elbaz et al. 2007; Daddi et al. 2007). Recent advances in instrumentation and detector technology have made possible spatially resolved spectroscopic observations of the ionised gas distribution and kinematics of the brighter and more massive of these galaxies, showing that only about a third of them show signs of recent or on-going merging activity, another third are compact, dispersion-dominated objects and the remainder are large rotating disk galaxies (Förster-Schreiber et al. 2006, 2009; Genzel et al. 2006, 2009; Shapiro et al. 2008). Numerical simulations (Semelin & Combes 2002; Birnboim & Dekel 2003; Kereš et al. 2005; Dekel et al. 2009) indicate that lower-mass galaxies ($M_{gal} \lesssim 10^{10} M_\odot$) may in fact acquire the majority of their gas not through slow condensation of shock-heated gas but through 'cold mode' accretion, in which the infalling gas efficiently radiates away its gravitational energy. Since this accretion mode requires a comparatively low-mass dark matter halo, it is expected to be important in particular at high redshifts and in present-day low density environments. These cold accretion flows are conjectured to consist of both smooth and clumpy gas flows, the former building up a disk and the latter leading to the formation of a spheroidal component (Dekel et al. 2009); aforementioned observations constitute key evidence in support of this cosmological model (Genzel et al. 2009).

However, even though their long-conjectured role as the dominant driver of cosmological baryonic mass assembly and star formation is coming under scrutiny, major mergers between galaxies are undoubtedly giving rise to the most rapidly star-forming galaxies observed in the local universe (ULIRGs; e.g. Sanders & Mirabel 1996), and possibly also at $z \sim 2$ (SMGs; Chapman et al. 2003, 2004; Smail et al. 2004; Swinbank et al. 2006; Tacconi et al. 2006, 2008).
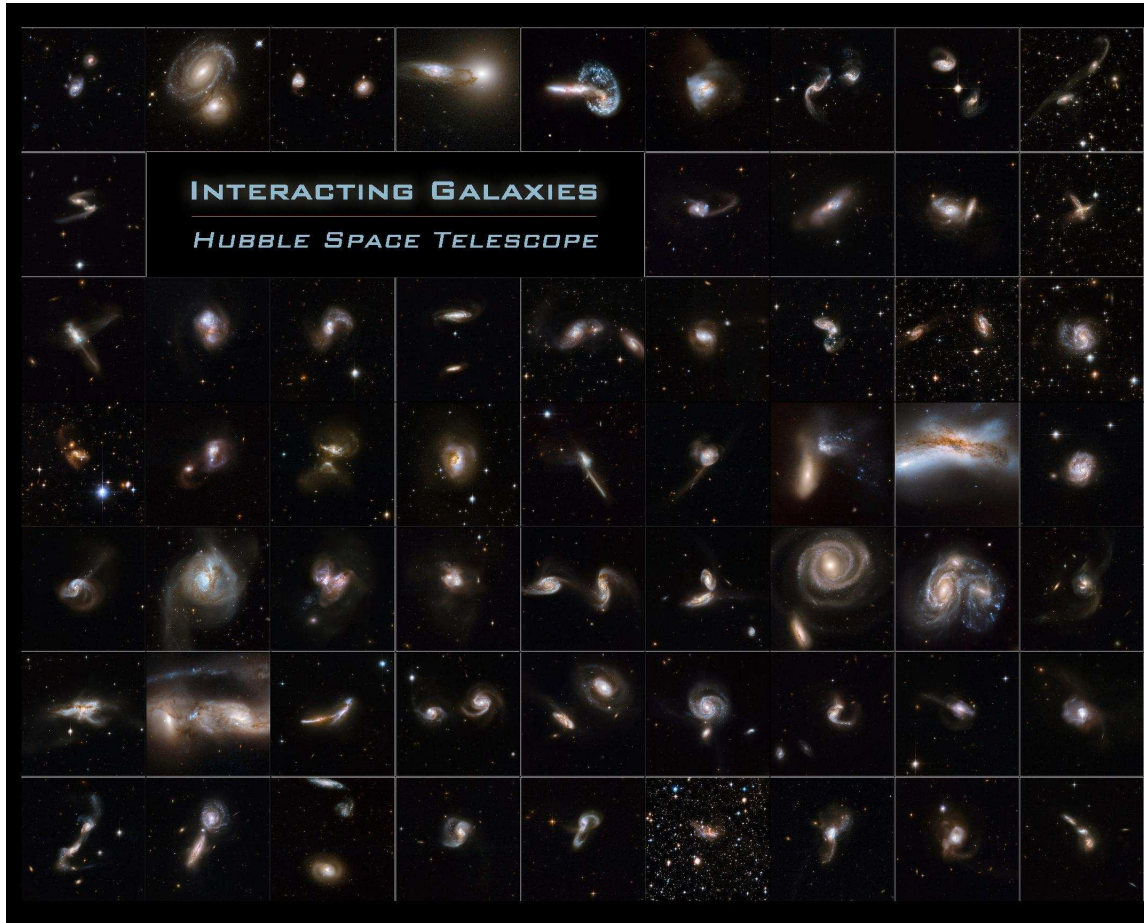
Figure 1.3: *Hubble Space Telescope* images of interacting galaxies. Image Credits: NASA, ESA, & Hubble Heritage (STScI/AURA)-ESA/Hubble Collaboration; acknowledgements: A. Evans (University of Virginia, Charlottesville/NRAO/Stony Brook University), W. Keel (University of Alabama, Tuscaloosa), K. Noll, B. Whitmore and M. Stiavelli (STScI), G. Ostlin (Stockholm University), and J. Westphal (Caltech).

1.4   ...and galaxy evolution

Despite the realisation that cold accretion is important, major mergers remain a key mechanism in galaxy evolution and transformation. As already mentioned earlier, Toomre & Toomre (1972) in a seminal paper suggested that mergers of near-equal mass spiral galaxies produce a spheroidal merger remnant; an elliptical galaxy. This has since been confirmed and refined by studies of the kinematic, structural, and photometric properties of advanced mergers currently in the ULIRG phase (Kim et al. 2002; Veilleux et al. 2002; Genzel et al. 2001; Tacconi et al. 2002; Dasyra et al. 2006b), showing that they resemble intermediate-mass ellipticals in terms of their light profiles, velocity dispersions, v_{rot}/σ, and location on the fundamental plane (FP, Djorgovski & Davis 1987), and the presence of structures in ellipticals (e.g. shells, nuclear light excesses, kinematic subsystems) indicative of recent mergers (Quinn 1984; Hernquist & Barnes 1991; Schweizer & Seitzer 1992; Mihos & Hernquist 1994; Kormendy et al. 2009), as well as by numerical simulations (Barnes 1988, 1992; Hernquist & Spergel 1992; Barnes & Hernquist 1996; Naab et al. 1999; Springel et al. 2005a; Naab & Burkert 2003; Jesseit et al. 2007). In recent years, this picture has been expanded to a merger sequence (Sanders et al. 1988a,b; Hopkins et al. 2006, 2008a,b; Somerville et al. 2008 & Fig. 1.4), in which a merger between two gas-rich disk galaxies triggers an intense nuclear starburst ('ULIRG phase', see discussion above) and fuels rapid growth of the supermassive black holes in the galaxies' centres. Feedback from the starburst and the AGN blows out the gas (Di Matteo et al. 2005; Tremonti et al. 2007), thus quenching the star formation and leading to an optically luminous quasar, which will eventually fade and leave a red, passively evolving elliptical galaxy. Support for this posited causal connection between major mergers and quasar activity is lent by a number of observational results. Canalizo & Stockton (2001); Kauffmann et al. (2003b); Jahnke et al. (2004); Vanden Berk et al. (2006) find young stellar populations and postmerger imprints in quasar hosts. Almost all red-and-dead galaxies contain a bulge component and thus a large supermassive black hole (Bell 2008). The Soltan (1982) argument (showing that nearly all the mass in supermassive black holes must have been accumulated during a period of quasar activity) in conjunction with the observed close correlation between the supermassive black hole mass and its host's bulge mass (Magorrian et al. 1998; McLure & Dunlop 2002; Marconi & Hunt 2003), and the fact that numerical simulations indicate that mergers produce 'classical' bulges (e.g. Barnes & Hernquist 1992; Springel et al. 2005a; Naab & Burkert 2003; Jesseit et al. 2007), taken together imply that the process responsible for forming spheroids simultaneously also triggers quasar activity. In this framework, galaxy mergers give rise to a number of observed galaxy properties, such as the bimodal distribution of galaxies in a colour-magnitude diagram (Strateva et al. 2001; Bell 2008) and the aforementioned correlation between the mass of the supermassive black hole appearing to reside at the center of most galaxies (Kormendy & Richstone 1995; Richstone et al. 1998; Ho 2008) and the host galaxy's bulge mass (Magorrian

et al. 1998; McLure & Dunlop 2002; Marconi & Hunt 2003) or velocity dispersion (Ferrarese & Merritt 2000; Gebhardt et al. 2000; Tremaine et al. 2002).
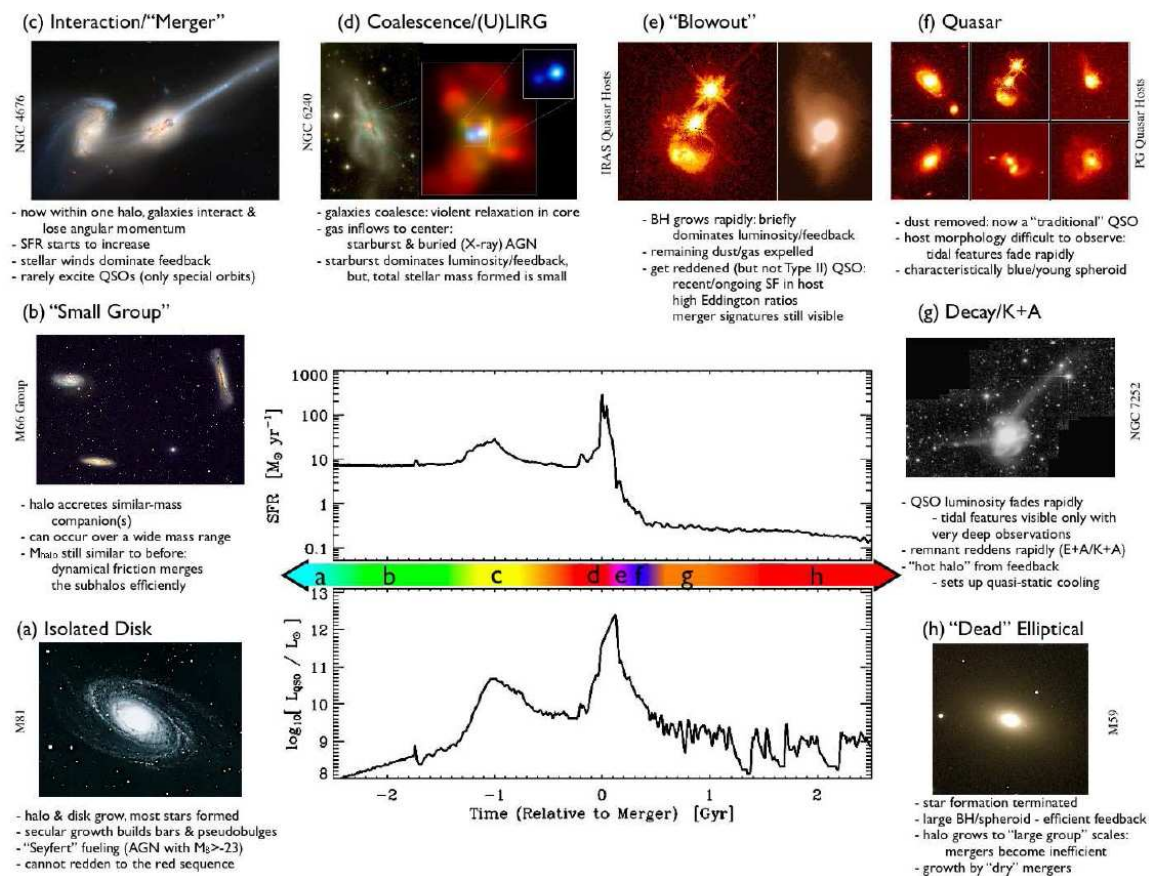
Figure 1.4: Schematic outline of a major merger sequence, from Hopkins et al. (2008a).

However, despite their recognised importance we still lack a good understanding of merger processes; due both to the complexity and the shortlived nature of these events. What is the dominant feedback process responsible for expelling the gas and quenching star formation; the accreting black hole, star formation, or a (sequential?) combination of both? Do bulges and black holes grow in parallel, or off-set? There is much still to be learnt about these galactic encounters that give rise to some of the most complex and visually compelling structures observable in our universe.

The broad theme of this thesis are major mergers. In the first part, we identify major mergers as the mechanism leading to the extreme luminosities of the most rapidly star-forming high-redshift galaxies. In the second part, we endeavour to improve our understanding of merger processes in general by investigating two prototypical examples.

Chapter 2

Background – Observational Techniques, Extinction, and Jeans Modelling

In this Chapter, we describe the observational (adaptive optics, integral field spectroscopy, interferometry) and theoretical (Jeans modelling) techniques used in the analyses. In addition, we outline some aspects related to extinction.

2.1 Adaptive Optics Assisted Near-Infrared Integral Field Spectroscopy

A major development in astronomical instrumentation has been the advent of integral field spectrographs. Combining the two previously separately used techniques of imaging (using filters covering a range of wavelengths to obtain a spectrally integrated two-dimensional image), and two-dimensional slit spectroscopy (providing spectroscopic information along the slit axis), integral field spectrographs produce three-dimensional datacubes by extracting a full spectrum for each spatial pixel of the field of view (FoV). Integral field spectrographs use pre-optics to relay the FoV from the focus of the telescope onto an integral field unit. The integral field unit samples or slices the FoV, and feeds the slices into a spectrograph, which produces the individual spectra that are then recombined into the full 3D data cube. This technique enables a much more time-efficient extraction of scientific data, which previously could only be done by, in most cases prohibitively time-consuming, repeat single slit spectroscopy observations or repeat settings for imaging with a tunable narrow band filter such as a Fabry-Pérot etalon.

An equally important advancement in recent years was the successful construction of adaptive optics modules, and laser guide star facilities. Ground-based observatories' resolution was long limited by the blurring effects of the atmosphere, caused by
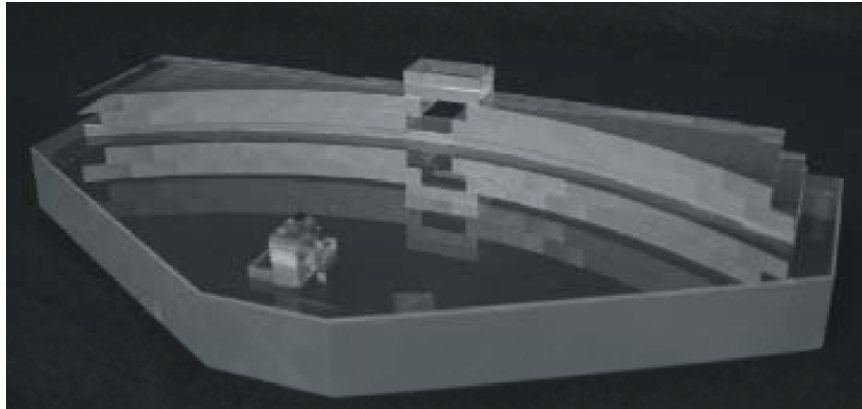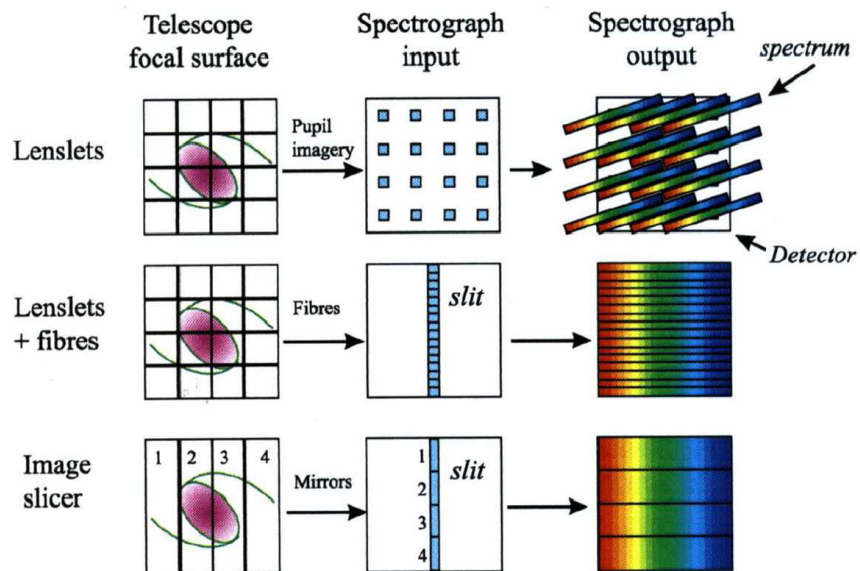
Figure 2.1: Top: Different types of integral field units. Bottom: *SPIFFI* image slicer; the light, entering through the central hole in the arc, is divided into 32 slices by a small stack of mirrors, and directed toward the 32 mirrors composing the arc, which rearranges the slitlets to a 31 cm pseudo-slit.

local variations in the air's temperature and density and thus its refractive index n. These lead to temporally varying deformations in the wavefront, and hence a blurred image. Kolmogorov (1941) described the statistical structure function for changes in the atmosphere's refractive index: $D_n(r) = C_n^2 r^{2/3}$; with r the distance between two points, and C_n^2 the local scale of the change in n – usually a function of height above ground, since the atmosphere is stratified into a series of horizontal layers. The statistical effect of these variations in n on a propagating wavefront is usually quantified via the coherence length r_0, the diameter of a circle within which the distortion is smaller than 1 radian^2 (i.e., the wavefront remains effectively flat). It is given by $r_0 = \left(16.7\lambda^{-2}\left(\cos\gamma\right)^{-1}\int_0^\infty dh C_n^2\left(h\right)\right)^{-3/5}$, with h the height of the disturbing atmospheric layer above the telescope, and γ the angular distance of the observed object from zenith. At good observation sites, r_0 is typically in the range 10-20 cm at optical, and 60-120 cm at near-infrared wavelengths, and therefore the resolution limit of the telescope due to these atmospheric effects ('seeing', given by λ/r_0 rather than λ/D) is $\sim$0.5-1$''$.

Adaptive optics (AO) corrects the wavefront deformations by applying the opposite deformation to a mirror, so that the reflected wavefront is flat again. The basic components of an AO system are a wavefront sensor, determining the shape of the wavefront using a guide star, a real-time computer calculating the corrections to be applied to the wavefront, and a deformable mirror. In order to reach a resolution approaching the diffraction limit of the telescope, a spatial sampling of the wavefront of order r_0 or smaller is required. Since the mirror deformations can only be applied after the measurement, an important parameter is the coherence timescale τ_0, which describes how quickly the wavefront of the incoming light is changing, and therefore determines the required frame rate (typically ten or more per τ_0). The coherence timescale is determined by the time taken by the wind to blow across r_0, and is typically a few milliseconds in the visible, and $\sim$ 20 ms at infrared wavelengths. Another key parameter is the isoplanatic angle θ_0, a measure of the angular distance at which the atmospheric perturbations to light from two different objects become uncorrelated (a function of the vertical extent of the turbulent layers) – this is important, since the guide star used to sample the perturbations must have an angular distance to the science target of θ_0 or smaller, so that the turbulences measured from the guide star are the same as those afflicting the science target. The isoplanatic angle is typically a few arcseconds in the optical, and 20-40$''$ in the near-infrared. This, together with the requirement that the guide star must be relatively bright ($V \sim 14$-15 mag; fainter stars do not provide enough photons to measure the wavefront properly), severely limits the applicability of AO systems, since the probability of finding a suitably bright guide star close enough to the science target is generally quite low. Therefore ways to produce artificial guide stars were investigated, leading to the development of laser guide star facilities. A laser beam tuned to 589 nm produces a bright spot $\approx$ 90 km above ground by fluorescently exciting atomic sodium deposited in the mesosphere by meteorites. This spot then serves as a guide star for the AO system. However,

this is complicated by the fact that the laser light is perturbed twice; on the way up, and on the way down. This is resolved by measuring this 'tip-tilt' using an additional natural guide star ('tip-tilt star') and thus correct for it. Since the whole telescope aperture is used to measure the tip-tilt, the constraints on the brightness and angular distance of the tip-tilt star are much less severe than those on the guide star itself.

Our near-infrared data (Chapter 4 & 5) were obtained at the European Southern Observatory's Very Large Telescope (VLT) facility on Cerro Paranal, Chile, using SINFONI. SINFONI (Eisenhauer et al. 2003) is mounted on one of the VLT's four 8.2 m telescopes, and consists of an adaptive optics module (Bonnet et al. 2004)) and the near-infrared integral field spectrograph SPIFFI. In laser guide star mode, it is operated with PARSEC (Bonacini Calia et al. 2006; Rabien et al. 2004), the VLT laser guide star facility.

'Near-infrared' denotes radiation with wavelengths just longward of the visible spectrum. It is of particular interest to astronomers, since due to its longer wavelengths it is not scattered by interstellar dust like ultraviolet (UV) and visible light, enabling observers to study objects hidden by gas and dust in the UV/optical regimes. Furthermore, contrary to far-infrared radiation, near-infrared observations can be carried out from ground-based telescopes due to several atmospheric transmission windows in this regime. In comparison to UV and optical radiation, the near-infrared samples cooler (and thus older) stars in the local universe. At redshifts of $z \sim 2$, near-infrared emission corresponds to rest-frame UV/optical wavelengths and thus the same *caveats* apply as with UV/optical observations locally; namely that emission from dusty galaxies will be severely extinction-affected and thus may not reliably trace the underlying galaxy structure.

2.2   Millimetre-Wavelength Interferometry

Interferometry arrays achieve a resolution far beyond the diffraction limit of the individual telescopes it consists of. This is done by combining the signal received by pairs of telescopes and measuring the interference pattern, obtaining one Fourier component of the source per telescope pair, or baseline. A single interferometric measurement from a pair of telescopes thus provides one data point in the so-called *uv*-plane, the Fourier-transform plane of the angular source brightness distribution on the sky. The on-sky image can then be precisely reconstructed when the entire *uv*-plane has been sampled. However, this would require a prohibitively large number of telescope pairs, so that in practise one can only obtain an incomplete picture of the science target. In particular, the smallest and largest resolved angular scales are determined by the observing wavelength and the longest and shortest baselines, respectively. The necessarily incomplete sampling of the *uv*-plane between those two limits leads to further loss of information. In sampling the *uv*-plane, the Earth's rotation plays a crucial role, by rotating the baseline of each telescope pair relative to the source and thus dramatically increasing the *uv*-plane coverage with increasing observation time.
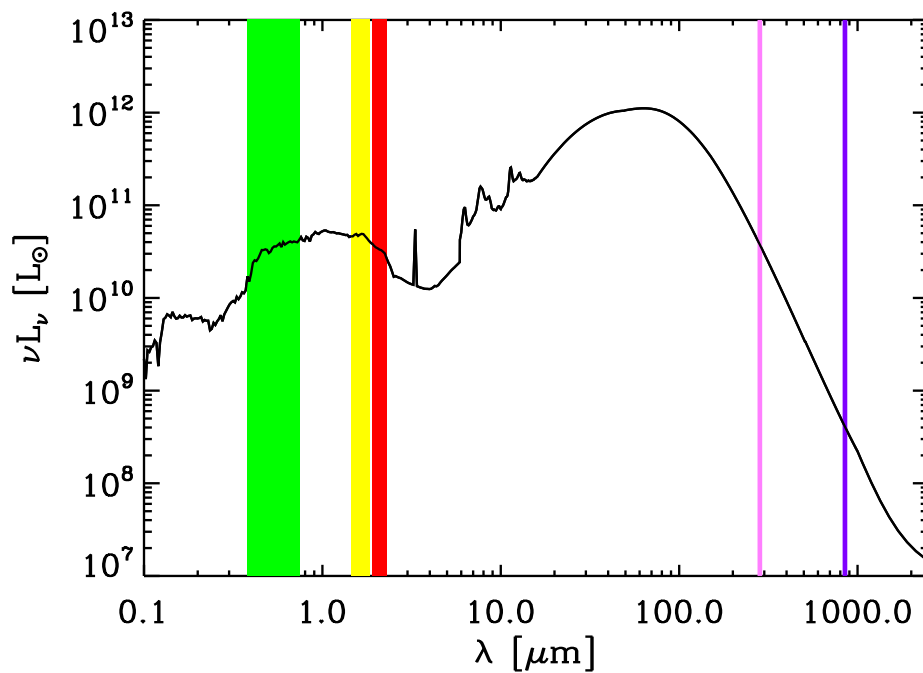
Figure 2.2: Typical spectrum of a $L_{IR} \sim 10^{12} L_\odot$ starburst galaxy. Green demarcates visible wavelengths, yellow the H-, and red the K-band. The purple line indicates $850 \, \mu m$, and the pink line the rest-frame wavelength of radiation from a $z = 2$ galaxy which, due to redshift, is observed at $850 \, \mu m$. This illustrates the so-called 'negative K-correction'; when observing objects at increasingly higher redshifts at a fixed wavelength of $850 \, \mu m$, the corresponding rest-frame wavelength is increasingly smaller and thus moves towards higher-energetic parts of the SED.

After the interferometry observations have been obtained, the original on-sky image is reconstructed from the interferometric data through deconvolution. The visibility $V_0(u,v)$ is the Fourier Transform of the on-sky brightness distribution of the science target, $V_0(u,v) = FT[I_0(x,y)]$; however due to our incomplete sampling of the uv-plane, we have only measured $V_{obs}(u,v) = S(u,v)V_0(u,v)$, with $S(u,v)$ the uv-plane sampling function of our observing run. The inverse Fourier Transform of $S(u,v)$ is called the dirty beam, $B_{dirty}(x,y) = FT^{-1}[S(u,v)]$; this is essentially the response of the interferometer setup to a point source. The first step in obtaining an image of the science target is to take the inverse Fourier Transform of $V_{obs}(u,v)$, resulting in the so-called dirty image: $I_{dirty}(x,y) = FT^{-1}[S(u,v)V_0(u,v)]$. Using the above and the convolution theorem, this can be rewritten as the convolution of the on-sky brightness distribution and the dirty beam: $I_{dirty}(x,y) = B_{dirty}(x,y) * I_0(x,y)$

In order to obtain a 'clean' image from I_{dirty}, it must be deconvolved. This is non-trivial, since due to the incomplete sampling, in theory an infinite number of brightness distributions are consistent with the data. Deconvolution is usually done using the CLEAN algorithm (Hogbom & Brouw 1974). This assumes that the sky brightness distribution can be decomposed into a finite number of point sources on an otherwise blank sky. The clean image is constructed by finding the peak in the dirty image, adding a corresponding point source to the clean image and subtracting an appropriately scaled dirty beam from the dirty image. This process is iterated, until the residuals in the dirty image approach the noise level. Finally, the clean image is smoothed with a Gaussian fit to the dirty beam ('clean beam'), and the residuals of the dirty image are added.

Our CO line emission data were obtained at the Plateau de Bure Interferometer located at an altitude of 2560 m near Grenoble in France. It consists of six 15 m-diameter telescopes, with baselines up to 760 m allowing spatial resolutions of up to 0.25″ at 1 mm in the longest-baseline configuration. Atmospheric transmission windows allow observations at wavelengths of ~ 0.8, 1, 2, and 3 mm. Similar to the near-infrared regime discussed above, millimetre-wavelength observations are unaffected by dust extinction and thus trace the underlying structure more reliably than rest-frame UV and optical data – particularly important e.g. when investigating the morphology of high-z galaxies, as we do in Chapter 3. Millimetre wavelength observations probe emission from cold gas and dust; it is at these wavelengths that the emission of a blackbody at ~ 3-70 K peaks.

Millimetre-wavelength continuum observations, sampling the Rayleigh-Jeans regime of the blackbody curve, are particularly well suited to detect objects over a long wavelength range, due to an effect known as 'negative K-correction'. Put simply, the effect of higher-redshift objects being increasingly dimmer is offset by the observed emission corresponding to increasingly shorter rest-frame wavelengths and thus more energetic emission (Fig. 2.2). As a result, galaxies between z$\sim$1-5 have near-equal $S_{850\mu m}$ emission and thus are equally likely to be detected by surveys at these wavelengths.

At redshifts z$\sim$1-3, several CO rotational transitions fall into the atmospheric

millimetre-wavelength transmission windows, allowing observations of their emission lines and thus of the morphology and kinematics of cold molecular gas. In Chapter 3 we utilise these to investigate the nature of high-redshift galaxies detected via their $S_{850\mu m}$ as outlined above.

2.3 Extinction

'Extinction' in an astronomical context refers to the absorption and scattering of light by matter located between an observed astronomical object and the observer. The interstellar medium consists to $\sim 70\%$ of neutral, ionised, and molecular hydrogen, with the majority of the remaining mass in helium, and metals such as carbon and silicon accounting for a few percent. Despite being near-negligible in the interstellar mass budget, dust is the dominant cause of extinction over the largest part of the spectrum. At visible to infrared wavelengths, the magnitude of scattering is directly proportional to the size of the scattering particles, and inversely proportional to the wavelength of the scattered light. At these wavelengths, the effect of dust extinction is therefore a reddening of the observed object. If λ is much greater than the dust grains, light passes through virtually unimpeded, and at significantly smaller wavelengths the extinction is independent of wavelength. Absorption features in the extinction vs. λ relation provide an indication of the composition of the dust: Graphite manifests itself in a distinctive bump at $2175\,\text{Å}$, absorption bands at $9.7\,\mu m$ and $18\,\mu m$ point towards the presence of silicate grains, and polycyclic aromatic hydrocarbons lead to emission bands between $3.3\,\mu m$ and $12\,\mu m$. Although its exact composition is still controversial and most likely also subject to spatial variations, interstellar dust appears to consist of graphite and silicate grains with sizes between $\sim 0.25\,\mu m$ and a few Angstroms. Attenuation is not the only effect of interstellar dust; the absorbed energy is re-emitted, mostly at mid-infared and longer wavelengths, this dust-reprocessed starlight dominates galaxies' SEDs at wavelengths larger than a few micron. Dust emission at $\lambda \lesssim 40\text{-}50\,\mu m$ is dominated by particles of size $\lesssim 100\,\text{Å}$ at temperatures of a few hundred Kelvin or larger. Emission longward of $\sim 80\,\mu m$ on the other hand is due to large dust grains ($\gtrsim 100\,\text{Å}$) in thermal equilibrium with their surroundings; their emission can therefore be modeled as the sum of multiple modified Planck functions.

When analysing astronomical data observed at near-infrared or shorter wavelengths, taking extinction and emission due to dust into account is important. In the near-infrared, there may be emission from very hot dust (such as found in the vicinity of an AGN), but the dominant effect that needs to be taken into account during analyses will be extinction. The two key factors determining the magnitude of scattering are the amount of dust present, and its spatial distribution with respect to the stars. The former is quantified via the optical depth τ, which is defined as the negative logarithm of the fraction of radiation not scattered or absorbed when passing through a partially transparent medium. As said above, the wavelength-dependence of the extinction depends on the nature and composition of the obscuring medium,

which in the case of interstellar dust is only approximately known. One has therefore to rely on empirical derivations, such as those of Landini et al. (1984), who find $\tau \propto \lambda^{-1.85\pm0.05}$ in the near-infrared. If the obscuring dust is located between the observed stars and the observer, the ratio of the observed to the emitted intensity is $I_{obs}/I_{em} = e^{-\tau}$; this assumption of the dust being spatially separated from the stars is commonly referred to as the 'screen' model. However, this simple model may be inadequate, more often than not the dust and stars are spatially coincident. The 'mixed' model emulates this, by assuming a uniform mix of stars and dust; in this case, $I_{obs}/I_{em} = (1 - e^{-\tau})/\tau$. Another way to relate intrinsic and observed emission are empirically derived reddening relations, e.g. those of Calzetti et al. (2000), based on nearby starburst galaxies. In Fig. 2.3, we compare I_{obs}/I_{em} as a function of wavelength and for a given τ, for the three examples above. As can be seen, unsurprisingly a given amount of dust obscures starlight more efficiently when placed in a screen in front of an observed galaxy instead of being spatially mixed with the stars. Furthermore, it is evident that the amount of light passing through decreases more sharply with decreasing wavelength in the 'screen' than in the 'mixed' case. At this level of extinction, the Calzetti et al. (2000) reddening law approximates to screen extinction at $\lambda \approx 1\,\mu m$, and to mixed extinction near $\lambda \approx 2.5\,\mu m$ – possibly reflecting the fact that both screen and mixed extinction occur in real galaxies, with screen extinction more dominant at lower wavelengths.

2.4   Jeans Modelling

Knowledge of spatially resolved kinematics of objects moving in a gravitational potential allows a derivation of this gravitational potential. Two main avenues can be taken: Schwarzschild orbit superposition and Jeans modelling. The former proceeds by reproducing the velocity and dispersion maps from a large suite of stellar orbits calculated for a given potential, which is varied until a match to the observations is achieved. The latter employs the Jeans equations, derived by taking moments of the collisionless Boltzmann equation. For all but the highest-quality data, Jeans modelling is better suited to recover the mass distribution, since the accuracy and resolution of the kinematic data is usually insufficient for Schwarzschild modelling. Here we give an introduction to this technique, as we employ it in Chapter 4.

2.4.1   Derivation of the Jeans equation

The distribution function f is defined such that $f(\mathbf{x}, \mathbf{v}, t)d^3\mathbf{x}d^3\mathbf{v}$ is the probability of a given star having phase-space coordinates in the range $d^3\mathbf{x}d^3\mathbf{v}$ at time t. If we are looking at a set of *identical* stars, this probability is the same for all stars. If there are no sources or sinks of stars (i.e. no stars are born or destroyed), we can apply the
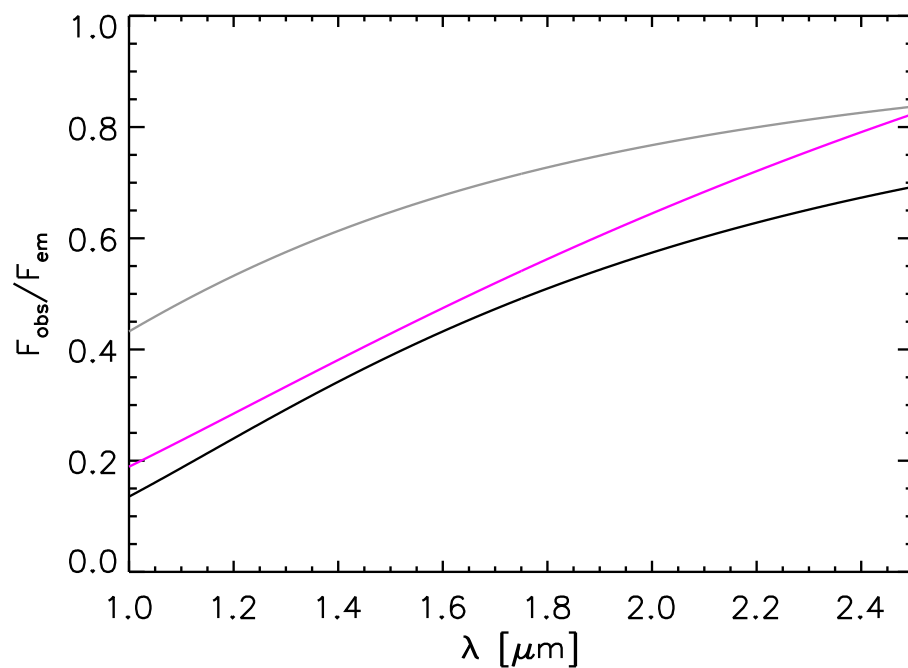
Figure 2.3: I_{obs}/I_{em} as a function of wavelength and for $\tau_K = 2$, for 'screen' (black) and 'mixed' (grey) extinction, and the Calzetti et al. (2000) reddening law (purple). As can be seen, a given amount of dust obscures starlight more efficiently when placed in a screen in front of an observed galaxy instead of being spatially mixed with the stars. Furthermore, it is evident that the amount of light passing through decreases more sharply with decreasing wavelength in the 'screen' than in the 'mixed' case.

continuity equation:

$$\frac{\partial f}{\partial t} + \frac{\partial}{\partial \mathbf{w}} (f \dot{\mathbf{w}}) = 0, \tag{2.1}$$

with $\mathbf{w} = (\mathbf{x}, \mathbf{v})$, analoguous to the continuity equation for fluid flow, with probability the quantity being conserved. Since $(\dot{\mathbf{x}}, \dot{\mathbf{v}}) = (\mathbf{v}, -\nabla\Phi)$, this simplifies to

$$\frac{\partial f}{\partial t} + \mathbf{v}\frac{\partial f}{\partial \mathbf{x}} - \frac{\partial \Phi}{\partial \mathbf{x}}\frac{\partial f}{\partial \mathbf{v}} = 0, \tag{2.2}$$

the *collisionless Boltzmann equation.* The Jeans equations are derived by taking moments of this. For example, expressing equation 2.2 in spherical coordinates,

$$0 = \frac{\partial f}{\partial t} + v_r\frac{\partial f}{\partial r} + \frac{v_\theta}{r}\frac{\partial f}{\partial \theta} + \frac{v_\phi}{r\sin\theta}\frac{\partial f}{\partial \phi}$$
$$+ \left(\frac{v_\theta^2 + v_\phi^2}{r} - \frac{\partial \Phi}{\partial r}\right)\frac{\partial f}{\partial v_r}$$
$$+ \frac{1}{r}\left(v_\phi^2\cot\theta - v_r v_\theta - \frac{\partial \Phi}{\partial \theta}\right)\frac{\partial f}{\partial v_\theta}$$
$$- \frac{1}{r}\left[v_\phi(v_r + v_\theta\cot\theta) + \frac{1}{\sin\theta}\frac{\partial \Phi}{\partial \phi}\right]\frac{\partial f}{\partial v_\phi}, \tag{2.3}$$

and assuming a steady-state system with $\overline{v}_r = \overline{v}_\theta = 0$, integrating v_r times equation 2.3 over all velocities yields the Jeans equation

$$\frac{d\left(\nu\overline{v_r^2}\right)}{dr} + \frac{\nu}{r}\left[2\overline{v_r^2} - \left(\overline{v_\theta^2} + \overline{v_\phi^2}\right)\right] = -\nu\frac{d\Phi}{dr}. \tag{2.4}$$

Here $\nu(\mathbf{x}) \equiv \int d^3\mathbf{v} f(\mathbf{x}, \mathbf{v})$ is the probability per unit volume of finding a particular star at position $\mathbf{x}$. This probability density can be related to the number density, luminosity density, or mass density by multiplication with the total number of stars, their luminosity, or cumulative mass, respectively;

$$n(\mathbf{x}) \equiv N\nu(\mathbf{x}) \tag{2.5}$$
$$j(\mathbf{x}) \equiv L\nu(\mathbf{x}) \tag{2.6}$$
$$\rho(\mathbf{x}) \equiv M\nu(\mathbf{x}), \tag{2.7}$$

since per definitionem $\int d^3\mathbf{x} d^3\mathbf{v} f(\mathbf{x}, \mathbf{v}, t) = 1$, and since all stars are identical and thus have the same mass and luminosity. It thus follows, since f appears only in first order in Eqn. 2.4, that n, j, and ρ can all be used as proxies for ν.

Usually ν is interpreted as being the mass density, implying that the stars constitute the mass distribution, and hence that the luminosity and mass profiles of the system are the same, so the system can be represented with a single mass-to-light

ratio. Such a state of affairs is inherent in Schwarzschild modelling since the potential has to be defined *a priori* in order to generate the library of stellar orbits; and it is typically derived from the de-projected stellar luminosity profile. While the linear superposition of orbits in the model has to fit the kinematics, one of the boundary conditions is to match the original luminosity profile (e.g. Thomas et al. 2004). The assumption of a constant mass-to-light ratio is also made explicitly in the Jeans models of Häring-Neumayer et al. (2006) and Neumayer et al. (2007). These authors model the kinematics of the gas, which they assume moves in a thin disk under the gravitational influence of the surrounding stars and black hole. This potential is defined as the sum of the black hole and stellar potentials, the latter being measured directly from the stellar luminosity profile under the assumption of spherical symmetry and a constant mass-to-light ratio.

However, the potential Φ can be separated from the distribution of stars, as we do in our approach in Chapter 4. In the following, we outline the details of our particular implementation for our data of NGC 6240. To achieve aforementioned separation, we keep the necessary assumption that all the stars contributing to the luminosity profile come from a uniform population; but we drop the assumption that the potential is defined by these stars – instead they only trace it. Thus we use the luminosity density j instead of ρ as a proxy for ν. In effect we are assuming that the stars are test particles, whose masses are identical but undefined. The luminosity profile traces the distribution of these test particles, since they all have the same luminosity. And Φ is simply the potential in which they are moving, but is not defined by the test particles themselves. We are therefore able to derive the potential from observations of L(r), v(r), and $\sigma(r)$, rather than requiring it *a priori* to follow L(r).

2.4.2 Choice of Model and specific Jeans Equation

In order to proceed, it is necessary to make some assumptions regarding the gravitational potential (defined by the combined mass of the stars, gas, and dark matter halo), the shape and isotropy of the nuclei and the stellar velocities and dispersions. A disky system would be characterised by $\sigma/v_{rot} \ll 1$, and an oblate spheroidal system, in which the dispersion provides non-rotational pressure support thickening the disk, by a $\sigma/v_{rot} \gtrsim 1$. Fig. 4.4 shows that for both nuclei in NGC 6240 $\sigma/v_{rot} \sim 1$, suggesting that the latter is the more physically realistic choice. However, this is non-trivial to implement (see for example van der Marel & van Dokkum 2007). Instead we make the simplifying assumption that both the stellar distribution and potential are spherically symmetric, which will allow us to capture the characteristics of the system. It also has the advantage of yielding an analytical solution, as we show below. We also adopt an isotropic dispersion, which can be justified because the data do not allow us to say anything about the form of anisotropy, and this choice represents the least informative, and hence least constraining, option (Ockham 1495; Dejonghe 1986).

Our assumptions above mean that the only streaming motion is azimuthal, so

that $\overline{v_r^2} = \sigma_r^2$, $\overline{v_\theta^2} = \sigma_\theta^2$, $\overline{v_\phi^2} = \overline{v_\phi^2} + \sigma_\phi^2$. In addition, isotropic dispersion means that $\sigma_\theta^2 = \sigma_r^2 = \sigma_\phi^2$, and thus equation 2.4 becomes

$$\frac{d(\nu\sigma^2)}{dr} - \frac{\nu}{r}v_\phi^2 = -\nu\frac{d\Phi}{dr}. \tag{2.8}$$

It should be noted that this is equivalent to the radial component of Euler's equation

$$\frac{\partial \mathbf{v}}{\partial t} + (\mathbf{v}.\nabla)\mathbf{v} = -\frac{1}{\rho}\nabla p - \nabla\Phi \tag{2.9}$$

for a fluid of density ν and pressure $\nu\sigma^2$.

For a spherically symmetric mass distribution,

$$\frac{d\Phi}{dr} = \frac{GM(r)}{r^2}. \tag{2.10}$$

(Newton 1687, but see also Einstein 1915). Combining Eqns. 2.8 and 2.10, we obtain an expression for M(r), the mass distribution giving rise to the potential governing the stellar motions:

$$M(r) = \frac{-1}{G}\left(\frac{r^2}{\nu}\frac{d(\nu\sigma^2)}{dr} - rv_\phi^2\right). \tag{2.11}$$

As outlined in §2.4.1, we wish to keep the potential and the stellar distribution as distinct quantities and therefore interpret $\nu(r)$ as the luminosity density $j(r) = L\nu(r)$ rather than as the mass density, maintaining the requirement that ν, σ, and v_ϕ trace a single population of stars. Note that this does *not* affect the gravitational potential – and thus the mass M(r) in Eqn. 2.11 – which is simply the gravitational potential in which the stars are moving, rather than the potential due to the mass of the stars for which we are solving the Jeans equation. Since $\nu(r) \propto j(r)$, and since $\nu(r)$ appears in first order in every term in equation 2.8, we can simply interchange the two. Thus Eqn. 2.11 becomes

$$M(r) = \frac{-1}{G}\left(\frac{r^2}{j}\frac{d(j\sigma^2)}{dr} - rv_\phi^2\right). \tag{2.12}$$

The crucial difference between our implementation of the Jeans models and those of others, where the simple relation $\rho(r) \propto L(r)$ is adopted, is that here the mass density depends not only on the luminosity profile, but also on the kinematics.

In order to assess the uncertainties of our result due to the choice of mass distribution, we also ran a set of models assuming an axisymmetric thin disk with an isotropic pressure component; the enclosed masses found with this model, which can be considered to be at the other end of the range of physically plausible models, agreed with the results of the spherically symmetric models within a factor of less than two. Häring-Neumayer et al. (2006) model the gas kinematics of Cen A with

three different Jeans models; an axisymmetric thin disk with and without pressure terms, and a spherically symmetric model. They find that the inferred black hole masses span less than an order of magnitude. Comparing their results with those of others, these authors find that, whilst favouring the pressure-supported thin disk model as the most physically plausible, the spherical Jeans model agrees best with the results from Schwarzschild orbit superposition modelling by Silge et al. (2005). The uncertainty of Jeans modelling results due to the unknown velocity dispersion anisotropy is more difficult to assess due to the degeneracy between the integrated mass and the anisotropy parameter β. Both Wolf et al. (2010) and Mamon & Boué (2010) attempt to quantify this (see Fig. 1 in Wolf et al. 2010 and Fig. 1 in Mamon & Boué 2010) in the case of mass measurements for the Carina dSph and DM haloes, respectively, finding that the range spanned by results for the integrated mass assuming extreme values of β are large at small physical radii, decreasing to less than a factor of two at radii comparable to or larger than the half-light radius (as is the case for our measurements). Since a spheroidal system like the one we modelled is unlikely to have extremely anisotropic velocity dispersions, the error due to our choice of $\beta=0$ is most probably less than a factor of two. We thus estimate that the uncertainties introduced by the assumptions inherent in our modelling are unlikely to be larger than a factor of two.

2.4.3   Justification of Applicability

The discussion above is based on the assumption that luminosity distributions in the nuclei consist of an ensemble of identical particles. Physically this is equivalent to requiring that, averaged over the PSF, the stellar population dominating the observed continuum is uniform. This needs to be justified – particularly in the case of NGC 6240 for which Tecza et al. (2000) have argued that the K-band continuum comprises both supergiants and an older population, and hence a spatially varying stellar composition is possible.

These authors deduced that the observable K-band continuum was dominated by supergiants rather than giants because a K4.5 I star gave a marginally better fit to the CO bandheads than a M3 III star. The signature of a population of late-type supergiants dominating the K-band continuum would be clearly visible in the map of EW_{CO} in Fig. 4.4 because K-M supergiants exhibit significantly deeper CO absorption features (15–17Å) than K-M giants (10–15 Å), which is deeper than for later-type dwarfs ($\sim$5 Å). This has been measured empirically for individual stars (Kleinman & Hall 1986; Origlia et al. 1993; Förster Schreiber 2000). It has also been demonstrated in stellar population synthesis models which show a peak of 16–17 Å for a 10 Myr old instantaneous burst, significantly above the typical 12 Å level for all other populations (Davies et al. 2007). That EW_{CO} is in the range 10–13 Å everywhere in the map clearly shows that supergiants do not dominate the observed population in the K-band, which is instead typified by late-type giants. Similarly, a crude estimate

of the global mass-to-light ratio using our Sérsic fits to the extinction corrected light profiles and $M_{dyn} = (v^2 + 3\sigma^2)R/G$ yields values of $10\,M_\odot/L_\odot$ (out to $250\,\mathrm{pc}$) and $4.5\,M_\odot/L_\odot$ (out to $320\,\mathrm{pc}$) for the northern and southern nuclei respectively – values that are about a factor of 2 more than the Jeans masses given in §4.7. Based on the tables of mass, luminosity, and colour for various stellar spectral types and luminosity classes (Tokunaga 2000; Drilling & Landolt 2000), we calculate mass-to-light ratios of late type (K0 to M0) supergiants to be $M/L_K < 0.01$, that for giants to be $M/L_K = 0.03$–0.3, and for main sequence stars $M/L_K = 40$–90. These ratios indicate that, as expected from population synthesis models, even on large scales it is late-type stars of luminosity class III–V that dominate the K-band continuum. Thus our assumption that the K-band continuum luminosity profile is, to first order, dominated by an ensemble of identical particles (specifically late-type giant and main sequence stars) appears to be justified.

Another condition which we need to justify is the continuity of the number of stars. To be physically realistic, we would need to include a sink and a source term in the continuity equation, as stars are constantly created and destroyed. Ignoring these terms is justifiable only if they are much smaller than the terms on the left-hand side of equation 2.2. As Binney & Tremaine (2008) show, this is the case if the fractional change in the number of stars per crossing time is small. Scaling a global star formation rate of $100\,\mathrm{M_\odot\,yr^{-1}}$, found by Springel et al. (2005c) to be a typical peak star formation rate during a gas-rich merger, to the size of the nuclei, and assuming a stellar mass of a few $10^9 M_\odot$ per nucleus, we find this fractional change per $t_{crossing}$ to be ~ 0.01 and hence can safely assume the continuity equation to apply.

2.4.4   Luminosity Profiles

The 2D luminosity distribution of both nuclei in NGC 6240 is asymmetric and shows complex substructure. In order to obtain a usable and meaningful representation of the overall intrinsic luminosity profile in each nucleus, it is necessary to smooth out this substructure and also avoid the region between the nuclei where the profiles must be strongly perturbed, as well as disregarding the luminosity contribution from the recent star formation. We have therefore subtracted the continuum associated with the Brγ emission (assuming an intrinsic $\mathrm{EW}_{Br\gamma}$ of $22\,\text{Å}$, as measured at the knot of Brγ emission north-west of the northern nucleus) and, after correcting for extinction, measured an azimuthally averaged profile using only a $180°$ wedge in the outside half (i.e. opposite the merger centre) of the galaxy. We have fitted a Sérsic function to the profiles, constraining it with the NIRC2 profile at $> 0.4''$, and with the extinction corrected SINFONI profile at $< 1.0''$ (i.e. some overlap between the two profiles is included). As part of the fitting process, the model profile was convolved in 2D with the SINFONI PSF, to account for beam smearing at small scales.

The extended NIRC2 data provided a strong constraint, and the models for both nuclei have an index n closer to the 4 one would expect for a de Vaucouleurs profile

than to the 1 for an exponential profile. The resulting effective radii are 490 pc for the northern nucleus and 180 pc for the southern nucleus. The fits also provide reasonable matches to the small-scale extinction-corrected SINFONI data. As such they appear to be representative of the global luminosity profiles for the two nuclei, and we use this parameterisation in both our Jeans modelling in §4.7 and when comparing the progenitors to the bulges of spiral galaxies in §4.10.

2.4.5 Profiles and Deprojection

The final step is to relate the variables in equation 2.12 to the observables we can extract from the data. As we can only measure the surface intensity $I(r)$ and line-of-sight dispersion σ_{LOS}, we need to deproject these to obtain the luminosity density j and intrinsic dispersion σ_{intr}. For a spherical system, these quantities are related via

$$\nu(r) = -\frac{1}{\pi} \int_r^{r_{max}} \frac{dI}{dR} \frac{dR}{\sqrt{R^2 - r^2}} \tag{2.13}$$

and

$$\nu(r)\overline{\sigma^2}(r) = -\frac{1}{\pi} \int_r^{r_{max}} \frac{d(I\sigma_{LOS}^2)}{dR} \frac{dR}{\sqrt{R^2 - r^2}}, \tag{2.14}$$

with R the projected radius. We use parameterisations of our data – Sérsic functions for the luminosity profiles, as outlined in §2.4.4, and polynomials for the dispersion profiles – and solve the above equations using *Mathematica*.

An important question arising is the choice of r_{max}, since it influences the deprojection results. Setting it to be infinite is impractical, and incorrect. A natural choice is the extent to which we can detect ordered rotation (~ 250 pc). To assess the impact of this choice, we deproject the luminosity profiles derived in §2.4.4, setting r_{max} to both 250 pc and 2.2 kpc; and compare the resulting luminosity density in the innermost 100 pc. We find the difference to be less than a few percent, indicating that r_{max} is not critical to the luminosity deprojection.

The impact of r_{max} on the deprojected dispersion is more noticeable, because σ_{LOS} does not decline as dramatically with radius as the luminosity profile. However, it is only consistent to use kinematic profiles (rotation and dispersion) covering the same spatial extent. We therefore truncate the dispersion deprojections at 250 pc and 320 pc for the northern and southern nucleus, respectively.

The dispersion profile we adopt is determined by azimuthally averaging the dispersion map in a wedge with opening angle 180°, pointing along the major axis of each nucleus and away from the system centre. This is done to avoid the regions of anomalously high dispersion between the nuclei which we have argued are not representative of the progenitors (see §4.6).

2.4.6   Rotation Curves

The rotation curves derived through kinemetry need to be corrected for beam smearing in order to recover the intrinsic kinematics, a procedure that is particularly important at small radii. However, in addition to beam smearing, projection along the line of sight also plays a role in flattening the observed rotation. This occurs because the nuclei are both thick and inclined. To recover the intrinsic rotation curve, we have modelled the mass distribution that can be supported solely by ordered rotation. In practice, we create a thin disk model for which we allow the light distribution to be uniformly extended above and below the disk. We use the dispersion profile as a constraint on the model, but only in the sense that the dispersion generated by spatial smearing of a steep high amplitude velocity gradient should not exceed the dispersion observed. The code we have used is described in Cresci et al. (2009), and accounts also for the beam smearing. In a first step, we estimate the impact of line-of-sight projection by putting all the mass in an unresolved point source, and adjusting the thickness of the model until the inner slope of the resulting rotation curve matches that observed. However, such models are ruled out because beam smearing effects on the intrinsic velocity field would alone lead to central dispersions higher than those observed. In a second step we therefore add an extended component, quantified as a Sérsic profile, while keeping the thickness fixed. We emphasize that this fitting procedure does not yield the mass distribution of the nuclei; it only addresses the mass that can be supported by the rotation and is used simply as a tool to estimate the intrinsic rotation curve.

For the northern nucleus the best model we can find for the mass supported by rotation consists only of a Sérsic profile, with a low index, and no additional compact component. This model provides an excellent match to the observed rotation curve, and the small increase in the central dispersion is still consistent with the flat dispersion profile observed. We therefore adopt it as the intrinsic velocity profile for the northern nucleus. Since the dispersion is nearly constant with radius, we adopt the mean value as a fixed intrinsic dispersion.

The southern nucleus is rather different. The rotation curve continues increasing as far as it can be measured, and the dispersion shows a peak at the centre. As one might expect, the model for this nucleus includes both an extended and a compact component. The central peak in dispersion is consistent with that observed, and the rotation curve again provides an excellent match to the data.

It must be stressed that the above analysis does *not* aim to derive mass profiles, but to obtain the intrinsic velocity and velocity dispersion as functions of radius. Using a mass model is simply a convenient way to model the rotation in order to assess what the impact of the PSF is and hence to recover the intrinsic rotation curve.

Chapter 3

Most Submillimetre Galaxies are Major Mergers

The work presented in this Chapter has been published as:

- "Most Submillimetre Galaxies are Major Mergers"
  Engel H., Tacconi L. J., Davies, R. I., Neri R., Smail I., Chapman S. C., Genzel R., Cox P., Greve T. R., Ivison R. J., Blain A., Bertoldi F., Omont A., 2010, ApJ, in press

3.1   Introduction

In Chapter 1 we explained the importance of SMGs in the context of high-redshift galaxy evolution, energy budget, and stellar mass assembly.

In this Chapter, we will critically examine the hypothesis that SMGs are mergers. We use observations of the CO line, which is unaffected by extinction, to trace the molecular gas, and combine both morphological and kinematic aspects in the analysis. We present new data for four SMGs. One of our sources has not been observed in CO before (SMM J105141), for the three other systems these new observations provide data of significantly increased resolution. This brings the number of SMGs observed to sub-arcsecond resolution from 8 to 12 and thus provides a significant increase in the total sample of high-resolution CO SMG observations. We complement these new data with previously published high resolution CO data for eight other SMGs (Greve et al. 2005; Hainline et al. 2006; Tacconi et al. 2006, 2008; Ivison et al. 2010; Bothwell et al. 2010), resulting in a much-improved statistical basis compared to e.g. Tacconi et al. (2006, 2008). Our work is distinctive to these preceding works, the aim of which was a general characterisation of the SMG population, not only in regard to sample size, but also objective. Here we tackle a specific, heretofore unsolved key issue – namely, whether or not SMGs are major mergers.

In §3.2 we detail our observations and data reduction. In §3.3.1 we explain the analyses employed, and in §3.3.2 we present results for individual systems. We then investigate merger mass ratios (§3.3.3), and sizes (§3.4.1) of our sample galaxies. In §3.4.2 we test stellar mass estimates from the literature, and discuss the implication of our results for cosmological models. We then bring these results together to discuss the trigger mechanism for the exceptional luminosities of SMGs in §3.4.3, before concluding in §3.5.

3.2   Observations & Data Reduction

The observations of four new SMGs were carried out in winter 2007/2008 with the IRAM Plateau de Bure interferometer, which consists of six 15 m-diameter telescopes (Guilloteau et al. 1992). We observed the four sources, SMM J09431, SMM J105141, SMM J131201, and HDF 169 under excellent weather conditions in the extended A-configuration, which has baselines up to 760 meters. The resulting spatial resolutions ranged from $0.4''$-$0.6''$(see Figs. 3.1-3.4). For the two $z \sim 3$ sources, SMM J09431 and SMM J131201, we observed the CO J = 6-5 line, which is redshifted into the 2 mm band. For the two sources at $z \sim 1.2$, SMM J105141 and HDF 169, we observed the CO J = 4-3 line in the 1 mm band. The observations were all made with the new generation, dual polarisation receivers, with system temperatures of $\sim$150 K and $\sim$200 K (SSB) in the 2 mm and 1 mm bands, respectively. The full available correlator capacity was configured to cover 1 GHz in each polarisation, which adequately covers the broad CO lines seen in SMGs (Genzel et al. 2003; Neri et al. 2003; Greve et al. 2005).

The total on-source integration times were 9.3 hours for SMM J09431, 12.7 hours for SMM J105141, 14.4 hours for HDF 169, and 20.1 hours for SMM J131204.

We calibrated the datasets using the CLIC program in the IRAM GILDAS package. Passband calibration used one or more bright quasars. Every 20 minutes we alternated source observations with a bright quasar calibrator within 15 degrees of the source. Our absolute positional accuracies are $\pm 0.2''$ or better. The absolute flux scale was calibrated on MWC 349 (1.35 Jy at $\sim$156 GHz and 1.6 Jy at $\sim$208 GHz). After flagging bad and high phase noise data, we created data cubes in the MAPPING environment of GILDAS. Final maps were cleaned with the CLARK version of CLEAN implemented in GILDAS. The absolute flux scale is better than $\pm 20\%$.

3.3 Results

Integrated spectra, integrated line flux maps, position-velocity diagrams, and velocity & velocity dispersion maps of the individual systems are displayed in Figures 3.1, 3.2, 3.3, & 3.4. Measured and derived source properties are listed in Tables 3.1, 3.2 & 3.3.

3.3.1 Analysis

Our analyses generally follow the procedures of Tacconi et al. (2006, 2008); for the computation of cold gas masses, we use the approach of Tacconi et al. (2010). Flux maps were produced by integrating the line emission, determining the line extent via visual inspection of spatially-integrated spectra. Fluxes are extracted from the line cubes by integrating over the area with significant emission. Given that the compact galaxies comprising a significant fraction of our sample here are in most cases only marginally resolved with the ~ 0.5-$1''$ spatial resolution available, we determine source sizes by fitting circular Gaussians to the systems in the uv-plane using the task UVFIT in the IRAM data reduction package GILDAS, and taking the Gaussian FWHM_{uv} to be the best estimate of the source's diameter. In the two individual galaxies of the four new systems where a Gaussian fit was not possible (most likely due to insufficient signal-to-noise), the beam FWHM was used as an upper limit to the source diameter. We note that these size measurements may slightly underestimate the actual size of the galaxies, since there may be faint extended flux below our sensitivity limit. We do not assign a formal uncertainty to this, since, if such a putative faint emission region exists, we do not know anything about its size or morphology. However the uncertainties due to this are unlikely to be significant.

Where possible, velocity and velocity dispersion maps were derived by fitting Gaussians to the line profiles. If the spectral signal-to-noise did not permit this, we produced moment maps of different velocity ranges, which were then overlaid as RGB-images.

Since the dispersions of our galaxies are comparable to or larger than the rotational velocities, dynamical masses have been derived using the 'isotropic virial estimator'

(e.g. Spitzer 1987; Tacconi et al. 2008; Förster-Schreiber et al. 2009) given in $M_\odot$ by

$$M_{dyn,vir} = 2.8 \times 10^5 \Delta v_{FWHM}^2 R_{1/2} \qquad (3.1)$$

where Δv_{FWHM} ($\mathrm{km\,s^{-1}}$) is the integrated line FWHM, and $R_{1/2}$ (kpc) is the the half-light radius (the radius within which half the total flux is emitted, here assumed to be equivalent to the Gaussian HWHM measured in the *uv*-plane). We note that the scaling factor appropriate for a rotating disk at an average inclination is a factor of ~ 1.5 smaller (Bothwell et al. 2010), i.e. if the above formula were applied to a disk galaxy, it would somewhat overestimate the dynamical mass. However, Cappellari et al. (2009b) find that this estimator agrees well with masses derived from more detailed Jeans modelling for a sample of massive $z \sim 2$ early-type galaxies.

In order to derive molecular gas masses, we convert the measured line fluxes to CO(1-0) fluxes (in $\mathrm{Jy\,km\,s^{-1}}$) using the results of SMG SED modelling (Fig. 3 of Weiss 2007, yielding $S_{CO(6-5)}/S_{CO(1-0)}$=13, $S_{CO(4-3)/CO(1-0)}$=10, $S_{CO(3-2)}/S_{CO(1-0)}$=7, $S_{CO(2-1)}/S_{CO(1-0)}$=3; the same numbers were also used by Bothwell et al. 2010 and Casey et al. 2009b). We assign an uncertainty of 30% to these conversions based on the differences between the individual SED models of Weiss (2007); in the four cases where we have flux measurements from two different transitions (Table 3.1) we find the flux ratios to be consistent with these conversion factors. We do not calculate gas masses based on CO(7-6) fluxes, since the conversion factor is uncertain for this transition. We then calculate the CO(1-0) line luminosities (in $\mathrm{K\,km\,s^{-1}\,pc^2}$) using Eqn. 3 of Solomon et al. (1997):

$$L'_{CO(1-0)} = 3.25 \times 10^7 S_{CO(1-0)} \Delta V \nu_{CO(1-0),rest}^{-2} D_L^2 (1+z)^{-1} \qquad (3.2)$$

with $S_{CO}\Delta V$ in $\mathrm{Jy\,km\,s^{-1}}$, $\nu_{CO(1-0),rest}$ in GHz, and D_L in Mpc. The CO(1-0) luminosities are then used to estimate the total gas mass via

$$M_{H_2} = \alpha L'_{CO(1-0)} \qquad (3.3)$$

using $\alpha = 1\,M_\odot\,/K\,km\,s^{-1}\,pc^2$ as measured for ULIRGs (Downes & Solomon 1998, for a discussion see also Genzel et al. 2010). For an in-depth discussion of this we refer the reader to Appendix A of Tacconi et al. (2008); we would like to stress that our choice of α is motivated by the surface densities of SMGs (cf. Table 10 of Tacconi et al. 2008) rather than any *a priori* assumption about a similarity between local ULIRGs and SMGs. Our choice of conversion factor is here further supported by the fact, that if for our SMGs the Milky Way conversion factor was adopted, in all but one case the gas mass would, rather implausibly, be equal to or larger than the dynamical mass. Finally, we apply a factor 1.36 correction to account for interstellar helium. We note that since the fluxes were measured in fixed apertures, and also some flux may be resolved out or be below our detection limit, the gas mass is likely to be somewhat larger than our estimates.

3.3.2 Results For Individual Objects

The detailed analyses of the molecular CO line emission in this Section reveal morphological and kinematic evidence that at least eight of the twelve SMGs studied in this Chapter are on-going mergers, and the remaining four are either disk galaxies or coalesced, late-stage mergers.

3.3.2.1 New Observations

SMM J09431 (z = 3.35) – a review of previous observations is given by Tacconi et al. (2006), who themselves presented CO(4-3) data. The system consists of two galaxies, H6 and H7, separated by ~ 30 kpc in projection, thus physically related and perhaps in an early stage of merging. Our new CO(6-5) data show a clear line spectrum for the south-west galaxy H7, with a global velocity gradient from -50 to $+70$ km s^{-1}, probably indicative of rotation. Förster-Schreiber et al. (2009) find that the commonly adopted boundary between 'dispersion-dominated' and 'rotation-dominated' systems of $v_{rot} \sim \sigma_0$ (where v_{rot} is the circular/orbital velocity and σ_0 is the intrinsic velocity dispersion) translates into $\sigma_{int}/v_{obs} \sim 1.25$ (where v_{obs} is the observed line-of-sight rotation and σ_{int} is the integrated line FWHM divided by 2.355). H7 has $\sigma_{int}/v_{obs} > 1.5$ nearly everywhere, i.e. appears dispersion-dominated. For the north-east galaxy H6, we detect a 4σ line shifted about $+210$ km s^{-1} relative to H7. Its width is 180 ± 65 km s^{-1}. There may also be broader and more redshifted emission extended over a larger region around H6 and towards H7, but at low significance. When deriving gas masses, the measured fluxes are corrected by a factor 1.3 for gravitational lensing effects, using the model of Cowie et al. (2002).

SMM J131201 (z = 3.41) – This system shows complex spatial and velocity distributions. There is no evidence of ordered rotation, although the extensions to the east and north-east are redshifted with respect to the emission peak. The substructures, which may be clumps, outflows, or tidal tails, and the overall lack of rotation most likely point towards an advanced, pre-coalescence merger stage. This conclusion is also drawn by Hainline (2008).

SMM J105141 (z = 1.21) – There are two galaxies separated in velocity by ~ 400 km s^{-1} and spatially by ~ 5 kpc, with no indications of disturbances. The south-west galaxy is about a factor 3 less luminous than its companion, but nearly equal in dynamical mass. The line profiles are well-resolved. The velocity field of the north-east system is indicative of a rotating disk, with velocities ranging from 60 to 180 km s^{-1}. Again we find that generally $\sigma_{int}/v_{obs} > 1.5$. It is likely that we are seeing two galaxies engaged in the early stages of merging, appearing close only in projection.

HDF 169 (SMM J123634+6212, z = 1.22) – The integrated spectrum of this compact galaxy is double-peaked, and its P-V diagram resembles a rotation curve, both indicative of a compact rotating system. It has a mass surface density of $\approx 10^{3.3} \mathrm{M}_\odot \, \mathrm{pc}^{-2}$. Tacconi et al. (2008) argued that the very high volume and surface densities characterising compact systems such as this could only plausibly be achieved during the
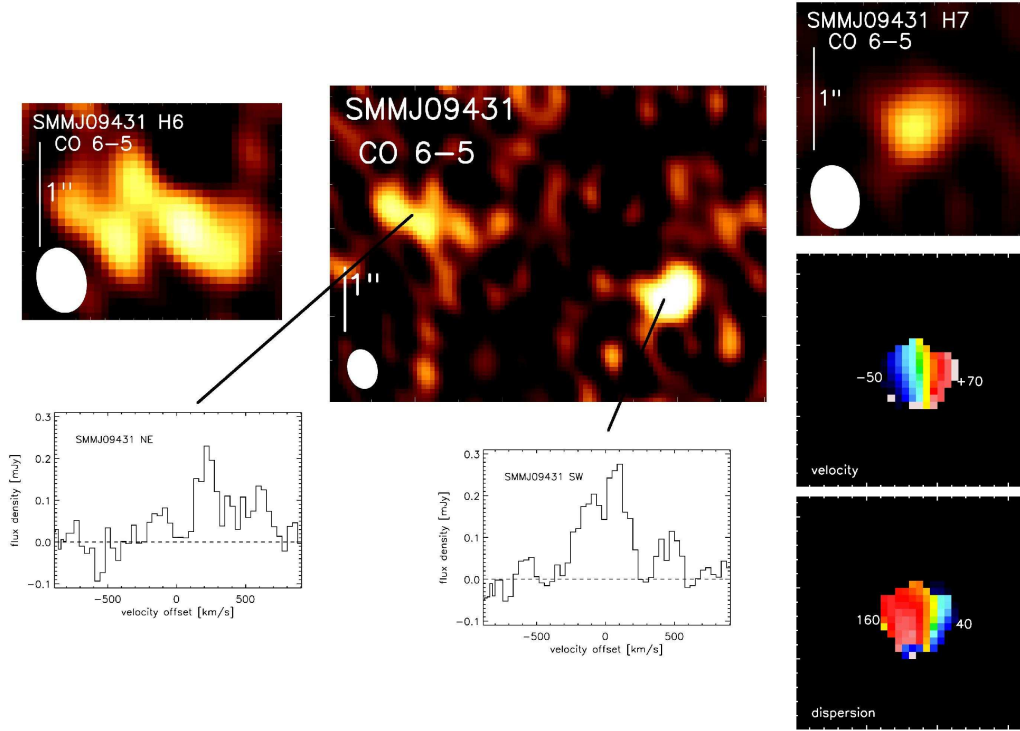
Figure 3.1: SMM J09431; this system consists of two galaxies separated by $\sim 30\,\text{kpc}$. The south-west one (H7) is a compact, rotating, dispersion-dominated disk galaxy. The left spectrum is of the north-east galaxy (H6), the right spectrum of the south-west galaxy. On the right are, top to bottom, south-west galaxy flux, velocity, and dispersion map, on the left north-east galaxy flux (the difference to the large-scale map being due to the H6 map having been integrated over the observed line extent rather than the full wavelength range) and integrated spectrum. The beam size ($0.64'' \times 0.48''$, P.A. $= 13.5°$) is displayed in the lower left corner of the flux maps. North is up and east is to the left. Scale bars denote $1''$.

final stages of a major merger. However we feel that this argument alone here is insufficient to judge with any degree of certainty whether this object is a quiescent disk galaxy or a late-stage merger.

3.3.2.2   Re-Analysis Of Existing Observations, & Published Results

We have re-analysed previous observations of HDF 242 (SMM J123707+614, $z = 2.49$, Tacconi et al. 2006) and N2850.4 (SMM J163650+4057 and SMM J16368+4057, $z = 2.38$, Tacconi et al. 2006) using the methods described in Section 3.3.1 (see Table 3.1). We also complement our data with published results from CO line observations by Tacconi et al. (2006, 2008) and Bothwell et al. (2010) for five other systems; HDF 76 (SMM J123549+6215, $z = 2.20$), N2850.2 (SMM J163658+4105, SMM J16370+4105,
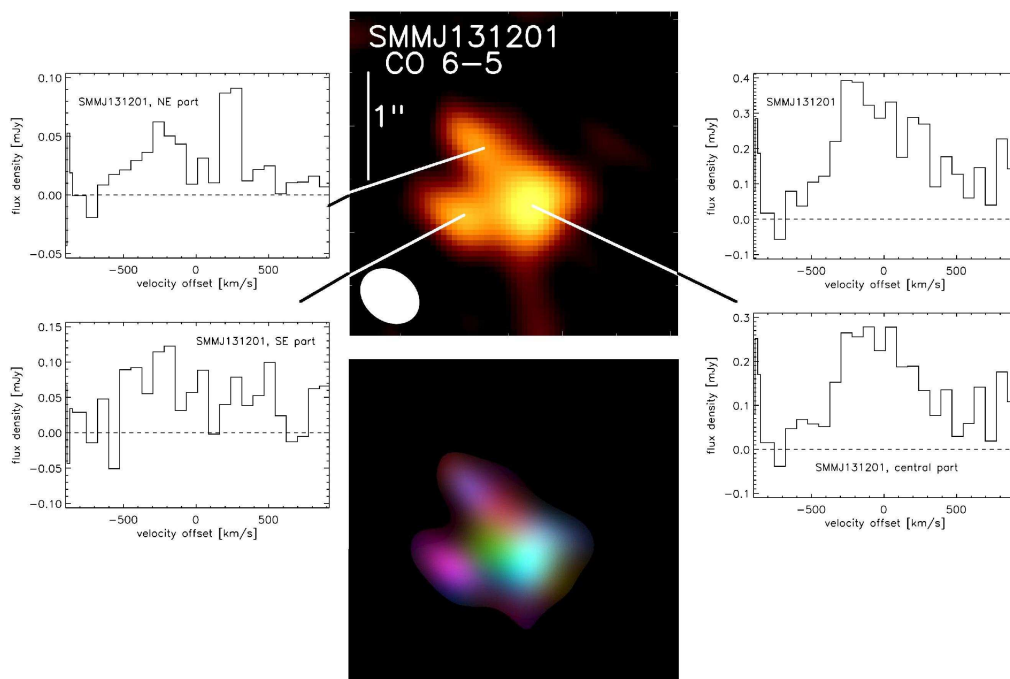
Figure 3.2: SMM J131201; this system displays a complex, irregular morphology, it most likely is an advanced pre-coalescence merger. The RGB-image (mapping red, green, and blue parts of the spectrum) shows no indication of rotation. Spectra are, left: north-east (top) and south-east (bottom) arm, right: entire system (top), and central part (bottom). The beam size $(0.59'' \times 0.47''$, P.A. $= 50.9°)$ is displayed in the lower left corner of the flux maps. North is up and east is to the left. Scale bar denotes $1''$.
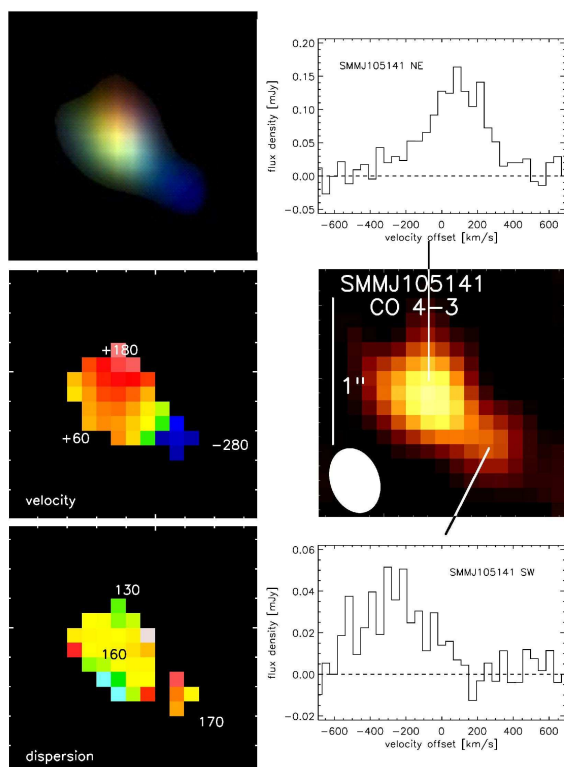
Figure 3.3: SMM J105141; as the RGB-map (top; mapping red, green, and blue parts of the spectrum) clearly shows, this system consists of two galaxies that are separated in velocity by $\sim 400\,\mathrm{km\,s^{-1}}$. Top right spectrum is of 'main' component (north-east galaxy), bottom right spectrum of the blue-shifted component (south-west galaxy). As can be seen from the velocity and dispersion maps (left, middle and bottom), the north-east galaxy is a dispersion-dominated disk galaxy. The beam size ($0.46'' \times 0.34''$, P.A. $= 28.7°$) is displayed in the lower left corner of the flux maps. North is up and east is to the left. Scale bar denotes $1''$.
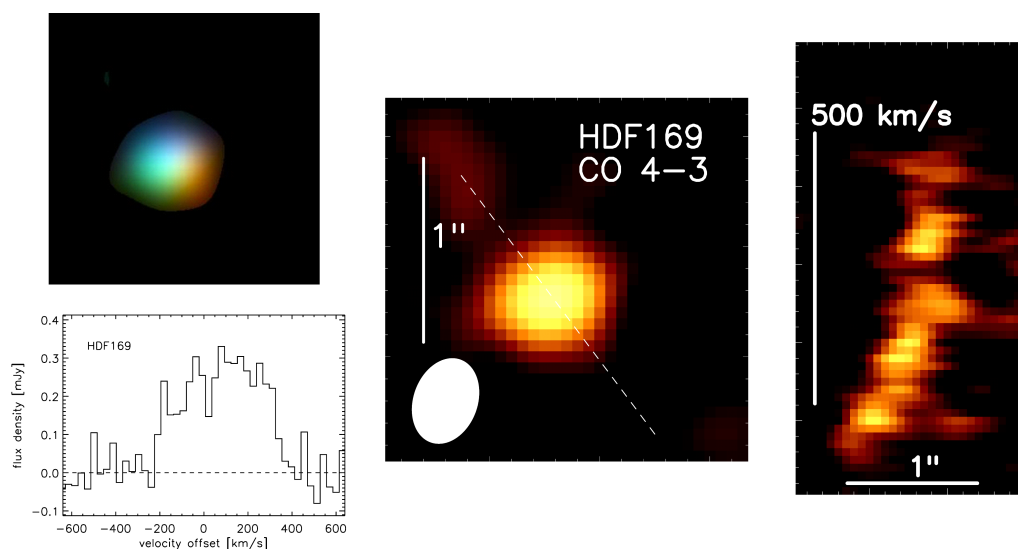
Figure 3.4: HDF 169; the position-velocity diagram (taken along the dotted line shown in the flux map, from lower right to upper left) and RGB-map (mapping red, green, and blue parts of the spectrum) indicate rotation, which is also supported by the integrated spectrum which appears double-peaked. This galaxy thus could either be a disk galaxy or a compact, rotating coalesced merger remnant. The beam size $(0.48'' \times 0.35'', \text{P.A.} = 161°)$ is displayed in the lower left corner of the flux maps. North is up and east is to the left. Scale bar denotes $1''$.

and SMM J16366+4105, $z = 2.45$), SMM J044307+0210 (SMM J04431+0210, $z = 2.51$), HDF 132 (SMM J123618.33+621550.5, $z + 2.00$), and Lockman 38 (SMM J105307+572431.4, $z = 1.52$), where possible re-calculating derived quantities to bring them into a consistent methodological framework. Finally, we include results from new multi-wavelength observations of SMM J02399-0136 (Genzel et al. 2003; Ivison et al. 2010). The published results on the kinematics and morphologies of these systems are summarised below:

SMM J044307+0210 – This lensed galaxy appears compact and has a double-peaked line profile with a FWHM of $\sim 350\,\mathrm{km\,s^{-1}}$.

HDF 242 – a wide binary with a separation of $\sim 22\,\mathrm{kpc}$.

N2850.4 – The CO(3-2) data show a double-peaked line profile and a separation of $\sim 3.3\,\mathrm{kpc}$ between the peaks of the red and blue channel maps. The integrated emission in the higher resolution CO(7-6) data directly shows two peaks separated by $\sim 3.7\,\mathrm{kpc}$. This system is therefore interpreted as a close binary. We infer a mass ratio of 0.68 from the flux ratios of the two components.

HDF 76, N2850.2, & HDF 132 – All compact sources with double-peaked line profiles. They could be either coalesced major mergers, or massive disk galaxies. They have extremely high mass surface densities of $10^{3.5}$, $10^{4.5}$, and $10^{4.0} M_\odot\,\mathrm{pc^{-2}}$ respectively (Tacconi et al. 2008; Bothwell et al. 2010), at least an order of magnitude larger than those measured in the UV/optically-selected SINS galaxies (Förster-Schreiber et al. 2006, 2009; Tacconi et al. 2008) and comparable to those measured in the central nuclear gas disk of Arp 220. Tacconi et al. (2008) argue, that to achieve this, the torques provided by a highly dissipative, major merger are necessary.

Lockman 38 – Bothwell et al. (2010) interpreted this object as a very late-stage merger, having two kinematically distinct components that are not spatially resolved.

SMM J02399-0136 – New multi-wavelength observations (Ivison et al. 2010) reveal that this system consists of at least two major components (most likely three, two of which host a BH); it is therefore interpreted as an on-going merger.

3.3.3   Mass Ratios

Ivison et al. (2002) first noted a preponderance of radio doubles among SMGs. With a larger sample, Ivison et al. (2007) were able to demonstrate that the likelihood of SMGs having companions within a few arcseconds is significantly larger than would be expected by chance. This overdensity suggests that at least a significant fraction of SMGs may currently be undergoing mergers. We are able to refine this picture substantially by investigating the mass ratios of the merging components. Five of the twelve SMGs in our sample consist of spatially separated interacting galaxies, and we are able to measure mass ratios for four of them (Table 3.2; SMM J09431, SMM J105141, HDF 242, N2850.4; no mass estimates for the individual components of SMM J02399 are published). In all cases the mass ratios are consistent with being *major* (mass ratios of 1:3 or closer to unity) mergers. It must be kept in mind that

galaxy	obs. CO transition	$S_{CO}\Delta V$ [Jy km s^{-1}]	$HWHM_{uv}$ [kpc]	v_{FWHM} [km s^{-1}]	M_{gas} [$10^{10}M_\odot$]	M_{dyn} [$10^{10}M_\odot$]
SMM J09431, SW	6-5[a]	1.8±0.3	1.13±0.23	390±45	7.10±2.44	4.81±1.26
	4-3[c]	1.1±0.2	1.85±0.60	400±45	5.64±1.98	8.29±2.99
	1-0[f]	<0.13	n/a	n/a	<8.67	n/a
SMM J09431, NE	6-5[a]	1.1±0.2	n/a	n/a	4.34±1.53	n/a
	4-3[c]	<0.4	n/a	n/a	<2.05	n/a
SMM J131201	6-5[a]	2.54±0.1	4.09±0.51	911±140	13.43±4.97	95.04±23.81
	4-3[e]	1.7±0.3	n/a	530±50	11.67±4.06	n/a
	1-0[f]	0.42±0.07	n/a	1040±190	28.83±4.81	n/a
SMM J105141, SW	4-3[a]	1.53±0.11	<1.40	436±50	1.63±0.51	<7.45
SMM J105141, NE	4-3[a]	5.87±0.19	1.77±0.14	383±50	6.72±1.89	7.27±1.46
HDF 169	4-3[a]	2.25±0.11	2.15±0.24	431±60	2.45±0.75	11.18±2.53
	2-1[h]	3.45±0.93	<16.5	560±90	12.47±5.03	<145
HDF 76	6-5[b,c]	2.3±0.4	0.95±0.4	600±80	5.76±2.00	9.58±4.42
	3-2[b,c]	1.6±0.2	<2.1	600±50	7.44±2.42	<21.17
HDF 242, SW	3-2[a,b,c]	0.59±0.08	2.51±0.86	426±60	3.41±1.13	12.75±5.10
HDF 242, NE	3-2[a,b,c]	0.32±0.07	3.45±0.98	394±60	1.85±0.68	15.00±5.35
N2850.2	7-6[b,c]	3.3±0.5	0.8±0.5	790±50	n/a	13.98±8.83
	3-2[c,e]	1.8±0.2	n/a	800±50	10.11±3.23	n/a
N2850.4, total	3-2[b,c]	2.3±0.3	2.48±1.24	710±50	12.28±4.02	35.00±17.85
N2850.4, SW	7-6[a,b,c]	2.01±0.18	0.54±0.37	373±50	n/a	2.10±1.50
N2850.4, NE	7-6[a,b,c]	1.36±0.18	<1.70	139±50	n/a	<0.92
SMM J044307	3-2[c]	1.4±0.2	<3.26	350±40	8.20±2.73	<11.18
SMM J02399	1-0[d]	n/a	n/a	n/a	100±30	n/a
HDF 132	4-3[g]	1.27±0.14	2.65	n/a	3.49±1.12	21.80±1.80
Lockman 38	3-2[g]	0.63±0.08	4.75	n/a	1.49±0.49	6.20±1.10

[a] this work
[b] Tacconi et al. (2008)
[c] Tacconi et al. (2006)
[d] Ivison et al. (2010)
[e] Greve et al. (2005)
[f] Hainline et al. (2006)
[g] Bothwell et al. (2010)
[h] Frayer et al. (2008)

Table 3.1: Measured quantities for the twelve systems in our sample. If a system consists of two galaxies, SW or NE indicates which galaxy is referred to. As outlined in the text, the HWHM of Gaussian fits to the source in the uv-plane were taken as best estimates of the intrinsic $R_{1/2}$, except for HDF 132 and Lockman 38, for which the half light radii as quoted by Bothwell et al. (2010) are given. The quoted values for dynamical masses were calculated using the 'isotropic virial estimator' (see §3.3.1 for details), except for HDF 132 and Lockman 38, for which Bothwell et al. (2010) estimated the quoted masses using disk rotation models. Gas masses were calculated by converting the measured line flux to CO(1-0) flux using Fig. 3 of Weiss (2007), assuming a ULIRG conversion factor $\alpha = 1\, M_\odot\, /K\, km\, s^{-1}\, pc^2$, and including a factor 1.36 correction for helium. For SMM J09431, measurements were corrected for gravitational lensing magnification of factor 1.3 (Cowie et al. 2002). If a source was unresolved, the beam HWHM was taken as an upper limit to $R_{1/2}$.

galaxy	z	proj. sep. [kpc]	mass ratio (gas)	mass ratio (dyn)
SMM J09431[a,c]	3.35	30±3	0.41±0.2	n/a
SMM J131201[a]	3.41	≤6	n/a	n/a
SMM J105141[a]	1.21	4.9±0.5	0.26±0.02	>0.98
HDF 169[a]	1.22	≤1.5	coal.	coal.
HDF 76[b,c]	2.20	≤2	coal.	coal.
HDF 242[a,b,c]	2.49	22±2	0.54±0.14	0.85±0.49
N2850.2[b,c]	2.45	≤3	coal.	coal.
N2850.4[a,b,c]	2.38	3.7±0.4	0.68±0.11	<0.44
SMM J044307[c]	2.51	≤4	coal.	coal.
SMM J02399[d]	2.80	∼8	n/a	n/a
HDF 132[e]	2.00	≤3	coal.	coal.
Lockman 38[e]	1.52	≤4	coal.	coal.

[a] this work
[b] Tacconi et al. (2008)
[c] Tacconi et al. (2006)
[d] Ivison et al. (2010)
[e] Bothwell et al. (2010)

Table 3.2: Projected separations and mass ratios. Coal. denotes coalesced system. The distribution of projected separations is also plotted in Fig. 3.5. For SMM J09431, the CO(6-5) data presented in this work were used to derive the gas mass ratio. For SMM J02399, no information on dynamical or gas masses of the subcomponents was available in the literature. As can be seen, the mass ratios are all consistent with major (mass ratio 1:3 or larger) mergers, within the error ranges.

if these are mergers between disk galaxies, the dynamical masses may be over- or underestimated due to the dependence on viewing angle, and hence the uncertainties on these mass ratios are somewhat larger than the propagated errors stated in Table 3.2. All measured spatial separations ($\lesssim 30$ kpc) are well within the range where they would be deemed gravitationally interacting, and the masses of individual components are $\gtrsim 10^{10} M_\odot$, much larger than clumps in a single galaxy (Förster-Schreiber et al. 2009).

We furthermore note that, as Bothwell et al. (2010) outline, one can also make a strong case for Lockman 38 and HDF 132 being mergers; they show clear indication of two kinematically distinct components, which are however not individually spatially resolved. Bothwell et al. (2010) calculate the mass ratios of the two subcomponents to be 0.24±0.18 and 0.68±0.14, respectively. However, since these two objects cannot unambiguously be classified as mergers, we do not include them in Table 3.2.

3.4 Interpretation and Discussion

3.4.1 Sizes

Size measurements of SMGs based on CO interferometric and mm-continuum data have indicated that these galaxies are compact, with median diameter ≤ 4 kpc (FWHM of Gaussian fitted to source in *uv*-plane; Tacconi et al. 2006). On the other hand, based on the diameter at the 3σ detection level of MERLIN and VLA radio observations, Chapman et al. (2004) find the star formation to be 'occurring on ~ 10 kpc scales'. However, Tacconi et al. (2006) and Biggs & Ivison (2008) point out that the size measurements from the MERLIN and VLA data are consistent with the CO size when a comparable method (deconvolved major axes of Gaussians fitted to the emission) is applied. They find a median diameter of ~ 5 kpc for their sample. We can compare radio and CO size measurements individually for two objects in our sample. For SMM J105141 Biggs & Ivison (2008) measure an overall radio size of $0.61'' \times 0.44''$, or 5.1 kpc $\times$ 3.68 kpc; we measure a CO(4-3) FWHM of 3.54 kpc for the main component of this two-galaxy system. For HDF 169, we find a CO(4-3) FWHM of 4.3 kpc and measure 4.5 kpc from an unpublished MERLIN radio map. Thus there appears to be good agreement between CO(4-3) and radio extents in these two cases. Younger et al. (2008, 2010) measure the scale of far-infrared emission of four SMGs to be ~ 5-8 kpc. This is somewhat larger than what we find for the sample discussed here (although Younger et al. 2008 say that their results are 'qualitatively consistent with the results of Tacconi et al. 2006'). The most plausible explanation for the difference – beside the possibility that CO lines and far-IR continuum trace slightly different things – lies in the fact that the Younger et al. (2008, 2010) SMGs probe the brightest end of the luminosity distribution, with $S_{870\mu m} \gtrsim 15$ mJy.

For our augmented sample, which contains all SMGs for which sub-arcsecond resolution interferometric CO observations are available (which are not strongly lensed),
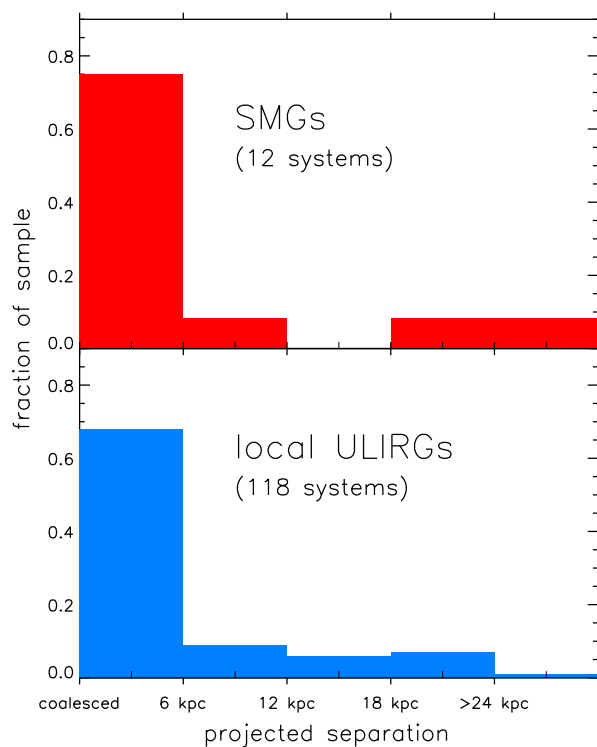
Figure 3.5: Distribution of projected separations. Red: SMGs, this work, 12 systems. Blue: local ULIRGs, Veilleux et al. (2002), 118 systems. Note that the last bin contains all systems with projected separations larger than 24 kpc. We note that for the SMGs, of the 9 systems in the first bin (projected separation smaller than 6 kpc), 7 are either poorly resolved or coalesced, and 2 are clearly recognisable as close binaries; the SMG sample thus divides into 5 well-resolved binary systems and 7 which are either poorly resolved or clearly compact, rotating systems. It should be noted that $\sim 64\%$ of local ULIRGs have projected separations ≤ 2 kpc, however due to the larger upper limits of some of the SMGs, and the increased uncertainties of a finer resolution (due to our small sample size), we have opted to use a coarser resolution. It is evident that SMGs and local ULIRGs display a very similar distribution of projected separations.

we have measured FWHM sizes for eleven galaxies (measuring each galaxy individually in the case of wide binaries). We find average and median FWHMs of 4.5 and 4.3 kpc, with a 1-σ distribution of 2.8 kpc, slightly larger than the results of Tacconi et al. (2006). We are unable to identify a plausible explanation for this, other than small number statistics (Tacconi et al. 2006 measure sizes for five systems, and upper limits for a further four; here we have size measurements for twelve systems). We also obtain upper limits of 3.4, 6.5, and 2.8 kpc for three other sources (Table 3.1).

We note that here we are collating measurements from a range of CO transitions, from (7-6) to (1-0), which may trace physically different environments. As Tacconi et al. (2008) elaborate, transitions up to $J \approx 5\text{-}6$ should all provide reasonable tracers of the overall molecular gas. However, the extent to which, say, CO(2-1) and CO(6-5) trace the same gas, is still on-going (see also Narayanan et al. 2010b). That the CO(7-6) may trace denser gas might explain the comparatively small source sizes for N2850.2 and N2850.4, and hence be at least partially responsible for the small dynamical masses we derive for these two galaxies (see also the discussion in Danielson et al. 2010). In the one case where we have a size measurement from two different transitions (SMM J09431 SW; J = 4 & J = 6), the two numbers are consistent within the uncertainties. Restricting to size measurements from $J \leq 6$ observations yields average and median FWHMs of 5.2 and 5.0 kpc, with a 1-σ distribution of 2.6 kpc.

Thus both radio and CO measurements are consistent with SMGs having FWHM sizes of ~ 5 kpc.

3.4.2 Stellar Mass Measurements, and their Implications for Cosmological Models

In this Section, we use our dynamical and gas masses to test stellar mass estimates. This is motivated by the large systematic uncertainties associated with stellar mass measurements, and the implications that a reliable determination of the stellar mass has both for a critical assessment of competing cosmological models of SMGs, as well as for the co-evolution of central black holes and their hosts (e.g. Hainline et al. 2010).

3.4.2.1 Stellar Mass Measurements

Hainline (2008) (see also Hainline et al. 2010) derived the stellar masses of a large sample of SMGs, employing *Spitzer* observations to cover a significantly larger spectral range than earlier attempts (e.g. Smail et al. 2004). The Hainline (2008) data set was also used by Michałowski et al. (2010) to derive stellar masses. But despite using an identical observational data base, their results are very different: Hainline (2008) find a median stellar mass of 6.3-6.9 $\times 10^{10} M_{\odot}$, whereas Michałowski et al. (2010) arrive at a median of $3.5 \times 10^{11} M_{\odot}$. Therefore, testing these results is essential and the next key step towards deriving the stellar mass content of SMGs reliably.

Table 3.3 brings our dynamical and gas masses together with the stellar masses

from Hainline (2008) and Michałowski et al. (2010) for the seven systems in common, and includes gas masses for two more galaxies based on flux measurements of Greve et al. (2005). We also show the stellar masses derived by Tacconi et al. (2008). As noted in §3.3.1, our dynamical masses may be underestimated due to undetected faint extended flux leading to somewhat smaller $HWHM_{uv}$. However, since this effect would be small and also the gas masses correspondingly larger, this is very unlikely to qualitatively impact on our conclusions here. We furthermore note that we have neglected both dust and dark matter in our mass budget here. Dust is unlikely to contribute more than a few percent, and Genzel et al. (2009) find the dark matter content in the central few kpc of high-z galaxies to be 10-20%. Thus, whilst not negligible, these will not have a significant impact on the mass budget, and we have opted not to include it here for sake of simplicity. We have converted the stellar mass estimates from a Salpeter (1955) to a Chabrier (2003) IMF by reducing them by a factor 1.7 (Hainline 2008). This is supported by Bastian et al. (2010), who find no conclusive evidence that an IMF different to the locally applicable Chabrier (2003) or Kroupa (2001) forms should be in place at high redshifts. Cappellari et al. (2009b) also find that a Chabrier (2003) instead of a Salpeter (1955) IMF is required to bring the stellar masses derived for a sample of z $\sim$ 2 early-type galaxies via SED modelling in agreement with their dynamical masses calculated from Jeans models.

We find that $(M_{gas} + M_{\star})/M_{dyn}$ for the seven galaxies for which all three mass estimates are available, has an average (median) of 0.8 (0.9) for the adjusted Hainline (2008) stellar masses (with a 1-σ distribution of 0.5); whereas for the adjusted Michałowski et al. (2010) masses, the average (median) is 2.1 (2.1), with a 1-σ distribution of 1.2. We conclude that the Hainline (2008) stellar masses, adjusted to a Chabrier (2003) IMF, are consistent with our independent mass measurements (Fig. 3.6).

3.4.2.2   Implications for Cosmological Models

Two different approaches to reproduce the sub-millimetre galaxy population in cosmological hydrodynamical simulations are currently being pursued. In semi-analytic models (e.g. Swinbank et al. 2008), the high sub-millimetre luminosities are achieved through bursts of star formation induced in gas-rich major mergers; whereas numerical simulations have also invoked 'cold accretion flows'. In the latter SMGs are assumed to be massive galaxies sitting at the centres of large potential wells, constantly forming stars at high rates sustained by smooth infall and accretion of gas-rich satellites (e.g. Davé et al. 2010).

Both models have shortcomings (such as cold accretion flows being unable to explain the short SMG lifetimes, Tacconi et al. 2008) and it is likely that both models are fundamentally limited by our current understanding of the role of gas physics inside the haloes. As Benson & Bowers (2010) show, implementation of cold mode accretion into semi-analytic models does not translate into a significant difference

	M_{gas} $[10^{10}M_\odot]$	M_{dyn} $[10^{10}M_\odot]$	$M_\star^{\mathrm{a}}$ $[10^{10}M_\odot]$	$M_\star^{\mathrm{b}}$ $[10^{10}M_\odot]$	$M_\star^{\mathrm{c}}$ $[10^{10}M_\odot]$
SMM J131201	18.0±9.4	95.0±23.8	n/a	$10.2^{+4.9}_{-3.3}$	13.5
HDF 169	7.5±5.0	11.2±2.5	n/a	$3.2^{+1.1}_{-0.8}$	26.9
HDF 76	6.6±1.6	9.6±4.4	12^{+4}_{-3}	$10.2^{+11.1}_{-5.3}$	28.2
HDF 242 (SW + NE)	5.3±1.3	27.8±7.4	$12^{+2.5}_{-4.5}$	$3.7^{+1.4}_{-1.0}$	52.4
N2850.2	10.1±3.2	14.0±8.8	25±7.5	$3.2^{+1.3}_{-0.9}$	34.6
N2850.4 (SW + NE)	12.3±4.0	35.0±17.9	23^{+11}_{-7}	$17.4^{+12.8}_{-7.4}$	21.9
HDF 132	3.5±1.1	21.8±1.8	n/a	$2.09^{+0.9}_{-0.6}$	29.5
SMM J16371+4053	5.3±1.1	n/a	n/a	$4.6^{+1.7}_{-1.3}$	47.8
SMM J22174+0015	6.7±1.7	n/a	n/a	$3.4^{+3.7}_{-1.8}$	13.8

[a] Tacconi et al. (2008)

[b] Hainline (2008)

[c] Michałowski et al. (2010)

Table 3.3: Stellar, gas, and dynamical mass measurements for the seven galaxies which are contained both in our sample and those of Michałowski et al. (2010) and Hainline (2008), and two additional galaxies contained in the latter two samples for which we calculate gas masses using fluxes measured by Greve et al. (2005). Michałowski et al. (2010) do not quote uncertainties for their stellar masses. Stellar masses were corrected for a Chabrier (2003) IMF. Binaries are treated as one system. Where multiple transitions were observed, dynamical and gas masses are averages of those derived for the different transitions, see Table 3.1. As can be seen, the stellar masses derived by Michałowski et al. (2010) are significantly larger than those of Hainline (2008), with only the latter being in good agreement with our gas and dynamical mass measurements.
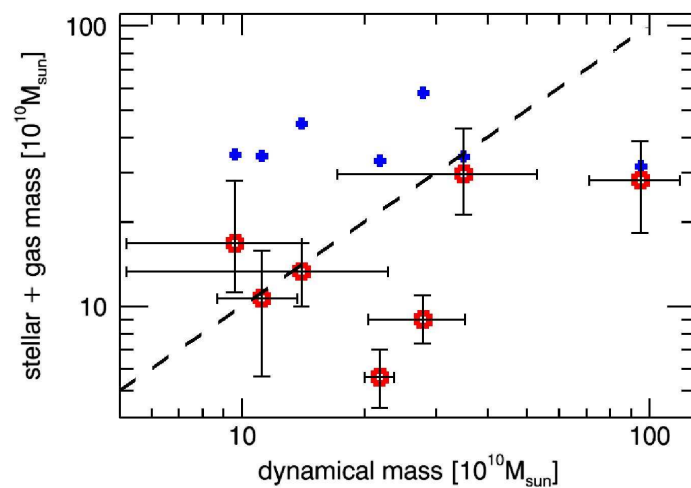
Figure 3.6: $(M_{gas} + M_\star)$ vs M_{dyn} for the seven galaxies for which all three mass estimates are available (Table 3.3). Blue crosses denote Michałowski et al. (2010) stellar masses, red squares those of Hainline (2008); both corrected for a Chabrier (2003) IMF. Michałowski et al. (2010) do not quote uncertainties for their stellar masses. The dashed line demarcates $M_{gas} + M_\star = M_{dyn}$; in order for the mass estimates to be physically realistic, galaxies should lie on or below this line. Within the errors, the Hainline (2008) stellar masses pass this test, whereas those of Michałowski et al. (2010) do not. This constitutes strong support for the Hainline (2008) results.

in cosmic star formation history compared to previous models; this may indicate that a more crucial aspect is how the stability of the cold gas inside the haloes is modelled. Equally, the assumptions underlying the numerical simulations have not been fully tested as it is computationally challenging to run large numbers of galaxies in these models to $z = 0$ to compare their properties to the observations of local galaxy populations (e.g. luminosity function, colour-luminosity relation) to confirm that they reproduce these. Clearly, a detailed discussion of this is beyond the scope of this work. Instead, here we will look at the stellar masses predicted by the current implementations of each approach, and how these compare to the adjusted Hainline (2008) masses.

Currently, both models have the difficulty that if the number density of SMGs is matched, then with a standard IMF, they underpredict the luminosities/SFRs and vice versa (Davé et al. 2010). This may be due to systematics in the simulations (Swinbank et al. 2008) or the inferred properties of observed SMGs (Davé et al. 2010). A key difference between the models is the stellar mass required to match the observed number density. In the cold accretion flow models, SMGs are the most massive galaxies and have a median stellar mass of $2.7 \times 10^{11} M_\odot$ (Davé et al. 2010). In the semi-analytic models, the declining stellar mass function, major merger rate and brief SMG phase push the predicted stellar mass down and the median is an order of magnitude lower at $\sim 2.1^{+3.0}_{-1.0} \times 10^{10} M_\odot$ (Swinbank et al. 2008). In Section 3.4.2 we showed it is the lower stellar masses, calculated by Hainline (2008) and corrected to a Chabrier (2003) IMF, that are physically more plausible for SMGs. The adjusted median stellar mass for their 64 SMGs is $3.9 \times 10^{10} M_\odot$, consistent with what is required by semi-analytic models. We therefore conclude that, although the associated uncertainties are certainly non-negligible, SMG stellar mass measurements strongly disfavour cold accretion flow models, and are compatible with hierarchical merging models.

3.4.3 What Triggers The Exceptional Luminosity of SMGs?

It has previously been conjectured, based primarily on radio and rest-frame UV morphologies, that the high luminosities of SMGs are triggered by merger activity. Our analysis in Section 3.3 of the CO emission shows convincing evidence that at least a majority of our twelve SMGs are indeed mergers. And in particular, we have found that all binary SMGs where we could derive mass ratios the merger partners are near-equal in mass, i.e. they are *major* mergers. Thus, while it is beyond doubt that *some* SMGs are triggered by major mergers, the question of the nature of the compact, non-binary SMGs comprising a significant fraction of the overall SMG sample is yet to be settled conclusively - are they end-stage major mergers, or isolated disk galaxies?

In the following we will develop the argument that they mostly are end-stage major mergers, since a major merger will be detectable as an SMG for a significant

amount of time spent in the 'final coalescence' phase – and thus that the large fraction of observed binary SMGs imply a correspondingly large number of single SMGs which are coalesced major mergers.

An illustrative comparison can be made with local ULIRGs, known to be exclusively major mergers. As Fig. 5 of Veilleux et al. (2002) shows, $\sim 64\%$ of local ULIRGs are either coalesced, or have projected nuclear separations $\leq 2\,\mathrm{kpc}$. This is what is expected from merger simulations (Mihos & Hernquist 1996; Springel et al. 2005b), which show that a first, minor starburst is triggered upon the first encounter, and the most prodigious star formation rates are only achieved during the final coalescence of the two galaxies, when tidal torquing compresses gas into the centre and leads to a $\sim$kpc-scale central starburst. Could it be that the SMG selection criterion selects a similar class of galaxies, at high redshift, and thus that the large fraction of compact SMGs in our sample is naturally explained as being those end-stage, coalesced major merger products? Indeed, as Fig. 3.5 shows, local ULIRGs and our SMG sample show a strikingly similar distribution of projected separations (here we have chosen to adopt a coarser bin size than Veilleux et al. 2002, due to the comparatively small SMG sample size and the relatively large upper limits on some SMG sizes – we note that most of the local ULIRGs in the $\leq 6\,\mathrm{kpc}$ bin have projected separations $\leq 2\,\mathrm{kpc}$). However, a direct comparison of the two samples is difficult. This is because L_{IR} and $S_{850\mu m}$ may not always be correlated during a major merger, due to the way the infrared SED changes with dust temperature at these redshifts – for a given L_{IR}, $S_{850\mu m}$ decreases with increasing dust temperature. This results in a cool dust bias in the SMG sample, illustrated by Fig. 4 of Casey et al. (2009a), and borne out by observations (Magnelli et al. 2010). This is important, since it may affect which merger stages are sampled by L_{IR} and $S_{850\mu m}$ selection, respectively: Both observations and simulations indicate that dust temperatures increase towards the final stages of a merger, suggesting that SMGs should sample earlier merger stages than ULIRGs. Does this imply that the observed ratio of binary and single SMGs is reconcilable with the single SMGs being isolated disk galaxies, rather than end-stage major merger products as suggested by the comparison with local ULIRGs? In order to answer this, we need to quantify the impact of the SMG cool dust bias on the merger stage sampling function.

Veilleux et al. (2002) use the ratio of *IRAS* $25\,\mu m$ and $60\,\mu m$ flux as a proxy for dust temperature, and find that local ULIRGs with $f_{25}/f_{60} \geq 0.2$ ('warm ULIRGs') are only found among system with nuclear separations below $10\,\mathrm{kpc}$ (no trend is evident for smaller f_{25}/f_{60}, i.e. cooler systems; their Fig. 6). However, the percentage of systems with $f_{25}/f_{60} \geq 0.2$ is constant for all nuclear separations $\leq 10\,\mathrm{kpc}$. More importantly, only 14 out of 118 systems in their sample have $f_{25}/f_{60} \geq 0.2$ – i.e. less than 10% of ULIRGs are affected by this bias!

Turning to simulations, Figs. 3 & 4 of Narayanan et al. (2010b) and Fig. 1 of Narayanan et al. (2010a) show the evolution of the star formation rate, bolometric luminosity, and $S_{850\mu m}$ during simulated gas-rich major mergers. These show that after the peak in star formation rate during final coalescence, $S_{850\mu m}$ appears to drop off

more sharply than L_{bol}, most likely due to an increasing AGN contribution effecting an increase in the dust temperature. However, variations between different simulations make it quite difficult to quantify the time a merger has both high bolometric luminosity and low $S_{850\mu m}$ (D. Narayanan, priv. comm.).

Another way to tackle this question may be to compare the AGN luminosity contributions in local ULIRGs and SMGs, since from the above we would expect SMGs to be biased against the merger phases with strong AGN contributions. Veilleux et al. (2009) find local ULIRG luminosities to have $\approx 39\%$ AGN contribution; estimates for SMGs are more uncertain, but span a range of $8\text{-}35\%$ (Swinbank et al. 2004; Alexander et al. 2005, 2008; Lutz et al. 2005; Valiante et al. 2007; Pope et al. 2008a; Menéndez-Delmestre et al. 2009). This seems to confirm a significant bias – however, one must bear in mind the differences between high-z and local galaxies; their absolute AGN luminosities should be comparable (similar black hole masses), but the stellar luminosities are factors of several larger in high-z galaxies (due to the larger gas fractions, Tacconi et al. 2010; Daddi et al. 2010), and we therefore expect significantly smaller relative AGN contributions in high-z galaxies. Lower relative AGN contributions in SMGs compared to local ULIRGs are therefore not necessarily a result of a merger stage bias.

The cool dust bias of the $S_{850\mu m}$ criterion implies that there should be a population of hot dust, ultra-/hyperluminous high-z galaxies which are not detected as SMGs. And indeed, Casey et al. (2009a) through $70\,\mu m$ selection find a population of $z > 1$ galaxies with an average dust temperature of $52\,\mathrm{K}$, which are not detected at $850\,\mu m$. These systems have a mean far-infrared luminosity of $1.9 \times 10^{12} L_\odot$, only slightly lower than that of SMGs, and thus it is plausible that they consitute the hot dust extension of the SMG sample. Although uncertain, the number density of these galaxies is estimated to be approximately five times lower than that of SMGs – implying that, if indeed all these systems are major mergers, a high-z major merger may be undetectable as an SMG for approximately 1/6th of its lifetime; or $\approx 25\%$ of the time spent in the 'final coalescence' phase, if all these hot dust systems are in that stage (as one would expect, based on the arguments above). This is larger than, but consistent with, the $\sim 10\%$ of local ULIRGs showing a dust temperature - merger stage correlation.

It is clear that the merger stage sampling bias of $S_{850\mu m}$ vs. L_{IR} selection is difficult to quantify. We can only say with confidence that $S_{850\mu m}$ sampling of a major merger will likely result in a somewhat smaller fraction of coalesced systems, but it certainly will not exclude all of them. Local major mergers, selected via L_{IR}, consist to $\sim 64\%$ of systems with projected nuclear separations $\leq 2\,\mathrm{kpc}$ (Veilleux et al. 2002); our sample of 12 SMGs contains 7 sources which are either poorly resolved or clearly single galaxies (Table 3.2). If we conservatively assume that a major merger is undetectable as an SMG for 50% (30%) of the time spent in the 'final coalescence' stage, this implies we would expect the fraction of coalesced systems in the sample to decrease from $\sim 64\%$ to about 32% (45%). Thus *at most* 3 (1) out of the 7 compact/coalesced

sources in our sample could plausibly be isolated disk galaxies, rather than end-stage major mergers.

This corroborates the argument made by Tacconi et al. (2006), that the extreme surface densities of the compact SMGs can plausibly only be achieved during a major merger, and is further supported by our results of §3.4.2.2, where we show that our confirmation of the Hainline (2008) stellar mass estimates agrees with cosmological models in which SMGs result from major mergers.

These three independent arguments all point in one direction, namely that most, if not all, SMGs are major mergers.

3.5   Summary

Our investigation of twelve sub-arcsecond resolution interferometric CO line observations of SMGs lends strong support to a merger origin of a large majority of this class of galaxies.

- Five of our systems consist of two spatially distinct galaxies, and the remaining seven have either disturbed morphologies typical for advanced, pre-coalescence mergers or are compact, dense galaxies which plausibly are late-stage, coalesced mergers.

- All four systems consisting of two resolved galaxies in which the masses of the two separate components could be derived, have mass ratios of 1:3 or closer, within the errors. This demonstrates that they are *major* mergers.

- Our gas and dynamical mass estimates are physically consistent with the lower end of the range of stellar masses in the literature, those of Hainline (2008) adjusted to a Chabrier (2003) IMF. This supports hierarchical merger models, whereas it disfavours cold accretion flow models of SMG formation.

- The majority ($\sim$64%) of local infrared-luminosity-selected major mergers (ULIRGs) are coalesced or have nuclear separations $\leq 2\,\mathrm{kpc}$. This suggests that the large fraction of binary SMGs in our sample also implies a major merger origin for at least some of the compact/coalesced SMGs. Due to the uncertain difference in merger stage sampling of $L_{IR} \geq 10^{12} L_{\odot}$ and $S_{850\mu m} \geq 5\,\mathrm{mJy}$ selection, we can only estimate the corresponding ratio of binary/coalesced mergers expected in our SMG sample. However, even very conservative assumptions indicate that *at most* 3 of the 7 compact/coalesced sources in our sample could plausibly be isolated disk galaxies, rather than end-stage major mergers.

- SMG size measurements (Gaussian FWHM) from radio and CO fluxes are both consistent with diameters $\sim 5\,\mathrm{kpc}$. This is in agreement with work by Menéndez-Delmestre et al. (2009) and Hainline et al. (2009), who find that the star formation in SMGs is more extended than the kpc-scale central starburst in local

ULIRGs. This is consistent with what is expected from theoretical predictions and simulations of mergers with higher gas fractions (e.g. Mihos 1999; Narayanan et al. 2010b).

Theory and observations are only beginning to uncover how differently galaxy evolution proceeds at high redshifts, with the 'cold accretion flow' framework successfully addressing many of the shortcomings of the hierarchical merging scenario. Particularly in the lower-luminosity tail of the high-z galaxy population, future observational and theoretical efforts are clearly necessary to fully clarify the picture. However, the evidence presented here overwhelmingly supports a framework in which the *most* luminous $z \sim 2$ galaxies are powered by major mergers.

Chapter 4

NGC 6240: merger-induced star formation & gas dynamics

The work presented in this Chapter has been published as:

- "NGC 6240: merger-induced star formation & gas dynamics"
  Engel H., Davies R. I., Genzel R., Tacconi L. J., Hicks E. K. S., Sturm E., Naab T., Johansson P. H., Karl S. J., Max C. E., Medling A., van der Werf P. P., 2010, A&A, in press

4.1   Introduction

A rare opportunity to study a major merger in the transient phase between first encounter and final coalescence of two merging gas-rich spirals is afforded by NGC 6240, at a distance of 97 Mpc. With $L_{\mathrm{IR}} \sim 10^{11.8} L_\odot$ (Sanders & Mirabel 1996), it falls just short of being formally classified as a ULIRG. *HST* images show a large-scale morphology dominated by tidal arms characteristic for mergers past first peripassage (Gerssen et al. 2004). It is therefore more characteristic of the ULIRG class, to which it is commonly assigned; and our analysis shows its luminosity is likely to exceed the ULIRG threshold in the next 100–300 Myr. Two distinct nuclei, with a projected separation of $\sim 1.5''$ or 700 pc, are seen at infrared, optical, and radio wavelengths (Tecza et al. 2000; Max et al. 2005, 2007; Gerssen et al. 2004; Beswick et al. 2001). Each nucleus is host to an AGN, detected in hard X-rays (Komossa et al. 2003) and at 5 GHz (Gallimore & Beswick 2004). However, Lutz et al. (2003) and Armus et al. (2006) estimate that the AGN contribute less than half, and perhaps only 25%, of the luminosity. Tacconi et al. (1999) find the cold gas, as traced by CO(2-1) emission, to be concentrated between the two nuclei. The 1-0 S(1) H_2 line emission is one of the most powerful found in any galaxy to date (Joseph et al. 1984), probably excited in shocks (van der Werf et al. 1993; Sugai et al. 1997; Tecza et al. 2000; Lutz et al. 2003). The stellar kinematics (Tecza et al. 2000) display rotation centred on each of the two nuclei, and extraordinarily large stellar velocity dispersions ($\sim 350\,\mathrm{km\,s^{-1}}$) between them. Tecza et al. (2000) find evidence for a recent starburst in the central kpc (the region encompassing the two nuclei), and Pollack et al. (2007) resolve a few dozen clusters in the nuclear region that are also consistent with a recent starburst.

Here, we build on the qualitative picture put forward by Tecza et al. (2000) that NGC 6240 is a merger already past its first close encounter, where the luminosity arises from a very recent burst of star formation, and therefore in which the mass must be due to an older stellar population. We use new adaptive optics integral field K-band spectroscopy, interferometric mm CO(2-1) data, and merger star formation histories from numerical simulations, to perform a quantitative analysis of the mass, luminosity, age, and origin of the young and old stellar populations.

We first introduce the observations and data reduction processes for the data sets used in our analyses (§4.2). We briefly look at the molecular gas (§4.3), and then focus on a detailed analysis of the stellar dynamics (§4.4, §4.5, §4.6, §4.7), before discussing the merger geometry and stage, and the curious CO(2-1) morphology (§4.8). Bringing together these results, we then investigate the scale of the starburst (§4.9) and nature and origin of the nuclei (§4.10). We summarise our results in §4.11.

4.2 Observations and Data Processing

4.2.1 SINFONI Data

4.2.1.1 Observations and Reduction

Observations of NGC 6240 were performed on the night of 20 Aug 2007 at the Very Large Telescope (VLT) with SINFONI. For these observations the wavefront reference was provided by the Laser Guide Star Facility. We used the $R = 13.7$ mag star $40''$ off-axis from NGC 6240 to correct for tip-tilt motions. The instrument was rotated by $70°$ east of north in order to acquire this star. In order to cover both nuclei of NGC 6240 simultaneously, the $0.05'' \times 0.10''$ pixel scale was chosen, giving a $3.2'' \times 3.2''$ field of view. This pixel scale and the K-band grating provide a resolution of $6.6 \times 10^{-4} \, \mu m$, equivalent to $R \sim 3300$ or $90 \, km \, s^{-1}$ FWHM at $2.18 \, \mu m$.

The data set comprised 12 object frames interleaved with 4 sky frames. Each exposure was 300 seconds, yielding a total on-source integration time of 60 minutes. Data were reduced using the dedicated SPRED software package (Abuter et al. 2006), which provides similar processing to that for long-slit data but with the added ability to reconstruct the data cube by stacking the individual slitlets. In order to optimise the sky subtraction, we made use of the algorithm described in Davies (2007). The image was rotated to restore the standard orientation, with north along the Y-axis, and east along the X-axis. The pixel scale of the final reduced cube was $0.05'' \times 0.05''$.

Standard star frames were similarly reconstructed into cubes. Telluric correction and flux calibration were performed using HD 147550, a B9 V star with K=5.96 mag. Velocity Standards were also observed with the same spatial and spectral settings, in order to enable recovery of the kinematics. The 3 stars observed, and added to our library of similar stars, were HD 176617 (M3 III), HD 185318 (K5 III), and HD 168815 (K5 II). These stars were chosen because of their deep CO absorption longward of $2.3 \, \mu m$ which provides a good match to that of NGC 6240.

4.2.1.2 PSF Estimation

We estimate the PSF by comparing the SINFONI data to higher resolution K-band Keck AO imaging data (Pollack et al. 2007), which are both shown in Fig. 4.1. Although the spatial resolution of our integral field observations is not as good as that achieved by these Keck imaging data, we note that the two bright spots in the northern nucleus are clearly separated in our data, indicating that our resolution is better than the $0.2''$ achieved by HST/NICMOS (Fig. 3c in Gerssen et al. 2004).

As outlined by Davies (2008a) and employed by Mueller Sánchez et al. (2006), since an observed image is the convolution of an intrinsic image with a PSF, $I_{obs} = I_{intr} \otimes PSF$, we can use a higher resolution image with a known PSF to obtain a good estimate of the PSF in a lower resolution image in two steps. Having resampled the data to the same pixel scale, we first find the broadening function B whose
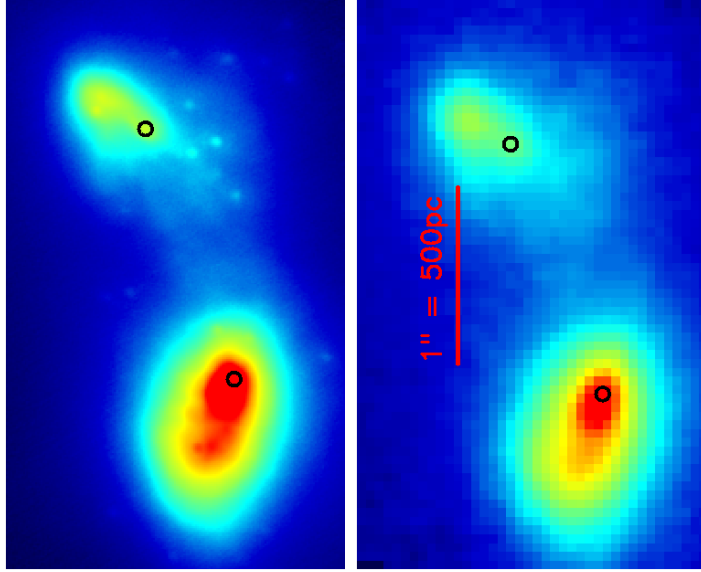
Figure 4.1: K-band adaptive optics images of NGC 6240 in square-root colour scale. Left: K-band flux density from NIRC2 on Keck II (pixel scale 0.01″, Pollack et al. 2007; Max et al. 2007). Right: 2.2 μm continuum from SINFONI on the VLT (pixel scale 0.05″), covering approximately the same field as left. In both panels, circles indicate AGN positions (see §4.5), north is up and east is left, and the red bar indicates 1″ (500 pc).

convolution with the high resolution image yields the best match to the low resolution image, $I_{low} = I_{high} \otimes B$. Since the underlying intrinsic image is the same for both I_{low} and I_{high}, we can then estimate the PSF of the low resolution image by convolving the broadening function B with the PSF of the high resolution image, $PSF_{low} = PSF_{high} \otimes B$. Since in this case B dominates the size and shape of our PSF, uncertainties in PSF_{high} have little impact on PSF_{low}. For the analyses carried out here, this procedure gives a sufficiently accurate definition for the PSF. We find the PSF to be well matched by an asymmetric Gaussian with major axis oriented $-20°$ east of north. The resolution is $0.097″ \times 0.162″$ FWHM, corresponding to 50×80 pc at the distance of NGC 6240. The asymmetry is to be expected since the resolution of the original data is pixel limited, being sampled at $0.05″ \times 0.10″$. The reason we are able to do better than the formal Nyquist limit is because the SINFONI data are resampled to $0.05″ \times 0.05″$ and many dithered exposures are combined using sub-pixel shifts to align them.

4.2.1.3   Spatial binning

Because of the limited signal-to-noise in our data, we have binned them spatially using an optimal Voronoi tessellation (Cappellari et al. 2003). This algorithm bins pixels together into groups by accreting new pixels to each group according to how close

they are to the centroid of the current group. The resulting groups then provide a set of positions (centroids) and mean fluxes which are used as the initial 'generators'. A further algorithm optimises the generator configuration based on a centroidal Voronoi tessellation. The final set of generators are the positions of the flux-weighted centroids of each binned group, and have the property that each pixel in the original image is assigned to the group corresponding to the nearest generator. This procedure only affects spaxels below a specified signal-to-noise threshold, and hence does not impact the spatial resolution of high signal-to-noise regions. The signal-to-noise cutoff was 20, chosen such that the regions with the highest signal-to-noise remained fully sampled, but lower signal-to-noise regions were binned. This avoided compromising the spatial resolution around the center of each nucleus, while enabling us to extend the region in which analyses can be performed. The effect of this can be seen in the resulting stellar kinematics maps, where the colours in the outer regions appear in blocks rather than individual pixels. The binning scheme that this routine provided was applied to each spectral plane in the cube, and the kinematics were extracted from each bin as described below.

4.2.1.4 Extracting Stellar Kinematics

The observed wavelength regime contains the stellar CO absorption bandheads longward of $2.29\,\mu$m, whose sharp blue edges are very sensitive to stellar motions. We utilise CO 2-0 and CO 3-1 to derive 2D maps of the stellar velocity and dispersion. The spectra were prepared by normalising them with respect to a linear fit to the line-free continuum. The continuum level was then set to zero by subtracting unity. A template spectrum, that of the M3 III star HD 176617, was prepared in the same way. Although both Sugai et al. (1997) and Tecza et al. (2000) used K Ib stars, they also both noted that M III stars provided almost equally good fits to the K-band features (see Fig. 5 in Tecza et al. 2000). We therefore do not expect template mismatch to be a problem but, as explained below, our method furthermore minimises the impact of any discrepancy. Silge & Gebhardt (2003) showed that the dispersion measured depends on the equivalent width of the template; this can be understood since the depth of the extinction feature relative to the continuum level (which may contain non-stellar emission) places a strong constraint on the fitting parameters. But it is the spectral width, not the equivalent width (i.e. depth), of the absorption feature that is important for deriving the dispersion. In our fitting method we resolve the problem of the feature's depth by setting the continuum level to zero. Therefore matching the relative depth of the absorption features, and hence the choice of template, is no longer critical.

In order to demonstrate this quantitatively, we have made use of the stellar template library of Winge et al. (2009). We created a large series of mock observations by broadening a K5 Ib template by various amounts in the range 150–300 km s^{-1}, and adding noise. We then extracted the dispersion using various mis-matched stellar

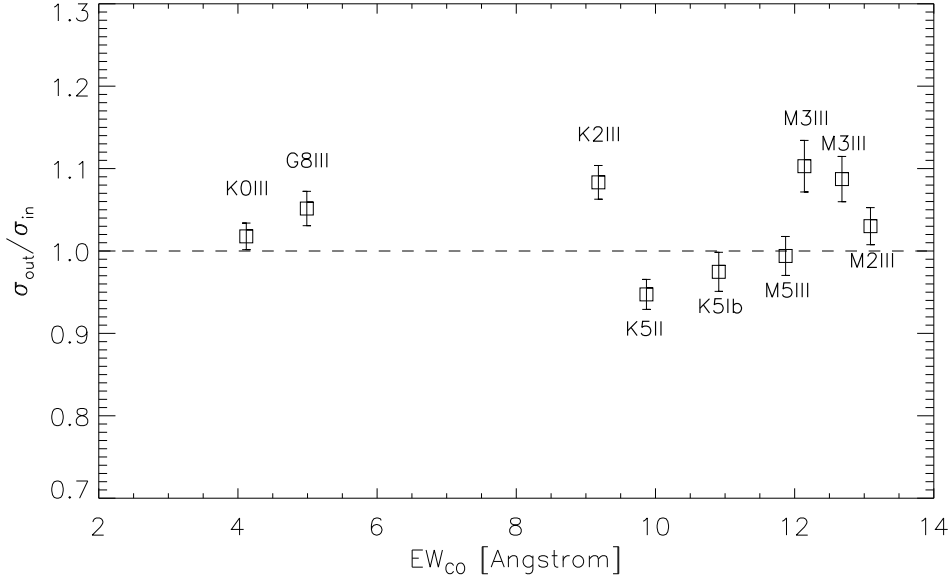**Figure 4.2:** Ratio between the measured dispersion σ_{out} and the input dispersion σ_{in} for a range of different stellar templates used to extract kinematics from a K 5Ib template. For each combination, a variety of dispersions in the range 150–300 km s^{-1} were used and noise was added to achieve a S/N$\sim$35. Variations in measured stellar kinematics using templates with a large range of EW$_{CO}$ and stellar types are around a few percent, showing that with our method a mismatched stellar template has little effect.

templates spanning a wide range of EW$_{CO}$ (equivalent width of the CO absorption feature) and spectral type. As can be seen in Fig. 4.2, our method recovers the input dispersion with a typical error of only a few percent, regardless of the template's spectral type. This shows that our method of extracting the stellar kinematics works reliably even if the template used is not a perfect fit. We emphasize that, in contrast to Sugai et al. (1997) and Tecza et al. (2000), we do not use the quality of the template fit to draw conclusions about the prevalent stellar population. This requires caution, and we discuss the pitfalls associated with doing so in §4.9. As such, because we use this star only for extracting kinematics, our choice of template can be fully justified by the good fits to the bandheads in the galaxy spectra in Fig. 4.3.

For the spectrum at each spatial pixel ('spaxel' hereafter) in the data cube, we convolve the template with a Gaussian, adjusting the properties of the Gaussian to minimise the difference between the convolution product and the galaxy spectrum. Deviant pixels are rejected from the fit. The spectral regions covering the steep edges of the bandhead at all expected stellar velocities are given five-fold weight
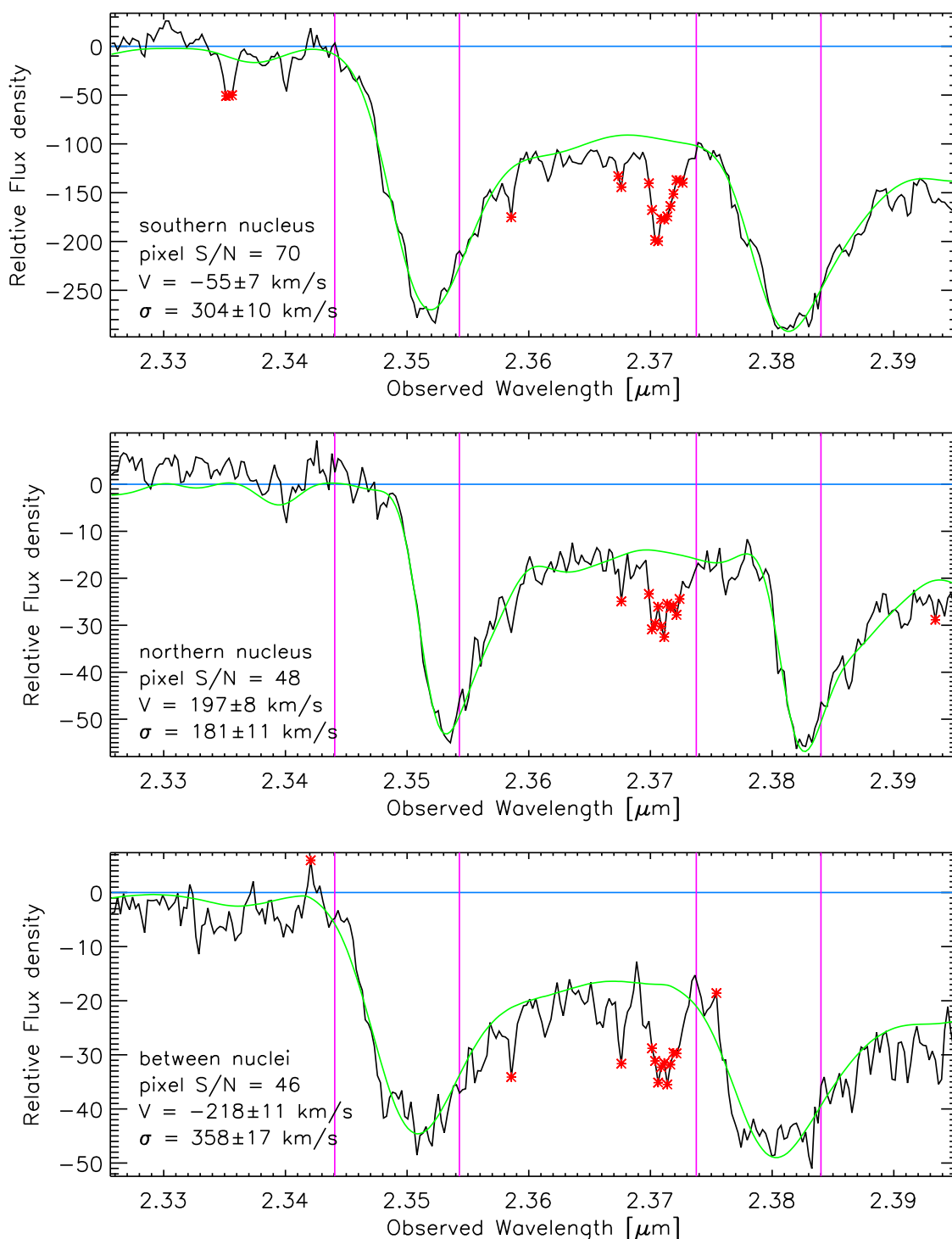
Figure 4.3: Spectra (black lines) and template fits (green lines) to the CO 2-0 and CO 3-1 stellar absorption features. These are for individual bins in the southern nucleus (top), the northern nucleus (middle) and in the region of high dispersion between them (bottom). The blue line indicates the continuum (i.e. zero) level; red asterisks denote pixels rejected during the fit; the pairs of magenta lines enclose regions around the bandheads for which the weighting is enhanced during the fit. These plots demonstrate the quality of the fit using our single M3 III template.

(Figure 4.3), in order to focus the fit on the kinematics rather than details in the spectrum. To ensure consistency in our analyses, the spectral ranges applied to compute EW_{CO} were taken from Förster Schreiber (2000), since these ranges are also used by the stellar synthesis code STARS which we use later. A high signal-to-noise ($\gtrsim 50$, Cappellari et al. 2009a) is required in order to measure deviations in the line of sight velocity distribution from a simple Gaussian. Without binning beyond a useful spatial resolution, the signal-to-noise in most of our spectra is not sufficient to include the Gauss-Hermite terms h_3 and h_4 in the fit. We therefore limited the kinematic extraction to V and σ. The noise in the kinematics was determined using Monte Carlo techniques: 100 realisations of the data were generated, a number that ensures a fractional uncertainty in the noise of less than 10%, by perturbing the flux at each pixel according to its RMS. These were fit using the same procedure as above. Although the RMS at each pixel can be derived when combining the data cubes, calculating the noise in bins is extremely difficult due to the correlations between neighbouring pixels. This is discussed in detail by Förster-Schreiber et al. (2009). Instead, we have derived the noise as the RMS of the difference between a spectrum and the convolved template (excluding rejected pixels). This may slightly over-estimate the noise, but will then yield conservative error estimates on the kinematic parameters. The resulting final maps of stellar velocity, dispersion, and EW_{CO} are displayed in Fig. 4.4.

4.2.2   Plateau de Bure Interferometer Data

We have mapped the $^{12}CO(J = 2\text{-}1)$ line in NGC 6240 with the IRAM millimetre interferometer, which is located at an altitude of 2550 m on the Plateau de Bure, France (Guilloteau et al. 1992). The data were obtained in May 2007. The array consisted of six 15 m antennae positioned in two configurations providing a large number of baselines ranging from 32 to 760 m. We observed NGC 6240 for 5 hrs in A configuration, which provides a nominal spatial resolution of $0.35''$ at 230 GHz. However, the low (+2deg) declination of NGC 6240 limited the resolution in an approximately north-south direction. A spectral resolution of 2.5 MHz, corresponding to $3.3\,\mathrm{km\,s^{-1}}$ for the CO(2-1) line, was provided by 8 correlator spectrometers covering the total receiver bandwidth of 1000 MHz ($1300\,\mathrm{km\,s^{-1}}$). All the data were first calibrated using the IRAM CLIC software. We then made uniformly weighted channel maps for the CO(2-1) data. We CLEANed all the maps using software available as part of the GILDAS package. To increase the sensitivity, maps were made with a velocity resolution of $26.6\,\mathrm{km\,s^{-1}}$. The CLEANed maps were reconvolved with a $0.69''\times0.26''$ FWHM Gaussian beam. The rms noise after CLEANing is $1.4\,\mathrm{mJy\,beam^{-1}}$. Fig. 4.5 shows the velocity-integrated CO(2-1) emission (black circles denoting approximate AGN locations), velocity moment map, and the dispersion (obtained from fitting Gaussians to the line shape). The AGN positions were estimated using the positions given by Gallimore & Beswick (2004); due to the astrometric uncertainties, these are
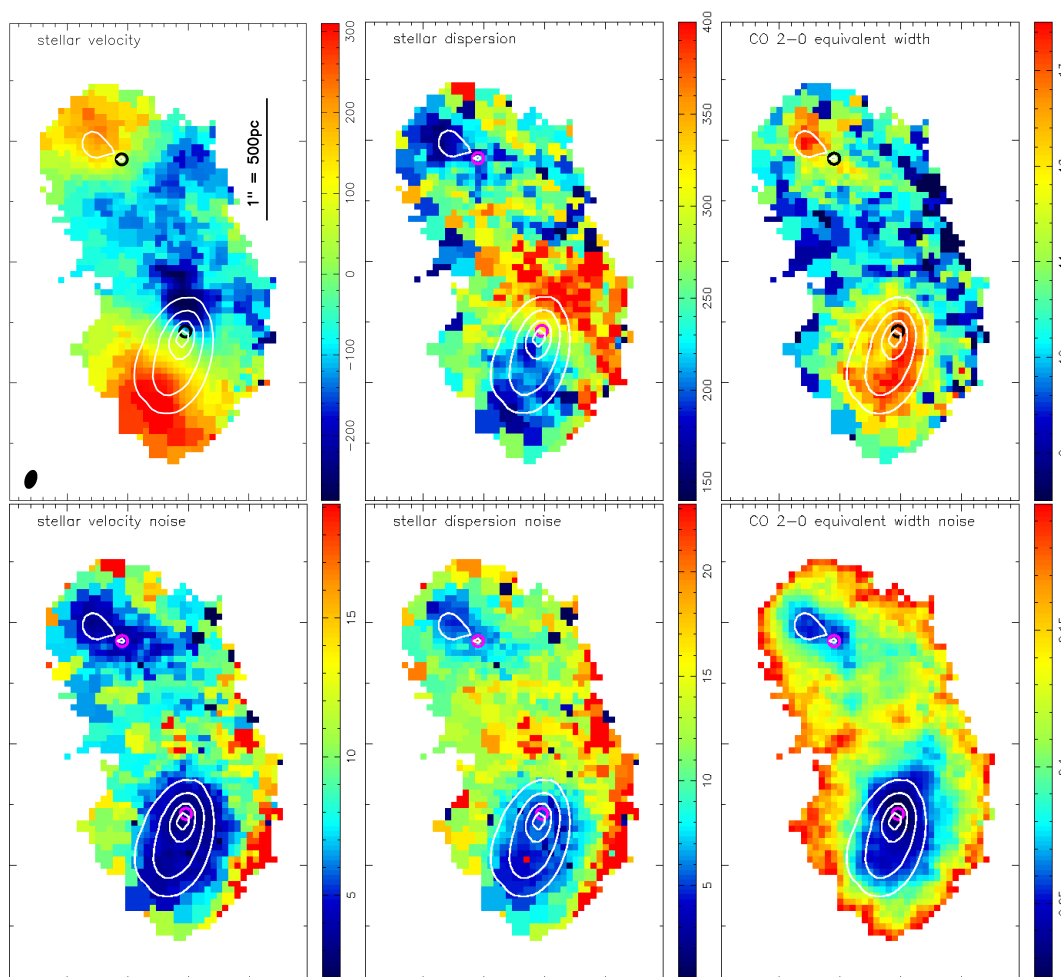
Figure 4.4: Stellar velocity and corresponding noise map (top and bottom left, both in $\mathrm{km\,s^{-1}}$ with respect to systemic), dispersion and corresponding noise map (middle, both in $\mathrm{km\,s^{-1}}$), and EW_{CO} and its noise map (right, both in Å). Contours trace the continuum as in Fig. 4.1. Black/magenta circles mark the AGN positions (see §4.5). The bar indicates $1''$ (images are $2.45'' \times 3.95''$), the PSF size is shown in the lower left corner of panel 1. North is up and east is to the left.
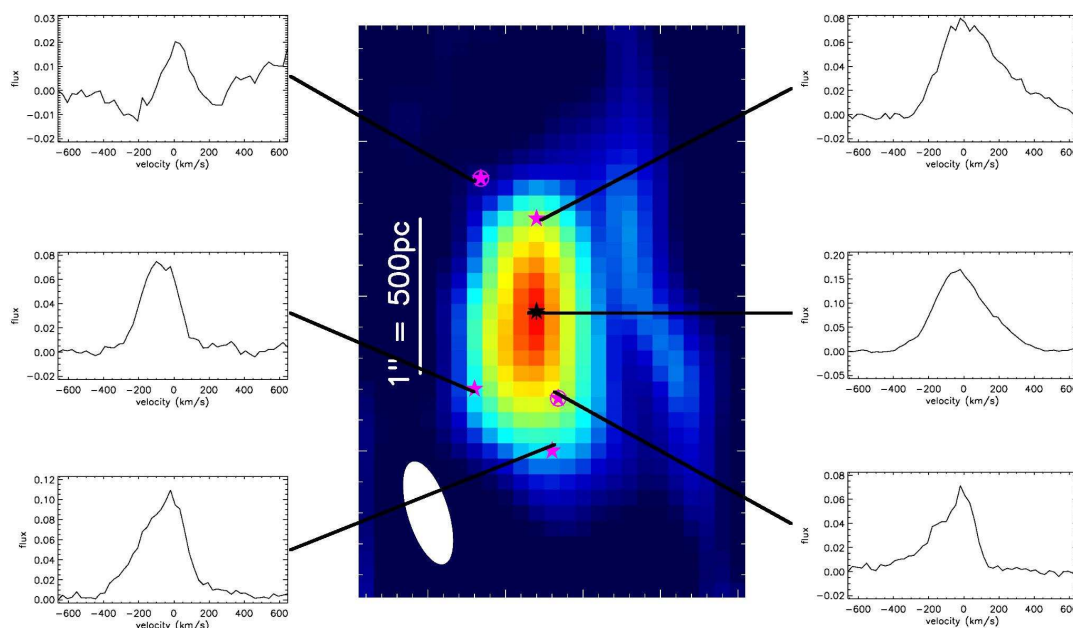
Figure 4.5: Map of CO(2-1) flux with spectral line profiles shown for selected spaxels. Circles denote AGN positions, stars denote positions where spectra were extracted. The beam size is displayed in lower left. The bar denotes $1''$, and north is up and east is to the left.

only accurate to within 1-2 pixels (0.7-0.14$''$).

4.3   Molecular Gas Emission

4.3.1   H$_2$ 1-0S(1)

NGC 6240 has the strongest H$_2$ line emission found in any galaxy to date (Joseph et al. 1984). Several authors (van der Werf et al. 1993; Sugai et al. 1997; Tecza et al. 2000) identify shocks as the excitation mechanism, and Ohyama et al. (2003) use the relative intensity of H$_2$ and CO(2-1) emission to conjecture that the shocks occur due to a superwind outflowing from the southern nucleus colliding with the molecular gas concentration. Our new SINFONI data provide the most detailed spatial and spectral view currently available. As can be seen in Fig. 4.6, the line profiles are highly complex, with clear evidence of multiple components. This, and the dispersion map (Fig. 4.7), support the picture of highly disturbed, turbulent gas. The emission morphology is uncorrelated with the stellar emission distribution, but roughly consistent with the cold gas emission (as traced by the CO(2-1) emission,

§4.3.2). The velocity moment map (Fig. 4.7) shows a global velocity gradient, again broadly consistent with what is seen in CO(2-1).

4.3.2 CO(2-1)

Fig. 4.5 shows the velocity-integrated CO(2-1) emission, with line shapes at selected positions. With a factor of two improvement in resolution along the E-W direction, our data re-affirm the findings of Tacconi et al. (1999). However, our resolution in the crucial N-S direction is limited by the declination of the source. As a result we are not able to draw more detailed conclusions about the CO(2-1).

The CO emission is concentrated in between the two nuclei, and the CO(2-1) velocity map, red and blue wings, and P-V-diagram all display signs of a velocity gradient. This is consistent with the findings of Tacconi et al. (1999), who conclude that the molecular gas likely is concentrated in a self-gravitating rotationally supported, but highly turbulent disk in the internuclear region. However, such a central gas concentration is not expected from merger simulations, which generally predict the gas to remain largely bound to the progenitors until the nuclei coalesce. We discuss this issue further in §4.8.

The total flux is about 40% less than that measured by Tacconi et al. (1999), indicating that our smaller beam has resolved out some emission on intermediate to large scales. We have not made a correction for this, since we are interested primarily in the small scale emission of the nuclei themselves, where the effect is likely to be negligible. To estimate the gas mass associated with the nuclei, we have measured velocity-integrated line fluxes within the same radii as those used in our dynamical mass modelling (§4.7), which were chosen to cover the extent of observed stellar rotation in the nuclei. In the northern nucleus we find $S_{CO}\Delta V = 37\,\mathrm{Jy\,km\,s^{-1}}$ out to a radius of 250 pc; in the southern nucleus we find $S_{CO}\Delta V = 178\,\mathrm{Jy\,km\,s^{-1}}$ out to a radius of 320 pc.

We estimate the gas mass by converting to line luminosity $L'_{CO} = 3.25\times10^7 S_{CO}\Delta V \nu_{obs}^{-2} D_L^2 (1+z)^{-3}$ (with $D_L = 97\,\mathrm{Mpc}$, $z = 0.0243$, $\nu_{obs,CO_{2-1}} = 225.1\,\mathrm{GHz}$), and using the relations $L(CO_{2-1})/L(CO_{1-0}) = 0.8$ (Casoli et al. 1992) and $M_{H_2}/L_{CO_{1-0}} \sim 1\,\mathrm{M_\odot}/(\mathrm{K\,km\,s^{-1}\,pc^2})$, as Downes & Solomon (1998) find for ULIRGs. This yields $\sim 0.2 \times 10^9\,\mathrm{M_\odot}$ and $\sim 1.1 \times 10^9\,\mathrm{M_\odot}$ for northern and southern nuclei, respectively. Similarly, for an aperture of $1''$ diameter centred on the CO emission peak, we derive a gas mass of $\sim3.1\times10^9\,\mathrm{M_\odot}$. We caution that the nuclear masses are very uncertain and should be treated only as order-of-magnitude estimates. The reason is that a significant fraction of the gas within the apertures may not be physically co-located with the nuclei, which would imply the masses are upper limits. On the other hand, the CO abundance around the nuclei is very likely to have been significantly reduced by X-ray irradiation from the AGN (see §4.8). In this case, the masses would be underestimates.

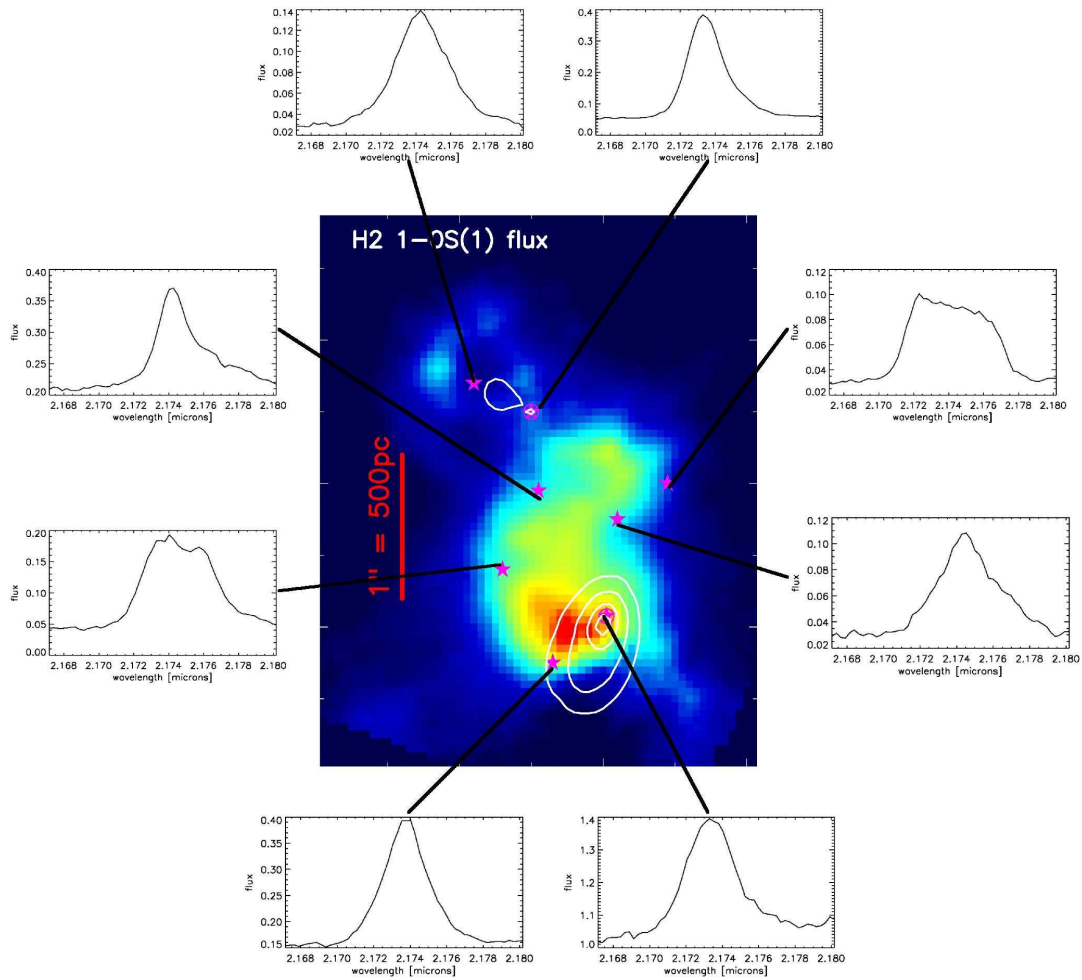**Figure 4.6:** Map of H_2 1-0 S(1) emission, with line shapes at selected spaxels. Circles mark AGN positions, stars denote positions where spectra were extracted, white contours represent continuum emission. The bar denotes $1''$, and north is up and east is to the left.
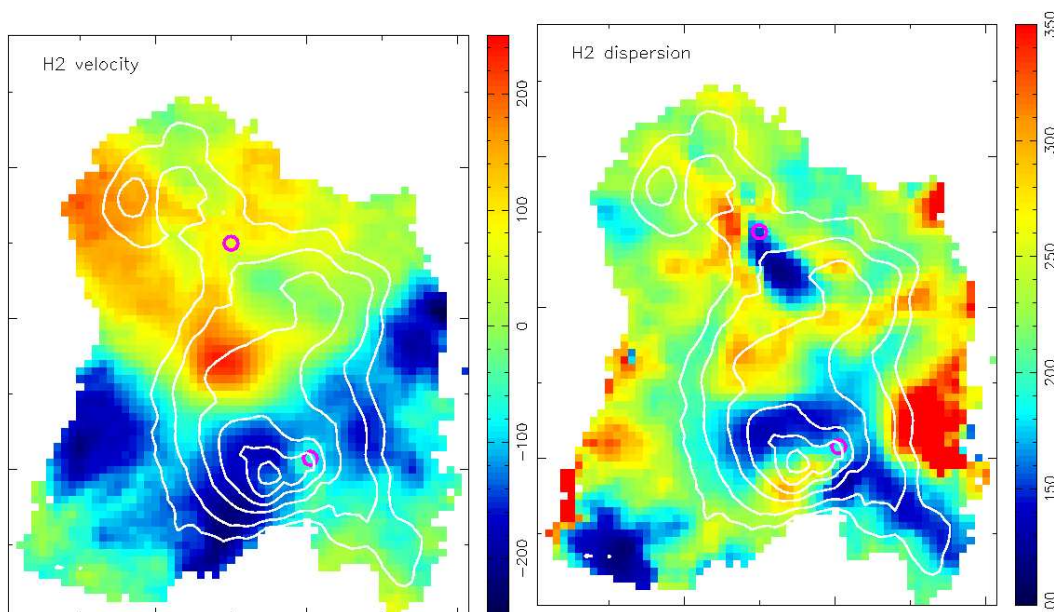
Figure 4.7: Velocity moment (left) and dispersion (right) maps of H$_2$. Magenta circles mark AGN positions, white contours represent H$_2$ 1-0 S(1) line emission.

4.4 Extinction and Luminosity of the Nuclei

Like most ULIRGs, NGC 6240 contains significant amounts of dust (Tecza et al. 2000), and hence correcting any flux measurement for extinction is paramount to ensure accuracy in the analyses described below. It is valuable to consider the extinction derived from mid-infrared data to assess whether the near infrared might be affected by saturation. However, this appears to be uncertain – primarily because no H$_{II}$ lines were detected either by ISO (Lutz et al. 2003) or Spitzer (Armus et al. 2006). Based on silicate absorption at 9.7 μm, Armus et al. (2006) find an extinction of $A_V \sim 95$ mag to the coronal line region. The more moderate estimates presented by Lutz et al. (2003) are for a global extinction, and correspond to a dust screen $A_V \sim 15$–20 mag. This estimate is comparable to derivations at radio ($N_H \sim (1.5$–2)$\times 10^{22}$ cm^{-2}, Beswick et al. 2001) and X-ray ($N_H \sim 10^{22}$ cm^{-2}, Komossa et al. 2003) wavelengths. This is important, because it implies a modest typical K-band screen extinction of only $A_K \sim 1$–2 mag. Thus our data should be sensitive to the majority of the emission. However, we note that the X-ray spectrum at energies above 10 keV indicates that at least one of the AGN themselves may be obscured by a column $> 10^{24}$ cm^{-2} (Vignati et al. 1999; Ikebe et al. 2000; Netzer et al. 2005). Differences between these various column density measurements are to be expected since they sample different spatial scales and sight lines; for example, the X-ray data specifically measure gas column density along the line of sight to the AGN rather than the extended cold dusty
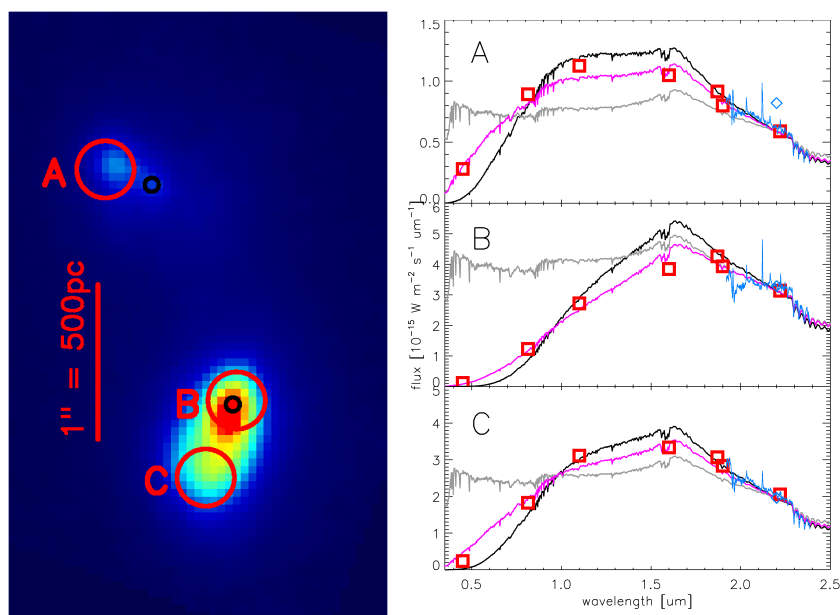
Figure 4.8: Comparison of different extinction models: We measured HST photometric data points (red squares) in $0.2''$ radius apertures; positions for the three examples shown here are indicated in the left panel. To these we fitted a synthetic STARS spectrum which was reddened using different reddening prescriptions: screen extinction (black), mixed extinction (grey), and the Calzetti et al. (2000) reddening law (magenta). We also overplot our SINFONI spectrum (blue), scaled to the HST $2.22mu$m data point (absolute SINFONI flux at $2.2mu$m shown as blue diamond). As can be seen, the Calzetti et al. (2000) reddening law provides the best fit to the data.

medium.

When correcting for the obscuring effect of dust, one needs to make assumptions about its location and distribution. The two most commonly used models assume either a uniform dust screen between the observer and the stars, leading to a reduction in observed flux according to $F_{obs}/F_{em} = e^{-\tau}$. Or the stars and dust are assumed to be spatially coincident and uniformly mixed ('mixed model'), in this case the observed flux decreases as $F_{obs}/F_{em} = (1 - e^{-\tau})/\tau$. Another alternative is the Calzetti et al. (2000) reddening law, derived empirically from observations of starburst galaxies. Its wavelength dependence reflects both the dust grain properties and the distribution of the dust with respect to the stars in these galaxies. The effect of this reddening law is remarkably similar to a combination of mixed and screen extinction, with – for the degree of extinction seen in NGC 6240 – the mixed component dominating in the infrared, and the screen component increasingly important at optical wavelengths. In order to investigate which extinction model best captures the characteristics of the dust distribution of NGC 6240, we obtained a number of archival HST imaging data, spanning wavelengths from 0.45μm to 2.22μm, and extracted photometric data points from a number of $0.2''$ radius apertures across our field of view. And we calculated a synthetic stellar spectrum using the stellar synthesis code STARS (Sternberg 1998; Sternberg et al. 2003; Förster Schreiber et al. 2003; Davies et al. 2003, 2005, 2006, 2007), assuming a star formation rate typical for a merger ('Antennae'-simulation, §4.8). We then fitted this spectrum to the HST data points and our SINFONI K-band spectra, using the screen and mixed extinction models, and the Calzetti et al. (2000) reddening law. As can be seen in Fig. 4.8, the Calzetti et al. (2000) reddening law best reproduces the observations; the mixed model saturates at optical wavelengths and cannot redden the spectra sufficiently, and the screen model is reddening the spectra too much at shorter wavelengths. We also test whether our choice of star formation history has an influence on this result, by conducting the same test with synthesised spectra for a 20 Myr old instantaneous starburst and 1 Gyr of continuous star formation. Both also indicate the Calzetti et al. (2000) reddening law to be appropriate.

We can then find F_{obs}/F_{em} for each spatial pixel by adjusting the reddening for a set of stellar template spectra according to Eqn. 2 in Calzetti et al. (2000), until the best-fit of a linear combination of templates to the measured line-free continuum is achieved. Fig. 4.9 shows the resulting map of A_K. The choice of stellar templates does not affect the result, since the K-band samples the Rayleigh-Jeans tail of the blackbody curve and hence to a good approximation all stars, and late-type stars in particular, have the same spectral slope.

One might ask whether a component of non-stellar emission from hot dust might be present, in our field of view in general and close to the AGN in particular. This is an important question, since it would have an influence on the stellar masses and mass-to-light ratios we calculate later on. That the K-band continuum may even be dominated by hot dust has been proposed by Armus et al. (2006). However,

	North observed	North dereddened	South observed	South dereddened
Apertures, Tecza et al. (2000)	$2.2 \times 10^8 L_\odot$	$2.3 \times 10^8 L_\odot$	$5.8 \times 10^8 L_\odot$	$6.8 \times 10^8 L_\odot$
Apertures, this work	$5.6 \times 10^8 L_\odot$	$9.8 \times 10^8 L_\odot$	$1.5 \times 10^9 L_\odot$	$4.0 \times 10^9 L_\odot$
Integrated profiles, this work		$1.1 \times 10^9 L_\odot$		$5.9 \times 10^9 L_\odot$
Apertures, NICMOS	$5.3 \times 10^8 L_\odot$		$1.7 \times 10^9 L_\odot$	

Table 4.1: Integrated Luminosities of the Nuclei. Apertures are all diameter $1''$, the profiles are integrated out to a radius of $0.5''$.

this conclusion was based on a fit to the near-IR spectral energy distribution that was constrained primarily as the residual in the blue side of a much more dominant cooler component, and is therefore rather uncertain. Instead, the good match of reddened synthetic stellar spectra to the photometry (Fig. 4.8) indicates that non-stellar emission is unlikely to contribute significantly. More importantly, emission from hot dust would dilute the stellar CO absorption features. Since we measure $EW_{CO} \sim 12\text{-}13\,\text{Å}$ (Fig. 4.4), and the theoretically possible (achievable only through a 10 Myr old instantaneous starburst) maximum is $\sim 17\,\text{Å}$, this puts a firm theoretical upper limit of $<30\%$ on any non-stellar contribution, and realistically makes anything larger than a few percent unlikely. And since we do not see a localised dip in EW_{CO} around the AGN positions, we conclude that any hot dust emission associated with the AGN is completely obscured at near-IR wavelengths.

Table 4.1 lists the observed and dereddened luminosities measured within apertures of diameter $1''$ centered on the northern and southern nuclei, from Tecza et al. (2000), this work, and from archival NICMOS data; and also those obtained by integrating the luminosity profiles out to 250 pc. We included the NICMOS data to obtain a third independent measurement, since our measurements of the observed luminosities and those of Tecza et al. (2000) differ by a factor of two. We find the NICMOS data agree with our measurements to within 10%. As can be seen, for Tecza et al. (2000), the dereddening only alters the measured luminosities by $\sim 10\%$, whereas for us, the difference is circa a factor of two. This difference is most likely due to the fact that we applied a spatially dependent, rather than single-valued, correction.

4.5   Kinematic Centres and Black Hole Locations

In this section, we attempt to confirm the hypothesis that the black hole locations do identify the centres of the progenitors, by independently determining the locations of the kinematic centres from the stellar velocity field. As we outline below, for a number of reasons locating the kinematic centres of the observed stellar rotation reliably and accurately is extremely difficult to do. Nevertheless, within the uncertainties, we find that the BH positions of Max et al. (2007) are consistent with the kinematic centres.
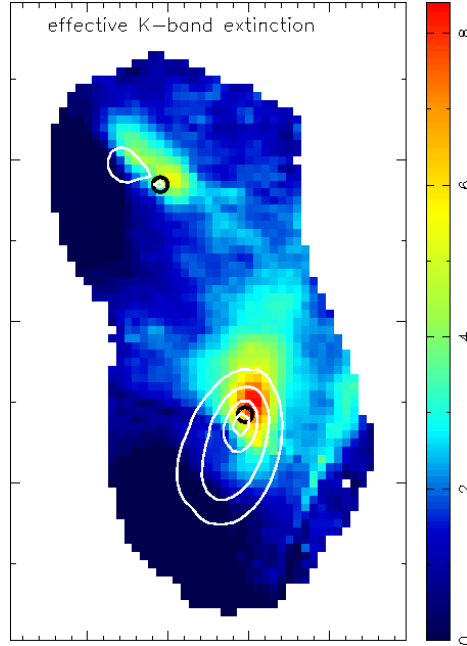
Figure 4.9: Effective K-band extinction A_K. As for Fig. 4.1, contours trace the continuum and black circles denote the AGN positions. Each $0.05''$ pixel length corresponds to $25\,\mathrm{pc}$ at the distance of NGC 6240.

Max et al. (2007) determined the positions of the two AGN in NGC 6240 by combining images taken in the near-infrared, radio, and X-ray regimes. Postulating that the southern sub-peak of the northern nucleus as seen in the K-band ('N1' in the notation of Gerssen et al. 2004) is coincident with the position of the northern black hole, they superpose radio data to infer that the southern AGN is located to the north-west of the $2.2\,\mu\mathrm{m}$ peak of the southern nucleus. The offset is explained in terms of dust obscuration, which is supported by their $3.6\,\mu\mathrm{m}$ images showing the southern continuum peak to be coincident with the posited black hole location. Our data also support the existence of higher obscuration at this location: Fig. 4.9 shows that the region suffering the greatest extinction overlaps with, and extends to the northwest of, the southern nucleus. We identify the AGN positions of Max et al. (2007) to an accuracy of better than ± 1 pixel ($0.05''$) on our data using the $2.12\,\mu\mathrm{m}$ continuum features as reference points (as shown in Fig. 4.1), and the angular separation of the VLBA radio sources ($1.511\pm 0.003''$, Max et al. 2007 and references therein). The uncertainties on the BH positions as identified on the Max et al. (2007) data are smaller than the uncertainty introduced by this translation onto our data.

We use kinemetry (Krajnovic et al. 2006) to parametrize the stellar velocity field which, as Fig. 4.4 shows, clearly exhibits ordered rotation around each of the two nuclei separately. In many cases, the centre of a galaxy and its axis ratio (or inclination)

and position angle (PA) can be extracted straightforwardly from the isophotes. This is not possible for NGC 6240 because the K-band isophotes are strongly asymmetric with respect to the black hole locations found by Max et al. (2007). Hence we must use our analysis of the velocity field to also fix these parameters simultaneously.

Kinemetry decomposes a velocity map $K(a, \psi)$ into a series of elliptical rings that can be expressed as the sum of a finite number of terms:

$$K(a, \psi) = A_0(a) + \sum_{n=1}^{N} A_n(a) \sin(n\psi) + B_n(a) \cos(n\psi).$$

By minimizing particular terms, one can in principle find the centre, position angle, and axis ratio of the velocity field. Under the assumption that the velocity field is due to an axisymmetric thin disk, these correspond directly to the equivalent parameters for the galaxy (although one should bear in mind that, for example, with non-circular orbits the kinematic and isophotal major axes may not coincide; and for a geometrically thick system the axis ratio may not represent the inclination).

The correct choice of kinematic centre minimises A_2 and B_2 (which are also weakly dependent on ellipticity and PA) and to a lesser degree A_1, A_3, and B_3 (see Krajnovic et al. 2006 for a more intuitive description of these parameters). The correct PA yields minimal values of A_1, A_3, and B_3; correct ellipticity minimises B_3. For a range of different ellipticities and PA, we place the kinematic centre at each pixel within a grid of 11×11 pixel centered on the AGN location and calculate the corresponding sum of A_2 and B_2. This results in a set of 2D maps of $A_2 + B_2$ for each combination of PA and ellipticity. The position of the minimum of each map then yields the best-fitting kinematic centre for that specific combination of PA and ellipticity. If the best-fit to the kinematic centre is the same for different values of ellipticity and PA (i.e. a unique best estimate for the kinematic centre exists), we then proceed to determine A_1 and A_3 at this kinematic centre for a range of different position angles, taking as the best estimate of the PA that value which results in $A_1 + A_3$ being minimal. Finally, the ellipticity is found by analogously minimising the B_3 coefficient.

With this method we are able to find a unique solution for all three parameters for the southern nucleus. But it fails for the northern nucleus where the best estimates for kinematic centre and position angle are interdependent: the minima for $A_2 + B_2$ (determining the kinematic centre) lie on an arc with the exact position of the kinematic centre dependent on the choice of position angle. The only way out of this impasse is to make additional assumptions, and so we arrive at a 'best-fit' by assuming the velocity field to have the same PA as the major axis of the continuum emission. We note that the PA of the continuum emission is independent of the extinction correction, because the extinction and continuum maps have the same PA. Figures 4.10 and 4.11 show the observed velocity field, the model, and the residuals for 2 cases in each nucleus: when the best-fitting centre derived from the kinemetry is used, and when the centre is fixed at the location of the black hole.

In the northern nucleus, the location of the derived kinematic centre is reasonably consistent with the black hole location, differing by only 0.12″. Since the average residuals per pixel are $33.5\,\mathrm{km\,s^{-1}}$ and $35.3\,\mathrm{km\,s^{-1}}$ for these two cases respectively, they can be considered statistically indistinguishable. We conclude that in the northern nucleus, we can confirm that the black hole is located at the kinematic centre of the stellar rotation.

For the southern nucleus, the difference is more significant. The separation between the best-fitting centre and the AGN location is 0.22″. The mean residuals are $28.2\,\mathrm{km\,s^{-1}}$ (best-fit) and $45.9\,\mathrm{km\,s^{-1}}$ (AGN position). This can be understood with reference to the dispersion map in Fig. 4.4 and the extinction map in Fig. 4.9. The region to the northwest of the AGN in the southern nucleus exhibits both anomalously high dispersion and extinction – features that are to be expected in a merger system. It is therefore not clear whether the velocity field in this region is really tracing the rotation of the progenitor, or something more complex. Inspection of the residuals in Fig. 4.11 suggests the latter, an issue that we discuss in more detail in §4.6. Our conclusion for the southern nucleus is that the centre we derive from the velocity field is biased by perturbed kinematics on the northern side of the nucleus.

In both nuclei, for further analyses we therefore adopt the black hole locations of Max et al. (2007) as identifying the kinematic centres of the nuclei, and make use of the rotation curves, dispersion, and luminosity profiles centered at these positions. We derive axis ratios of 0.70 ± 0.02 and 0.65 ± 0.02 and PAs of $229° \pm 2°$ and $329° \pm 2°$ (measured east of north, PA pointing from receding to approaching velocities) for the northern and southern nuclei, respectively. We interpret the axis ratios in terms of an inclination for a flat system, noting that this may be an overestimate since the nuclei are likely to be thick. The impact is that we may also overestimate the intrinsic velocity.

4.6   Stellar Kinematics between the Nuclei

NGC 6240 is known to exhibit an exceptionally large stellar velocity dispersion between the nuclei (Lester & Gaffney 1994; Doyon et al. 1994; Tecza et al. 2000). In Fig. 4.4 we present a detailed 2D dispersion map which shows that the region with the highest ($>300\,\mathrm{km\,s^{-1}}$) dispersion is fairly localised, and lies across the northern side of the southern nucleus. The localised nature of this region, together with poor signal-to-noise, most likely explain why Genzel et al. (2001) and Dasyra et al. (2006b) cite a significantly lower maximal dispersion, as it can easily be missed by slit measurements.

This high dispersion cannot be associated with the established stellar population in the southern nucleus because the high velocity ($\sim500\,\mathrm{km\,s^{-1}}$ at $500\,\mathrm{pc}$) implies a dynamical timescale of $t_{dyn} \sim 5\,\mathrm{Myr}$. Any asymmetry in the dispersion of a stellar population orbiting the southern nucleus would be dispersed within this timescale. An alternative explanation is that this represents a region where emission from stars

Figure 4.10: Northern Nucleus: Comparison of kinemetry models for two different PAs and kinematic centres. It should be noted that the rotation curves do not differ significantly for the two different positions of the kinematic centre. Black circles indicate black hole positions; black stars represent the kinematic centre; the dashed white line traces the major axis of rotation. Left to right: velocity map, model, and residuals. First row: best-fitting kinematic centre from kinemetry analysis. The average residuals per pixel are $33.5\,\mathrm{km\,s^{-1}}$. Second row: kinematic centre fixed at the position of the AGN. The average residuals per pixel are $35.3\,\mathrm{km\,s^{-1}}$. Image size is $820\times720\,\mathrm{pc}$.
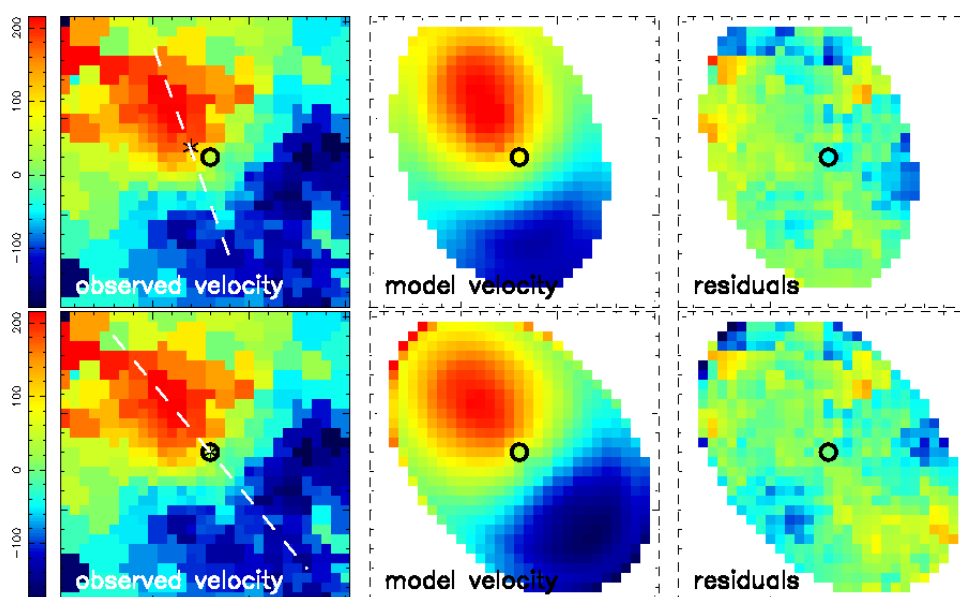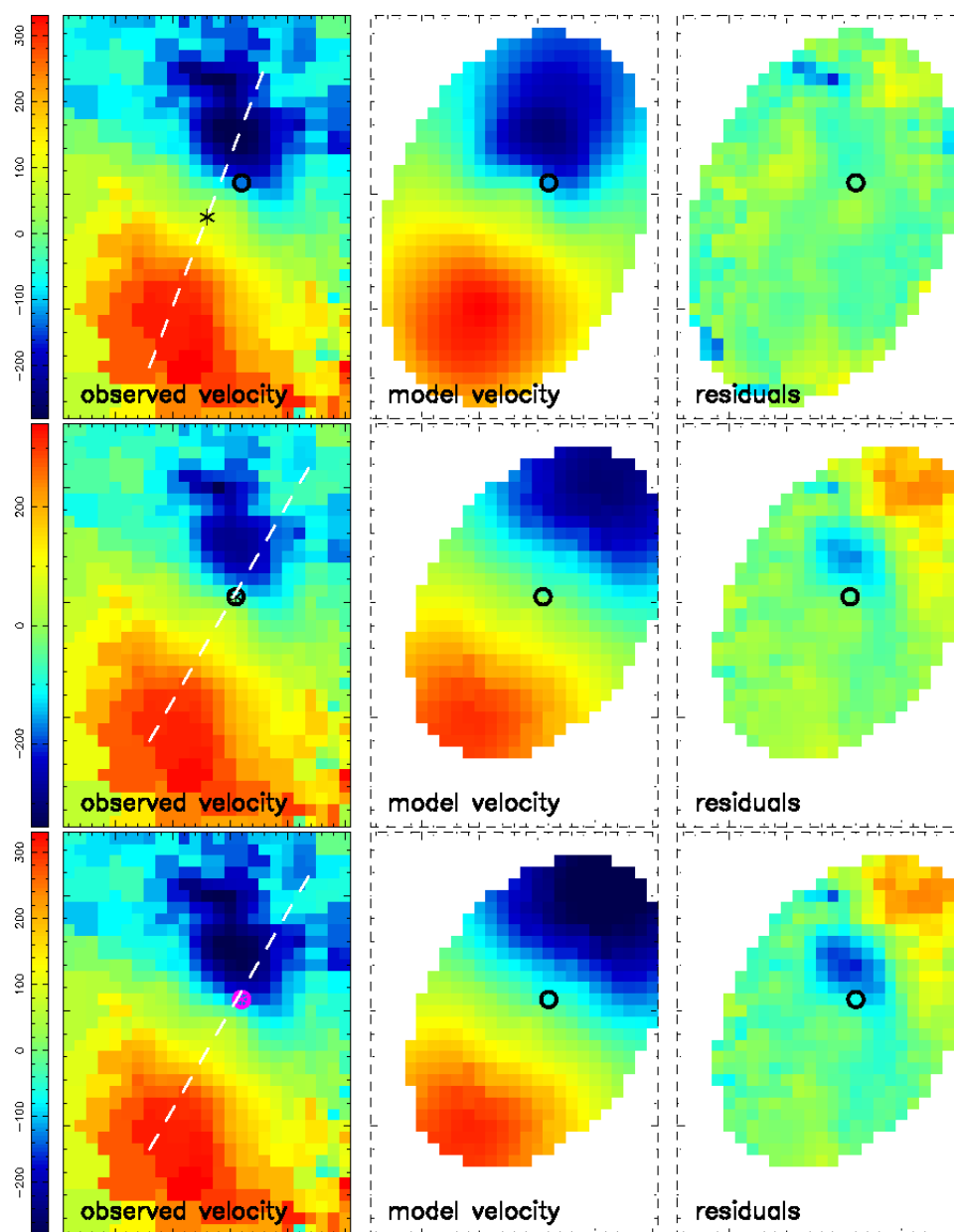
Figure 4.11: Southern Nucleus: Comparison of kinemetry models for different PAs and kinematic centres. It should be noted that the rotation curves do not differ significantly for the two different positions of the kinematic centre. Black circles indicate black hole positions; black stars represent the kinematic centre; the dashed white line traces the major axis of rotation. Left to right: velocity map, model, and residuals. First row: best-fitting kinematic centre from kinemetry analysis. Average residuals per pixel are $28.2\,\mathrm{km\,s^{-1}}$. Second row: kinematic centre fixed at the position of the AGN; average residuals per pixel are $45.9\,\mathrm{km\,s^{-1}}$. Third row: kinematic centre fixed at position of the AGN and performing fit only to southern half of nucleus. Average residuals per pixel over southern half are $21.1\,\mathrm{km\,s^{-1}}$. Image size is $600{\times}840\,\mathrm{pc}$.

that have been formed recently as a result of the interaction is superimposed on the light from the nucleus. As the stellar kinematics are derived from absorption lines, a superposition of two populations at different line-of-sight velocities would lead to an overestimate of the dispersion: the line resulting from such a superposition would appear broader than the intrinsic line widths of each of its constituent lines. Fitting the resulting line profile with a single kinematic component would lead to a significant over-estimate of the disperion. Support for this explanation is lent by Ohyama et al. (2003). Based on a study of the morphology and kinematics of the warm and cold gas, they argued that clouds along the line of sight to the northern half of the southern nucleus were being crushed in the interaction. In this scenario, if the cloud crushing leads to star formation, there would indeed be two superimposed populations at this location. This is supported by Spitzer observations of the Antennae galaxies, which show that the largest energy output, and thus a high rate of star formation, occurs in the overlap region between the two galaxies' nuclei (Brandl et al. 2009).

Although rather speculative, in the following discussion we consider whether this scenario can in principle account for both the increased dispersion and irregularities in the velocity in the northern half of the southern nucleus. Our aim is to use a very simple toy model to test the basic validity of the hypothesis by reproducing the characteristic features of the data; we do not attempt to match them exactly, nor to constrain the numerous parameters that would be required to do so.

We construct a two-population model as follows: the disk population is represented by a disk with the kinematic centre at the position of the AGN. PA, inclination, and velocity curve are found via a minimisation such as best to match the observed velocity field in the southern half. The dispersion is adopted from the radial dispersion curve derived from the southern half. We then subtract the disk velocity field from the observed velocity field in the northern half, and take this to be the velocity field of the second stellar population (thus ensuring that the observed velocity field is reproduced as closely as possible). In order to derive the resulting dispersion, we combine the two populations at each pixel by adding two Gaussians, with their centres corresponding to velocity and FWHM corresponding to dispersion (resembling the superposition of two absorption or emission lines). The resulting velocity field of the combination of both populations is then extracted by fitting a Gaussian to the result (resembling the method through which stellar kinematics are derived). As can be seen in Fig. 4.12, the model, whilst not matching the observations exactly, does reproduce the characteristic features of the data, displaying locally significantly increased velocity dispersions. The fact that the dispersion map is not reproduced exactly is due to the fact that we intentionally kept the model simple, assuming spatially constant, equal weightings and line FWHMs. We emphasise that the purpose of this exercise is simply to show that it is in principle possible to account for the locally significantly increased inferred dispersion through the effect of fitting a single velocity and dispersion to an absorption feature to which two stellar populations at different relative velocities have contributed. Although our assumptions that the two
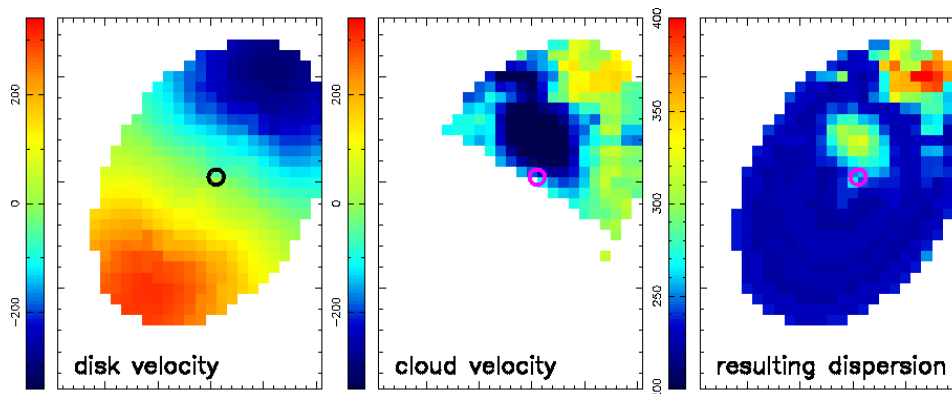
Figure 4.12: Southern Nucleus: Resulting apparent dispersion of the superposition of a 'disk' population and a 'cloud-crushing' population, both with velocity dispersions of $220\,\mathrm{km\,s^{-1}}$. Left to right: disk velocity field, cloud population velocity field, resulting apparent dispersion. Black circles indicate BH positions. The right panel shows that a simple 'disk plus cloud' model can produce an increase in dispersion, characteristic of that observed (Fig. 4.4). This indicates that the high dispersion in the northern half of the southern nucleus may be an artifact due to the presence of two kinematically different stellar populations with similar luminosities.

populations have the same luminosity and dispersion are simplistic, this underlines the point that a significantly better fit could be achieved if these parameters were allowed to vary. However, we feel that pursuing this is unjustified given constraints available from the data.

The total extinction-corrected luminosity emitted by the internuclear area with $\sigma \geq 330\mathrm{km\,s^{-1}}$ is $8.5 \times 10^8\,\mathrm{L_\odot}$. If this can be attributed in roughly equal shares to the old stellar population and the newly formed stars, it would imply a stellar mass of $\sim 10^8 M_\odot$ contained in the starburst population in this area. We speculate that this population may have originated from star formation associated with gas between the nuclei, perhaps in the tidal bridge or clump discussed in Section 4.8.

4.7 Jeans Modelling, Nuclear Masses, and Mass to Light Ratios

In this Section, we derive the mass and mass-to-light ratios of the two nuclei of NGC 6240 using Jeans models. The technical details of the technique in general and our approach in particular can be found in Chapter 2. However, we recapitulate the key points here.

An important aspect of our approach is that we separate the gravitational potential Φ from the distribution of the stars, i.e. we allow for non-stellar mass. We

assume isotropic velocity dispersion, which can be justified because the data do not allow us to say anything about the form of anisotropy, and this choice represents the least informative, and hence least constraining, option (Dejonghe 1986). Another issue is the shape of the stellar and total mass distribution. A disky system would be characterised by $\sigma/v_{rot} \ll 1$, and an oblate spheroidal system, in which the dispersion provides non-rotational pressure support thickening the disk, by a $\sigma/v_{rot} \gtrsim 1$. Fig. 4.4 shows that for both nuclei in NGC 6240 $\sigma/v_{rot} \sim 1$, suggesting that the latter is the more physically realistic choice. However, this is non-trivial to implement (see for example van der Marel & van Dokkum 2007). Instead we make the simplifying assumption that both the stellar distribution and potential are spherically symmetric, which will allow us to capture the characteristics of the system. It also has the advantage of yielding an analytical solution.

In order to assess the uncertainties of our result due to the choice of mass distribution, we also ran a set of models assuming an axisymmetric thin disk with an isotropic pressure component; the enclosed masses found with this model, which can be considered to be at the other end of the range of physically plausible models, agreed with the results of the spherically symmetric models within a factor of less than two. Häring-Neumayer et al. (2006) model the gas kinematics of Cen A with three different Jeans models: an axisymmetric thin disk with and without pressure terms, and a spherically symmetric model. They find that the inferred black hole masses span less than an order of magnitude. Comparing their results with those of others, these authors find that, whilst favouring the pressure-supported thin disk model as the most physically plausible, the spherical Jeans model agrees best with the results from Schwarzschild orbit superposition modelling by Silge et al. (2005). The uncertainty of Jeans modelling results due to the unknown velocity dispersion anisotropy is more difficult to assess due to the degeneracy between the integrated mass and the anisotropy parameter β. Both Wolf et al. (2010) and Mamon & Boué (2010) attempt to quantify this (see Fig. 1 in Wolf et al. 2010 and Fig. 1 in Mamon & Boué 2010) in the case of mass measurements for the Carina dSph and DM haloes, respectively, finding that the range spanned by results for the integrated mass assuming extreme values of β are large at small physical radii, decreasing to less than a factor of two at radii comparable to or larger than the half-light radius. Since a spheroidal system like the one we modelled is unlikely to have extremely anisotropic velocity dispersions, and since also we are measuring mass at radii larger than the half-light radius, we can assume the factor of two derived by these authors to be an upper limit on the error due to our choice of $\beta=0$. We thus estimate that the uncertainties introduced by the assumptions inherent in our modelling are unlikely to be larger than a factor of two.

Jeans modelling requires luminosity, rotational velocity, and velocity dispersion profiles as input. Since the region between the two nucleu is likely strongly perturbed, we measured azimuthally averaged profiles using only a 180° wedge in the outside halves (i.e. opposite the merger centre) of the galaxy, after subtracting the

continuum associated with the recent starburst (assuming an intrinsic $EW_{Br\gamma}$ of 22 Å,
as measured at the knot of Brγ emission north-west of the northern nucleus, cf. §4.9)
and correcting for extinction. To these we fitted a Sérsic function, constraining it
with the NIRC2 profile at $> 0.4''$, and with the extinction-corrected SINFONI profile
at $< 1.0''$ (i.e. some overlap between the two profiles is included). As part of the
fitting process, the model profile was convolved in 2D with the SINFONI PSF, to
account for beam smearing at small scales. We then analytically deprojected these
LOS luminosity profiles. The measured rotation curves and dispersion profiles need
to be corrected for beam smearing and projection along the line of sight in order to
recover the intrinsic kinematics. For this, we used the code described in Cresci et al.
(2009).

With these inputs, we compute M(r). The total mass enclosed within the cut-off
radius (250 pc and 320 pc for northern and southern nuclei, respectively) is found to
be $2.5 \times 10^9 M_\odot$ and $1.3 \times 10^{10} M_\odot$. This is comparable to that seen in the central
few hundred parsecs of nearby AGN (Figure 7, Davies et al. 2007). We also cal-
culate a global K-band mass-to-light ratio by finding the multiplication factor that
best matches the luminosity enclosed at radius r to M(r). L_K is taken to be the
total luminosity in the 1.9–2.5μm band in units of bolometric solar luminosity where
$1\,L_\odot = 3.8 \times 10^{26}$W (we note that a commonly used alternative is the definition via
solar K-band lumnosity density, 2.15×10^{25}W μm^{-1}). We obtain values of $5.0\,M_\odot/L_\odot$
and $1.9\,M_\odot/L_\odot$ for the northern and southern nuclei. Downes & Solomon (1998) find
typical gas fractions of $\sim$15% for local ULIRGs; in conjunction with these modelling
results, this implies total stellar masses of $2.1 \times 10^9 M_\odot$ and $1.1 \times 10^{10} M_\odot$, and stellar
mass-to-light ratios of $4.3\,M_\odot/L_\odot$ and $1.6\,M_\odot/L_\odot$ for the northern and southern nu-
clei, respectively. We discuss the possible inferences from these results regarding the
nature of the nuclei and the progenitors' Hubble types in §4.10.

It is tempting to compare the mass enclosed in the innermost few parsecs to the
expected black hole masses. One avenue to estimate the black hole masses is afforded
by the X-ray luminosities. Vignati et al. (1999) measure a total absorption-corrected
nuclear X-ray luminosity in the 2-10 keV range of 3.6×10^{44} erg s^{-1} with BeppoSAX.
Komossa et al. (2003), using *CHANDRA*, find that the northern and southern nu-
clei have absorption-corrected 0.1-10 keV X-ray luminosities of 0.7×10^{42} erg s^{-1} and
1.9×10^{42} erg s^{-1}, respectively. The discrepancy is most likely due to different absorp-
tion corrections (Komossa et al. 2003 derive $N_H \sim 10^{22}$cm^{-2}, Vignati et al. 1999
measure $N_H \approx 2 \times 10^{24}$cm^{-2}). Since Vignati et al. (1999) derive their absorption
correction from a significantly larger wavelength range (up to 100 keV) we use their
values for the following estimates. We convert the X-ray luminosity to monochro-
matic 5100 Å luminosity using the luminosity dependent α_{OX}-relation (Steffen et al.
2006; Maiolino et al. 2007), and then convert to AGN bolometric luminosity adopting
$L_{bol} = 7\nu L_\nu$ (5100Å) (e.g. Netzer & Trakhtenbrot 2007). Dasyra et al. (2006b) calcu-
late Eddington ratios for a sample of 34 ULIRGs, finding a median value of 0.37.
With this value for L_{bol}/L_{Edd}, we arrive at a combined black hole mass of $4 \times 10^8 M_\odot$.

However, the uncertainty on this estimate is at least a factor of a few.

Alternatively estimates can be derived from the stellar velocity dispersions. Using the M_{BH}-σ relation from Tremaine et al. (2002) and the stellar dispersions measured at the locations of the AGN ($\sim 200\,\mathrm{km\,s^{-1}}$ and $\sim 220\,\mathrm{km\,s^{-1}}$ for the northern and southern nuclei, respectively) yields expected central black hole masses of $1.4\pm0.4\times10^8 \mathrm{M_\odot}$ and $2.0\pm0.4\times10^8 \mathrm{M_\odot}$ for the northern and southern nuclei, respectively. The uncertainties on black hole masses derived from the M_{BH}-σ relation are also a factor of a few.

Finally, a measurement (with a rather smaller uncertainty) of M_{BH} in the southern nucleus can be made using high resolution stellar kinematics. Resolving the gravitational sphere of influence of the black hole and modelling the kinematics, Medling et al. (in prep.) derive a preliminary mass of $2.0 \pm 0.6 \times 10^9\,\mathrm{M_\odot}$.

Although the range of M_{BH} above spans an order of magnitude, the very large uncertainties of the first 2 estimates means that all the estimates are formally consistent (within $\sim 2\sigma$). We therefore caution against over-interpretation.

4.8   Merger Geometry & Stage, And Cold Gas Concentration

Starting from the assumption that the projected angular momenta of the nuclei are the true angular momenta, Tecza et al. (2000) proposed a merger geometry in which one of the nuclei is coplanar and prograde with the merger orbital plane, and the other is inclined with respect to the orbital plane (their Fig. 11). They further supported the notion of at least one of the galaxies being subject to a prograde encounter by noting that the formation of tidal tails such as those of NGC 6240 is favoured in prograde encounters. Here we would like to build onto and expand this discussion.

NGC 6240 indeed has long, well developed tidal tails, as can be seen in optical and HI data (Gerssen et al. 2004; Yun & Hibbard 2001), covering a projected size of ~ 45 kpc from north to south, about half that of the Antennae. In the HST images, a continuous dust distribution across the centre strongly suggests that what we are seeing is an extended, well developed single tail curving in front of the system, rather than a series of disconnected shorter features. However, NGC 6240's tails are not as dense or long as those of e.g. the Antennae. What can we derive from this with regard to the merger geometry? It is generally known that in merger simulations, the more coplanar/prograde, and thus 'resonant', an encounter is, the stronger the resulting tidal tails are. It is quite clear however, from looking at the relative orientation of the rotation axes of the nuclei, that NGC 6240 cannot be a perfectly coplanar merger. But a merger must not be exactly coplanar and prograde in order to produce tidal tails – an example of this is NGC 7252, which has tidal tails akin to those of NGC 6240. NGC 7252's tidal features were successfully reproduced through N-body simulations by Hibbard & Mihos (1995); their simulation had one of the progenitors on

a coplanar, prograde encounter, but the other galaxy at an inclination of ~ 45 degrees to the orbital plane – this illustrates that there is a non-negligible merger parameter space around 'coplanar/prograde' which will also result in pronounced tidal tails. Therefore, whilst not pinning down the merger geometry exactly, the existence of such long and well developed tidal tails is convincing evidence that the merger geometry must be within a reasonable parameter space around prograde/coplanar. The stellar kinematics at first sight seem to disagree with this, giving the appearance that the nuclei are counter-rotating. However, co-rotating nuclei would also look like this if one nucleus is inclined behind the plane of the sky, and the other in front. Thus the stellar kinematics are consistent with the view that NGC 6240 is not too far from being a prograde merger. That the nuclei are clearly not exactly aligned could be the reason for the additional shorter tails that make the system look rather messy. We therefore conclude that NGC 6240's merger geometry most likely tends towards coplanar/prograde, and in this sense is perhaps quite similar to the geometry proposed for NGC 7252 by Hibbard & Mihos (1995).

It is more difficult to deduce the stage of merging the two galaxies comprising NGC 6240 are currently in - we cannot pin down their merger geometry exactly, as discussed above, and neither do we know the 3D relative velocities of the two nuclei, so we cannot calculate whether the two nuclei will merge immediately or separate again before eventually coalescing. We know that they must certainly have already experienced their first close encounter, since tidal tails only form after the first strong gravitational interaction of the two galaxies. This is also supported by the high luminosity of the system, because elevated levels of star formation also are only expected after the first encounter leads to collision and compression of gas complexes. And the fact that the two nuclei are still separated by about a kpc in projection indicates that the system is not yet at the 'final coalescence' phase.

The observed peak of the gas emission between the nuclei (Fig. 4.5), which Tacconi et al. (1999) found to display a velocity gradient and interpreted as due to a self-gravitating gas disk located in between the nuclei, is puzzling, since from merger simulations this is generally not expected to occur. We could be seeing a collapsed gas clump in a tidal arm - such features are found to occur quite often in simulations of merging galaxies above a certain gas fraction (Wetzstein et al. 2007; Bournaud et al. 2008), and are also seen in observations (Knierman et al. 2003). An alternative, and perhaps more likely, interpretation of this gas concentration is a tidal bridge connecting the two nuclei that is viewed in projection. Such tidal bridges are often seen in merger simulations. However, simulations have never yielded a system in which the total gas mass is dominated by that between the nuclei. And although bridges are produced most strongly in a perfectly prograde coplanar encounter (which, as discussed above, is inconsistent with our observations), as one deviates from a prograde coplanar geometry the strength of the bridge decreases.

An alternative, although somehwat rarer, way to drive a significant gas mass away from the nuclei is a direct interaction (i.e. low impact parameter), in which the ISM of

the progenitors collides. The best example of this is UGC 12914/5 (the Taffy Galaxies; Braine et al. 2003), in which about 25% of the CO emission originates between the nuclei. In this system, the progenitors collided at about $600\,\mathrm{km\,s^{-1}}$. Braine et al. (2003) argued that while this would have ionised the gas, the cooling time is short enough that H_2 could reform while the disks are still passing through each other. From the ratio of ^{12}CO to ^{13}CO these authors found that the optical depth of CO in the bridge was far less than on the nuclei. Combined with the effect of increased CO abundance due to grain destruction, this led them to suggest that the actual mass of molecular gas may be rather less than implied by the CO luminosity, perhaps only $\sim 6\%$ of the total gas mass. Since direct collisions such as these tend to create ring galaxies (or in the case of the Taffy Galaxies, an incomplete ring or hook), this scenario seems unlikely for NGC 6240.

In NGC 6240, the CO map indicates that CO luminosity is dominated by that between the nuclei. We must therefore also consider factors that could significantly affect the flux-to-mass conversion factor in the two regions. It is already known that sub-thermal emission from non-virialised clouds can radically modify the CO-to-H_2 conversion factor, as shown in Fig. 10 of Tacconi et al. (2008). Such an effect could easily boost the emission from gas in a drawn-out, thin and diffuse gas bridge compared to denser material around the nuclei. And it is supported by other observations: a comparison of the CO line emission (Fig. 4.5) with the $1.315\,\mathrm{mm}$ continuum measured by Tacconi et al. (1999) (their Fig. 3, left panel) shows that the dust, as traced by the mm continuum, is concentrated on the nuclei rather than following the CO line emission. Furthermore, in a detailed analysis of various CO transitions, Greve et al (2009) were unable to find a single set of average H_2 conditions that comes close to reproducing the observed line ratios. A second important issue is the impact of X-ray irradiation on the CO abundance around the nuclei, since the AGN are quite luminous. Lutz et al. (2003) argue that as little as 25–50% of L_{bol} is due to the AGN. If we take the lower end of this range, and distribute it equally between the two AGN, we find each radiates at $L \sim 3 \times 10^{44}\,\mathrm{erg\,s^{-1}}$. We also adopt a column of $2 \times 10^{24}\,\mathrm{cm^{-2}}$ (Vignati et al. 1999) and assume a gas density of $10^5\,\mathrm{cm^{-3}}$. Under these conditions, hard X-rays from the AGN will cause sufficient ionisation to reduce the CO abundance an order of magnitude below its typical value of 10^{-4} out to a radius of $250\,\mathrm{pc}$ (see Boger & Sternberg 2005, and Davies & Sternberg in prep.). Thus, even if there is significant gas mass around the nuclei (as the models imply), one would expect rather little CO emission. That these effects will conspire to make the CO luminosity distribution look rather different to the molecular gas mass distribution should be borne in mind.

4.9   Scale of Starburst & Star Formation History

While Tecza et al. (2000) concluded that the nuclei were the progenitor bulges, they did not quantify how much of the K-band luminosity arises in the recent starburst

and how much is due to the progenitor bulges themselves. Our data enable us to resolve this issue. Our method is to measure an average value for $\mathrm{EW}_{Br\gamma}$ away from the nucleus where dilution from the bulge is small, and assert that this is representative of the whole starburst. The fundamental assumption is that, integrated over a sufficiently large aperture, we are summing a fair cross-section of star clusters and hence probing the average star formation properties. This minimises the impact of the stochastic nature of individual clusters. We have therefore chosen a region containing a high density of clusters, and measured $\mathrm{EW}_{Br\gamma}$ in a $0.8''$ aperture corresponding to $400\,\mathrm{pc}$ so that many clusters are included. Such a region lies about $1''$ to the west of the northern nucleus (Pollack et al. 2007), sufficiently far that the K-band continuum from the nucleus is very faint. Fig. 4.13 shows that, despite the Brγ flux being higher on the nuclei, both here (and also in other off-nuclear regions) $\mathrm{EW}_{Br\gamma} = 22 \pm 6\,\text{Å}$. We use it to obtain the fractional contribution of the young stellar population in $1''$ diameter apertures centred on the nuclei, by dividing the measured $\mathrm{EW}_{Br\gamma}$ by this intrinsic value. We then find the K-band luminosity emitted by the starburst population to be $3.6 \times 10^8 L_\odot$ (northern nucleus) and $1.3 \times 10^9 L_\odot$ (southern nucleus), implying $\mathrm{L}_{K,young}/\mathrm{L}_{K,total}$ to be 0.36 (northern nucleus) and 0.32 (southern nucleus) – i.e. only about 1/3 of the total K-band luminosity of the nuclei is due to recent star formation.

This implies that the K-band luminosity of the nuclei is dominated by a population of stars older than $20\,\mathrm{Myr}$. An important question is whether this is consistent with claims that one needs supergiant templates in order to match the CO bandhead depth (Lester et al. 1988; Sugai et al. 1997; Tecza et al. 2000). In the following, we show that basing conclusions about the dominant stellar population on a fit to a single template is very uncertain. The tables in Origlia et al. (1993) and Förster Schreiber (2000) show that the equivalent widths of the CO bandheads vary considerably between individual stars; and it is also well known that higher metallicity populations have deeper bandheads because the K-band continuum is dominated by cooler stars. The templates found by Tecza et al. (2000) and Sugai et al. (1997) to provide the best fit to the K-band absorption features are of K4.5 Ib and K2.5 Ib stars, respectively: i.e. specifically K type sub-luminous supergiants. Both authors infer from this that the dominant stellar population is late type supergiants. Tecza et al. (2000) go on to conclude that these were produced as a result of a burst of star formation that lasted for $5\,\mathrm{Myr}$ and occurred $\sim 20\,\mathrm{Myr}$ ago. We have examined the Tecza et al. (2000) starburst scenario in detail using the population synthesis code STARS, and found that it would lead to $\sim 60\%$ of the K-band luminosity being due to M supergiants (cooler than $4000\,\mathrm{K}$) and only $\sim 3\%$ due to K supergiants (temperatures 4000–4600 K). Thus the scenario of a $\sim 20\,\mathrm{Myr}$ old starburst leads to two apparent contradictions: How can M supergiants dominate the luminosity and yet have absorption features too deep to match the spectrum? And how can K supergiants provide a good match to the spectrum and yet contribute only an insignificant fraction of the luminosity? The resolution is simply that the galaxy spectrum consists of many different types of

stars, and a single template can at best be characteristic of the sum of all these. The important conclusion here is that while the composite spectrum is best matched by a supergiant template, other types of stars still make up a significant fraction of the near-infrared continuum.

Another key point of interest are the past and future star formation rates. Di Matteo et al. (2007, 2008); Cox et al. (2006, 2008) offer a large sample of medium-resolution simulations comprehensively covering a large range of gas fractions, merger geometries, and mass ratios, as well as employing different codes. Their synthesised results regarding the qualitative evolution of the star formation during a merger are that nearly all encounters are marked by at least two peaks in the star formation rate; one at the first encounter, and one upon final coalescence. However, the relative strength of the two peaks differs, depending on the merger geometry; but on average the second peak is stronger (Di Matteo et al. 2007, 2008). This is particularly evident for mergers that tend towards coplanar/prograde geometries, as appears to be the case for NGC6240.

The aforementioned simulations were carried out at medium resolution, and thus one may wonder if their results would change when going to higher resolution simulations resolving the multiphase ISM. However, as Bournaud et al. (2008); Teyssier et al. (2010) show, the qualitative evolution of the star formation rate during a merger remains largely unchanged, the only significant difference is that star formation proceeds much more effectively, resulting in predicted star formation rates a factor of up to ten times larger than those predicted by lower-resolution simulations (Teyssier et al. 2010).

We therefore conclude that NGC 6240, being between first encounter and final coalescence, most likely has experienced a peak in star formation rate in the recent past (triggered by the first encounter), has currently elevated levels of star formation compared to a quiescent galaxy, and will experience another peak in star formation rate, likely stronger than the first one, in the near future when the galaxies coalesce. This is supported by the observed Brγ emission, which indicates that star formation must currently still be on-going, and by measurements of cluster ages (Pollack et al. 2007) which are found to be typically very young – in a population of clusters with a range of ages, it is the brighter ones that are more easily detected, and because clusters fade quickly, these will also inevitably be younger. We furthermore note that since NGC 6240 is already just below the canonical ULIRG threshold of $L_{IR} \gtrsim 10^{12} L_{\odot}$, it is safe to assume that it will breach this threshold once the final starburst is triggered, and will become a *bona fide* ULIRG.

In order to be able to make more quantitative analyses, we use STARS to calculate a range of observables from two star formation histories, which both display the generic features discussed above; an initial peak at first encounter followed by a gradual rise or plateau, and a final intense burst. One of these simulations is selected from a set of simulations intended to reproduce the properties of the Antennae galaxies (Karl et al. 2008, 2010), and the other one from the library of Johansson et

al. (2009). Neither are coplanar/prograde, althought they tend towards it, and both produce well-developed tidal tails during the interaction. The rationale of using star formation histories from two different simulations is to provide an estimate of the uncertainties introduced by the quantitative differences introduced by the exact simulation details. Since we only know that NGC 6240 must be between first encounter and final coalescence, we use the full range of simulated properties between these two points, as well as our measurement and associated uncertainties of $EW_{Br\gamma}$, as constraints to derive the uncertainties in the star formation properties.

In Table 4.2, we have used these star formation histories to calculate the mass of young stars formed in both scenarios, as well as the current star formation and supernova rates. To do so, we have applied a scaling so that the K-band luminosity matches that observed for each nucleus, under the assumption that the evolution of the central SFR mirrors that of the global SFR. The table shows that quantitatively the results for the two different star formation histories do not differ greatly – in fact, the variation within each scenario over the possible time range is larger than the variation between the averages of the two cases.

One conclusion is that the bolometric luminosity of the starburst from the two nuclei together is only 20–30% of the system's total. This follows in the same direction as Lutz et al. (2003) that the recent starburst only contributes part of the total luminosity. We estimate a somewhat lower fraction than Lutz et al. (2003), who constrain the starburst contribution to be 50 to 70%, posssibly due to the fact that we are looking at the central region whereas they investigated the global luminosities.

An important concern is that our results appear to be inconsistent with those of Beswick et al. (2001) who find, based on the 1.4 GHz continuum, significantly larger star formation and supernova rates of $83.1 \, M_\odot \, yr^{-1}$ and $1.33 \, yr^{-1}$. We argue that this is due to the different star formation histories adopted. We show that this can have a major impact on interpretation of the data, and that accounting for it makes the radio continuum data consistent with our results.

We first address a minor correction, specifically a $\sim$10% increase in radio flux due to the larger aperture used by Beswick et al. (2001), which included a substantial flux contribution from an off-nuclear source not included in our apertures ('N2' in their nomenclature, see their Fig. 2). A larger correction may be needed by analogy to Arp 220 for which Rovilos et al. (2005) examined the 18-cm lightcurves of the supernovae. They found the type IIn RSNe model insufficient and arrived at a supernova rate that was a factor of $\sim$3 smaller than the $\sim 2 \, yr^{-1}$ often quoted. A similar correction may be applicable to the rates inferred from radio measurements for NGC 6240. This may be related to the third issue, which concerns the star formation history. The formulae used by Beswick et al. (2001) to convert 1.4 GHz luminosity to star formation and supernova rates (based on work by Condon & Yin 1990; Condon 1992; Cram 1998) were derived empirically based on measurements of normal disk galaxies for which a constant star formation rate is characteristic. This implicit constant star formation rate is very different to the increasing star formation rate found in merger

simulations. We show below that this can make as much as a factor of three difference in the star formation and supernova rates that are derived from observables.

We use STARS to estimate the star formation rate from a given K-band luminosity for three different star formation histories. First, following Beswick et al. (2001), we adopt continuous star formation for a duration of $20\,\mathrm{Myr}$, corresponding to that estimated by Tecza et al. (2000), Pasquali et al. (2003), Pollack et al. (2007) for the most recent star burst. In order to reach $L_K{=}1.7{\times}10^9 L_\odot$, corresponding to the total measured for the starburst population, we require a constant SFR of $25\,\mathrm{M_\odot\ yr^{-1}}$. On the other hand, for the recently increasing star formation rate typical of the merger scenarios, we find star formation rates of $\sim 10\,\mathrm{M_\odot\ yr^{-1}}$. Thus we find a factor ~ 2.5 difference in the SFR required to reach the same K-band luminosity, depending on the star formation history. We can estimate the supernova rates in a similar way: For $20\,\mathrm{Myr}$ of continuous star formation at $25\,\mathrm{M_\odot\ yr^{-1}}$, we calculate a supernova rate of $0.3\,\mathrm{yr^{-1}}$. In contrast, for our merger scenarios, we find supernova rates of $\sim 0.13\,\mathrm{yr^{-1}}$. Thus, much of the discrepancy between our supernova rate and the (corrected) value from Beswick et al. (2001) is due to the different star formation histories adopted.

This illustrates an important *caveat*: the choice of star formation history can have a far-reaching impact on the interpretation of the observables. We note that the very similar derived stellar population parameters for our two different merger star formation histories indicate that, for mergers, using a 'characteristic' star formation history (i.e. an initial peak at first encounter followed by a gradual rise or plateau, and a final intense burst) will yield much more reliable quantities than either instantaneous or continuous star formation models.

simulation	nucleus	$L_{K,young}$	$L_{bol,young}$	mass of young stars	SFR	SNR
'1'	North	$3.6 \times 10^8 L_\odot$	$2.9^{+0.5}_{-0.7} \times 10^{10} L_\odot$	$4.2^{+1.3}_{-0.4} \times 10^8 M_\odot$	$2.3^{+1.8}_{-0.7} M_\odot yr^{-1}$	$0.03 \pm 0.1 \, yr^{-1}$
'2'	North	$3.6 \times 10^8 L_\odot$	$3.1^{+0.4}_{-0.3} \times 10^{10} L_\odot$	$3.7 \pm 0.3 \times 10^8 M_\odot$	$2.2^{+0.4}_{-0.3} M_\odot yr^{-1}$	$0.03 \pm 0.01 yr^{-1}$
'1'	South	$1.3 \times 10^9 L_\odot$	$10.0 \pm 2.0 \times 10^{10} L_\odot$	$1.5^{+0.5}_{-0.1} \times 10^9 M_\odot$	$8.2^{+6.8}_{-2.4} M_\odot yr^{-1}$	$0.11^{+0.02}_{-0.04} \, yr^{-1}$
'2'	South	$1.3 \times 10^9 L_\odot$	$11.0^{+2.0}_{-1.0} \times 10^{10} L_\odot$	$1.3 \pm 0.1 \times 10^9 M_\odot$	$7.8^{+1.7}_{-1.1} M_\odot yr^{-1}$	$0.10^{+0.02}_{-0.01} \, yr^{-1}$

Table 4.2: Characteristics of Starburst Populations. $L_{K,young}$ was measured in $1''$ diameter apertures using the dereddened continuum flux map and adopting an intrinsic $EW_{Br\gamma} = 22$ Å (see §4.9). Values for L_{bol}, stellar mass, and SFR were inferred from this together with the star formation history from the simulations at all points between first encounter and coalescence; given are the median value and the range sampled.

4.10   Stellar Populations of NGC 6240

Did the Progenitors Have Bulges?   The existence or otherwise of bulges (where 'bulge' here includes both pseudobulges and classical bulges) in the galaxies under-going a merger has a profound impact on the star formation (Mihos & Hernquist 1996). Springel et al. (2005c) show in their Fig. 15 that in a major merger of disks (gas fraction 10%) without bulges, the first encounter already triggers an episode of enhanced star formation that lasts for 300–400 Myr. The second encounter triggers a more intense, but also somewhat shorter ($\sim$50 Myr), starburst 800–900 Myr later. In a simulation that included a bulge and a central black hole, there was almost no perceptible change in the star formation rate at the first encounter. This remained constant at $\sim$5–10% of the peak star formation rate until the second encounter, when the starburst is triggered and the peak star formation rate was achieved. Because there had been no earlier phase of enhanced star formation, this starburst is more intense than it would be without a bulge. Which of these two different scenarios holds true for NGC 6240?

   The evidence overwhelmingly points towards the progenitors having had a promi-nent bulge component. First, the majority of massive spirals at low redshifts have bulges, although at $z \gtrsim 2$ the situation may well be different as bulges may not yet have had time to grow (Genzel et al. 2009). Second, we know that both nuclei host an AGN and therefore harbour a supermassive black hole. The implication of the M_{BH}-$\sigma*$ relation is therefore that the progenitors must have had bulges. Using estimates of the black hole masses based on the AGN luminosity and our measured stellar dispersion (§4.7) in conjunction with the empirical correlation between M_{BH} and bulge mass (Häring & Rix 2004) yields associated bulge masses of $8.7 \times 10^{10} M_{\odot}$ and $1.2 \times 10^{11} M_{\odot}$ for the northern and southern nuclei respectively, an order of mag-nitude larger than their dynamical masses. However, due to their transformational impact on both black hole and host galaxy, it is uncertain whether such scaling rela-tions can be expected to hold during on-going mergers. An argument favouring the existence of bulges in the progenitors stems from the merger simulation: the galaxies in our simulation had bulges, and the good match to the observed $\mathrm{EW}_{Br\gamma}$ suggests that the star formation history is reasonable. As Springel et al. (2005c) and Di Mat-teo et al. (2007, 2008) show, bulgeless mergers have markedly different star formation histories, with the first encounter producing the most potent burst of star formation (It should furthermore be noted that in higher-resolution simulations, the starburst triggered by the final coalescence occurs somewhat earlier; cf. Teyssier et al. 2010.). Thus, at the current phase, we would expect to see significantly lower $\mathrm{EW}_{Br\gamma}$ if the first encounter had indeed triggered the more powerful star formation event.

Are the Nuclei the Progenitors' Bulges?   Are the nuclei we see (remnants of) the progenitor galaxies' bulges, did they originate only in the first encounter a few 100 Myr ago, or is the rotation we see the signature of stellar disks? The latter is
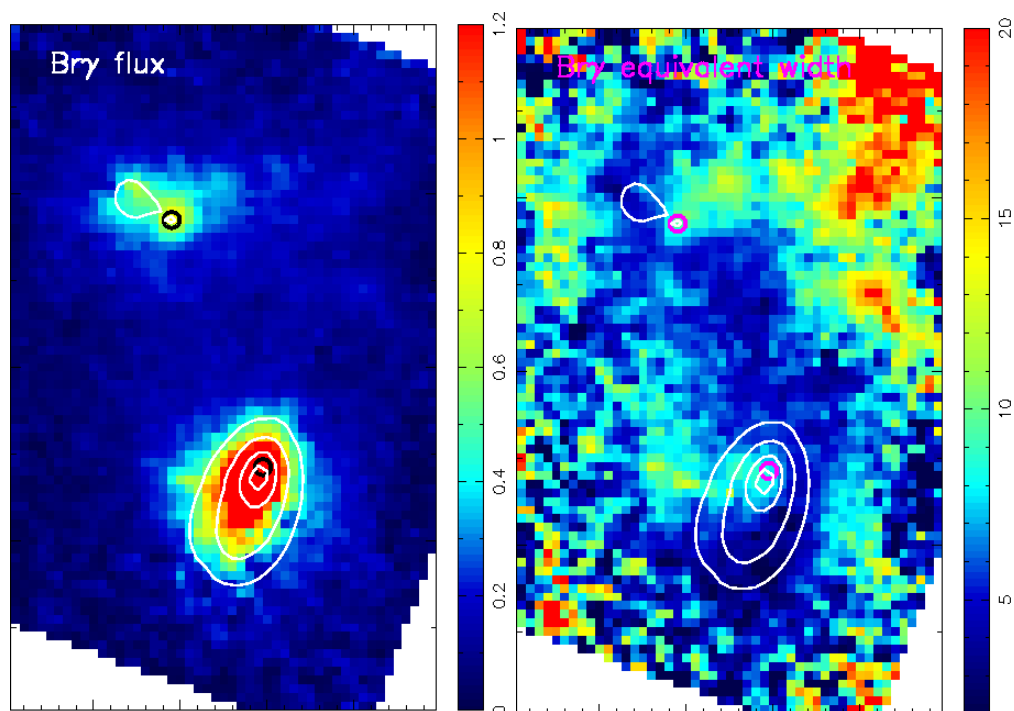
Figure 4.13: Left: Map of Brγ flux (units given in $10^{-16}\,\mathrm{W\,m^{-2}}\,mu$m). Right: Map of $\mathrm{EW}_{Br\gamma}$ (units given in Å). White contours tracing the K-band stellar continuum, and black circles denoting the black hole locations are overdrawn on both maps. Although the most intense Brγ emission is on the nuclei, the equivalent width here is lowest, suggesting that the K-band light is dominated by an older stellar population. We note that in §4.4 we showed that dilution by hot dust emission associated with the AGN cannot play a role in reducing $\mathrm{EW}_{Br\gamma}$.
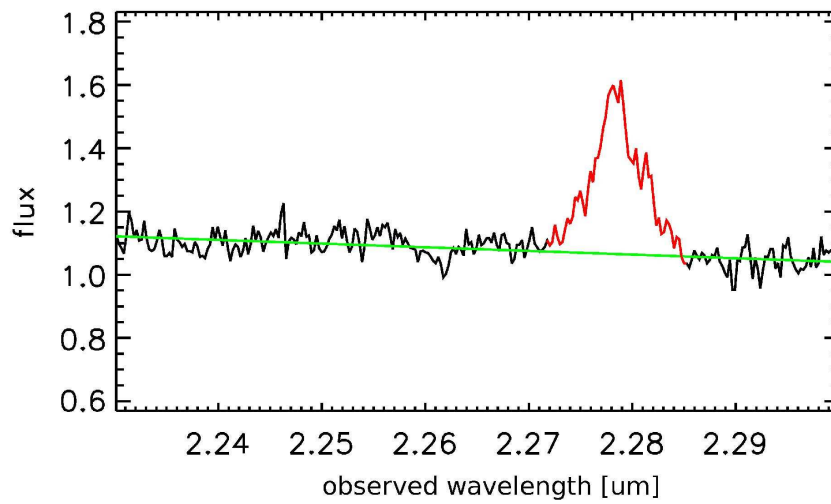
Figure 4.14: Spectrum of the region to the northwest where the $EW_{Br\gamma}$ is not diluted by continuum emission from the progenitors, integrated over an $0.8''$ diameter aperture. The flux is in units of $10^{-16}\,\mathrm{W\,m^{-2}}\,mu\mathrm{m^{-1}}$. The measured $EW_{Br\gamma}$ is 22 ± 6 Å.

unlikely, since the high dispersion clearly indicates a thickened structure, and nuclear stellar disks in contrast are often accompanied by sigma-drops (Peletier et al. 2007). Tecza et al. (2000) proposed the first, based on an estimate of the global mass-to-light ratio of the nuclei. Our high spatial resolution data allow us to explore this in more detail using not only the mass and luminosity, but also the effective radius and kinematics, and our knowledge of the stellar populations.

Table 4.3 quantifies the kinematics, luminosities, masses, and sizes of the two nuclei. How do these compare with the characteristics expected of a bulge? An argument in favour of the nuclei being bulges is supplied by estimates of the mass-to-light ratio of the non-starburst stellar population: correcting the global stellar mass-to-light ratios (§4.7, assuming a gas fraction of ∼15%) for the starburst contribution (Table 4.2), we find that the non-starburst nuclear populations must have mass-to-light ratios of ∼ $5.2\,M_{\odot}/L_{\odot}$ (northern nucleus) and $1.8\,M_{\odot}/L_{\odot}$ (southern nucleus) – noting that the associated uncertainties are estimated to be about a factor of two. If the nuclei only formed after the first encounter (∼560 Myr ago in the 'Antennae' scenario), they should have a M/L_K of *at most* $2\,M_{\odot}/L_{\odot}$, whereas a several Gyr old stellar population has a M/L_K of ∼6–10 $M_{\odot}/L_{\odot}$ (cf. Fig. 5.7). This, as well as the small relative contributions of the starburst population to the nuclear masses and luminosities, indicates that a substantial fraction of the nuclei consists of stars predating the beginning of the merger.

NGC 6240 has often been cited as having anomalously high stellar dispersion. However, excluding the region towards the northern half of the southern nucleus which we discuss in §4.6, the dispersions typical for the nuclei are ∼200 km s^{-1}. These are not unusual for late-type bulges, as Fig. 18 in Kormendy & Kennicutt (2004) shows. Placing the two nuclei on the ϵ vs. v_{max}/σ diagram of Kormendy & Kennicutt (2004) (their Fig. 17), it appears that the northern nucleus lies comfortably within the region typical for late-type pseudobulges, whereas the southern nucleus would represent a somewhat more extreme case, having a higher v_{max}/σ than other galaxies. In both cases, however, the kinematics strongly support the case for a disk-like, secularly-grown pseudobulge rather than a merger-formed classical bulge. The Sérsic indices are rather typical of classical bulges, but we caution that the luminosity profiles are disturbed and influenced by recent star formation, and hence the values derived from the Sérsic fits should be treated with caution. For the same reason, we prefer to measure the sizes from the extents to which rotation can be seen (indicating the extent to which the nuclei dominate the light distribution), rather than the effective radii obtained from the Sérsic fits; this gives radii of 265 pc and 290 pc for the northern and southern nuclei, respectively (as opposed to 490 pc and 180 pc based on the Sérsic fits). This places them at the lower end but within the range given by Moriondo et al. (1999) who measure the bulge radii for 40 spiral galaxies and find values ranging from 230 pc to 1.93 kpc with an average of 650 pc. The same authors also look at the bulge masses, where they find values from $1.4\times10^9 M_{\odot}$ to $1.8\times10^{11} M_{\odot}$ with an average of $2.5\times10^{10} M_{\odot}$. Our analysis (§4.7) yields masses of $2.5\times10^9 M_{\odot}$ and $1.9\times10^{10} M_{\odot}$, again

at the lower end but within the range found by Moriondo et al. (1999).

Would we expect the bulges to survive to this merger state? Comparatively little is known about the evolution of galaxy bulges during mergers. Observationally, Agüero et al. (2001) report velocity dispersions of $217\,\mathrm{km\,s^{-1}}$ and $280\,\mathrm{km\,s^{-1}}$ in the two nuclei of the merger system AM 2049-691, and Shier et al. (1998) investigate 11 multiple-nucleus merging objects and find nucleus sizes between 200 and 1600 pc (on average 600 pc), velocity dispersions of $66\text{-}151\,\mathrm{km\,s^{-1}}$ (excluding NGC 6240, which was also sampled) with an average of $109\,\mathrm{km\,s^{-1}}$. However, these were to a large part galaxies in earlier merger stages. Hernquist (1993) simulates the merger of two spiral galaxies with bulges. His model suggests that the bulges remain very nearly intact until final coalescence. The spin (rotational velocity) is reported to remain nearly constant throughout the simulated merger.

In light of this and the fact that the nuclei are found towards the lower end of the range of masses and sizes found for a large sample of spiral galaxy bulges, we conjecture that the nuclei are indeed the progenitor galaxies' bulges, most likely pseudo-bulges, that have had their outer, less tightly bound layers stripped off during the merger, leading to the sub-average sizes. Dispersion may have increased due to 'heating' during the interaction by gravitational impulse, and a gravitational potential deepened by influx of gas into the central region. Since the progenitors did not only have a prominent bulge component, but must also have had substantial disks in order to allow such pronounced tidal features as we observe to develop, the progenitors were most likely of Hubble type Sa/Sb.

nucleus	v_{max}	σ	n	ϵ	r_{eff}	r_{kin}	L_K	M_{dyn}	M_{dyn}/L_K
North	$205\,\mathrm{km\,s^{-1}}$	$200\,\mathrm{km\,s^{-1}}$	2.8	0.3	$490\,\mathrm{pc}$	$265\,\mathrm{pc}$	$1.1{\times}10^9\mathrm{L_\odot}$	$2.5{\times}10^9\mathrm{L_\odot}$	$5.0\,\mathrm{M_\odot/L_\odot}$
South	$300\,\mathrm{km\,s^{-1}}$	$220\,\mathrm{km\,s^{-1}}$	2.8	0.35	$180\,\mathrm{pc}$	$290\,\mathrm{pc}$	$5.9{\times}10^9\mathrm{L_\odot}$	$1.3{\times}10^{10}\mathrm{L_\odot}$	$1.9\,\mathrm{M_\odot/L_\odot}$

Table 4.3: Properties of the Nuclei. v_{max} is the peak measured stellar velocity, σ is the average/typical stellar dispersion (§4.2.1.4); n and r_{eff} are the Sérsic index and effective radius of the light profile (§4.7), ϵ is the ellipticity (§4.5), r_{kin} is the extent to which rotation is seen, L_K the total K-band luminosity (§4.4), and M_{dyn} the dynamical mass as derived from the Jeans modelling (§4.7).

4.11   Summary

We present new adaptive optics integral field spectroscopy near-IR data and CO(2-1) interferometric line observations of the nearby merger system NGC 6240. Our main conclusions are:

- The Calzetti et al. (2000) reddening law provides the best fit to photometric data points spanning 0.45μm to 2.22μm. The spatially resolved extinction is generally moderate, with $A_K \sim 2$–4.

- The locations of the stellar kinematic centres are consistent with the black hole locations proposed by Max et al. (2007). However, an additional stellar population along the line of sight may be perturbing the velocity field of the southern nucleus and causing the higher dispersion across the northern side.

- Jeans modelling of the stellar kinematics, assuming spherical symmetry and isotropic dispersion, gives $M = 2.5 \times 10^9 M_\odot$ and $M/L_K = 5.0\,M_\odot/L_\odot$ for the northern nucleus (out to 250 pc), and $M = 1.9 \times 10^{10}\,M_\odot$ and $M/L_K = 5.0\,M_\odot/L_\odot$ for the southern nucleus (out to 320 pc).

- The presence of tidal arms, and the still-separated nuclei indicate that NGC 6240 must be between first encounter and final coalescence. The stellar velocity field, and strength and prominence of the tidal arms indicate that this system is not perfectly, but reasonably close to prograde coplanar.

- Although simulations can produce significant projected gas mass between the nuclei, these are never as prominent as the observed concentration in CO luminosity. In order to explain this, additional physical effects such as spatial differences in CO-to-H_2 conversion factor or CO abundance are needed.

- Star formation histories from numerical simulations display generic features. Using these in combination with our constraints on the merger stage and measurements of $\mathrm{EW}_{Br\gamma}$, we calculate the properties of the young starburst population. We find that recent star formation accounts for only about 1/3 of the total K-band luminosity. Thus the stellar luminosity is dominated by stars predating the merger.

- Whereas the differences between the starburst properties inferred from different merger star formation histories appropriate to NGC 6240 are markedly small, adopting a constant star formation rate yields very different results (such as a factor 3 change in the derived SFR). We conclude that, when characterising the star formation properties of a merger, a 'generic' merger star formation history should be adopted in preference to either instantaneous or constant star formation histories.

- After accounting for the recent star formation, the mass-to-light ratios of the remaining stellar population are $5.2\,M_\odot/L_\odot$ and $1.8\,M_\odot/L_\odot$ for the northern and southern nuclei respectively. This implies that a population of stars older than $\sim$1 Gyr contributes the majority of the nuclear stellar masses and luminosities. Combined with the measured size and V/σ, as well as results from the simulations, it implies that the two nuclei are the remnants of the bulges of the progenitor galaxies.

Chapter 5

Arp 220

This chapter is an almost exact reproduction of the following publication:

- "Arp 220: extinction & merger-induced star formation"
  Engel H., Davies R. I., Genzel R., Tacconi L. J., Sturm E., Downes D., 2010,
  ApJ, to be submitted

5.1   Introduction

Arp 220 ($L_{IR} = 1.4 \times 10^{12} L_\odot$, Soifer et al. 1987) is the closest ULIRG representative (D = 73 Mpc; z = 0.018, $1'' = 352$ pc) and thus a unique laboratory for the investigation of this important class of galaxies. As such, it has been extensively studied and is widely regarded as the prototypical ULIRG. It is an advanced merger; tidal tails and distortions are observed at optical wavelengths and in HI emission (Arp 1966; Joseph & Wright 1985; Hibbard et al. 2000). There is evidence for a galactic-scale outflow from Hα and soft X-ray observations (Armus et al. 1990; Heckman et al. 1996; McDowell et al. 2003). In the centre, two nuclei are discernible with a separation of ~ 0.4 kpc in the near-infrared (Scoville et al. 1998), millimeter (Scoville et al. 1997; Downes & Solomon 1998; Sakamoto et al. 1999; Downes & Eckart 2007) and radio (Mundell et al. 2001) regimes. There also is a more extended (kpc-scale), rotating gas disk (Downes & Solomon 1998; Sakamoto et al. 1999, 2009; Mundell et al. 2001; Wiedner et al. 2002). Arp 220 is very gas-rich; Scoville et al. (1997) measure a molecular gas mass of $\sim 9 \times 10^9 M_\odot$, concentrated in the central 750 pc – implying an astonishing molecular gas surface density of $5 \times 10^4 M_\odot \, \mathrm{pc}^{-2}$. It therefore comes as no surprise that obscuration is severe for this system; estimates for A_V range from 50 to 1000 (Sturm et al. 1996; Downes & Solomon 1998), and even at near-infrared wavelengths obscuring dust lanes are visible (Scoville et al. 1998). And CO(3-2) and 860 μm continuum observations indicate substantial optical depths even at submillimetre wavelengths (Sakamoto et al. 2008). These extreme levels of extinction have hindered a definitive determination of the power source of Arp 220; a significant contribution to its prodigious luminosity comes from a starburst (Sturm et al. 1996; Lutz et al. 1996, 1998; Genzel et al. 1998b), but there is also significant (and possibly dominant) dust emission from heavily obscured central star formation or perhaps AGN (Spoon et al. 2004). The presence of a deeply dust-enshrouded major nuclear power source is confirmed by millimetre observations; most recently Sakamoto et al. (2008) estimate the bolometric luminosity of the 50–80 pc core within the western nucleus to be at least $2 \times 10^{11} L_\odot$ and possibly as much as $\sim 10^{12} L_\odot$. The high obscuration has prevented confirmation or rejection of a possible active nucleus through X-ray observations (Iwasawa et al. 2001, 2005; Clements et al. 2002); the obscuring column density is of order $N_H \sim 10^{25} \mathrm{cm}^{-2}$ (Iwasawa et al. 2001; Sakamoto et al. 2008). Downes & Eckart (2007) interpret the very compact millimetre continuum emission in the western nucleus as due to a black hole accretion disk, whereas Sakamoto et al. (2008) contend that the morphological agreement between the millimetre continuum emission and supernovae detections is suggestive of a very young, extremely dense starburst being responsible.

Since Arp 220 is the ULIRG most frequently used as a starburst galaxy template, it is vital to understand its power source and star formation history. A photometric analysis by Wilson et al. (2006) of *HST UBVI* observations showed that the central cluster population divides into two groups; one with ages $\lesssim 10$ Myr, and one with

ages $\sim 300\,\mathrm{Myr}$. However, it must be kept in mind that due to photometric uncertainties, the age/reddening degeneracy limits the accuracy of such work. Rodríguez Zaurin et al. (2008) use optical spectroscopic observations of the extended diffuse light along three slit positions for a stellar population analysis; they find the optical spectrum to be dominated by an intermediate-age stellar population (0.5–0.9 Gyr), and a young stellar population ($< 100\,\mathrm{Myr}$) which has an increasing contribution towards the central part of the galaxy. Besides the extinction limitations afflicting all optical-wavelength observations of dusty galaxies, it must be cautioned that only one of their slits covers the central region, from which the vast majority of the luminosity is emitted, and hence that their results may be biased towards the star formation history of the sub-dominant outer regions. Parra et al. (2007) (see also Rovilos et al. 2005; Lonsdale et al. 2006) investigate radio supernovae and supernova remnants in the nuclear region of Arp 22, finding that they are indicative either of a radically different stellar initial mass function, or a very short, intense burst of star formation $\sim 3\,\mathrm{Myr}$ ago.

Here, we use adaptive optics near-infrared integral field spectroscopy data and interferometric mm CO(2-1) and continuum observations, to investigate the star formation history, the extinction, and the nature and orientation of the two nuclei.

In §5.2, we introduce the data, and data analysis procedures. In §5.3 we investigate the star formation history in the SINFONI field of view, and in §5.4 look at the extinction in the near-infrared regime. We then focus on the western (§5.5) and eastern (§5.6) nucleus. We put this together in a coherent picture of the nuclear region (§5.7), before summarising and concluding in §5.8.

5.2 Observations and Data Processing

5.2.1 SINFONI Data

5.2.1.1 Observations and Reduction

Observations of Arp 220 were performed on the nights of March 7th and April 18th to 21st 2007 on Cerro Paranal, Chile, at the Very Large Telescope (VLT) with SINFONI. SINFONI is a near-infrared integral field spectrometer (Eisenhauer et al. 2003) which includes a curvature-based adaptive optics system (Bonnet et al. 2004) and can operate with the VLTs laser guide star facility (Bonacini Calia et al. 2006; Rabien et al. 2004). The laser guide star was used for these observations, without tip-tilt correction due to lack of a suitable tip-tilt star. SINFONI's $0.05'' \times 0.10''$ pixel scale was used, giving a $3.2'' \times 3.2''$ field of view. The science data and standard star observations were reduced using the SPRED software package (Abuter et al. 2006). Telluric correction and flux calibration of the reconstructed data cubes were performed using these standard star frames. Fig. 5.1 shows spectra from three different positions of the Arp 220 nuclear region.
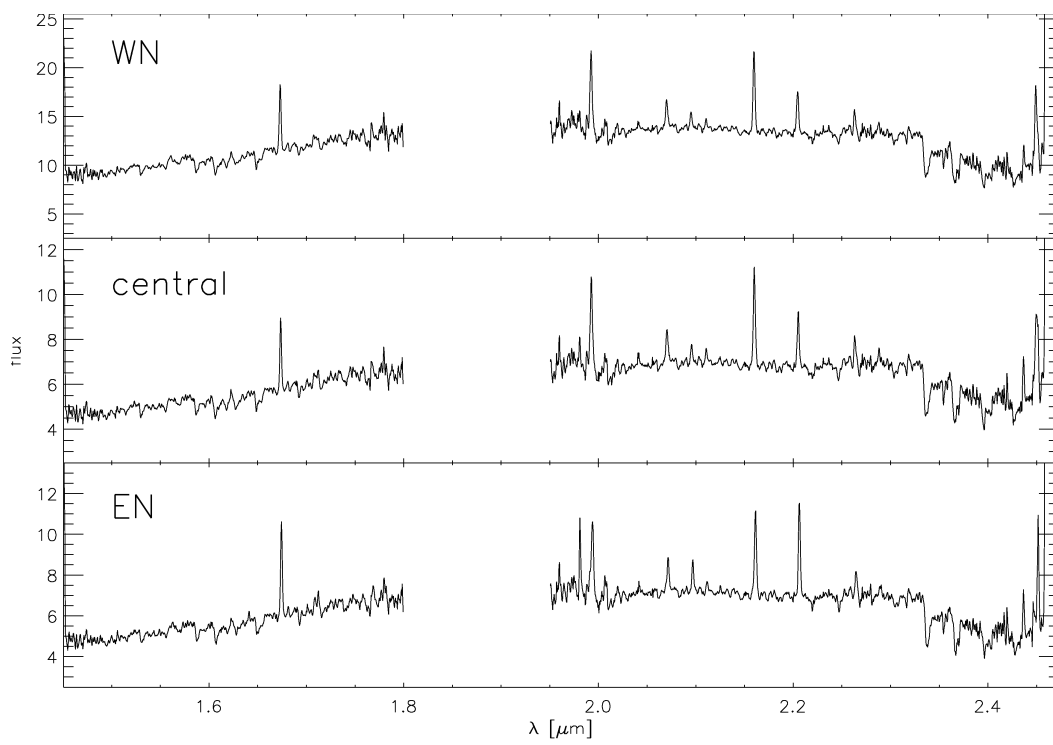
Figure 5.1: Spectra extracted in 0.25″ radius apertures on the western nucleus ('WN'), eastern nucleus ('EN'), and in between the two nuclei ('central').
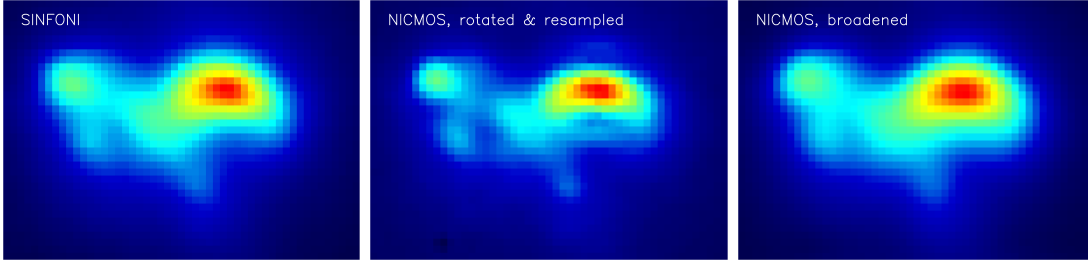
Figure 5.2: We estimate the PSF of our AO data by finding the broadening function which, applied to a higher-resolution image with known PSF, best matches the AO image. The AO PSF is then estimated by convolving this broadening function with the PSF of the high-resolution image. Left: Our SINFONI K-band image. Middle: Archival NICMOS K-band image, rotated and resampled to the SINFONI pixel scale. Right: Best-matching broadened NICMOS image. We find the PSF to be well represented by a slightly asymmetric Gaussian with major axis oriented 4° east of north and FWHM $0.30'' \times 0.31''$.

5.2.1.2 PSF Estimation

We estimate the PSF using the method already explained in §4.2.1.2. Here, we use *HST* NICMOS $2.16\,\mu$m observations retrieved from the *HST* archives as the higher-resolution counterpart with known PSF. Fig. 5.2 shows our SINFONI data, the *HST* data (rotated and resampled to the SINFONI pixel scale), and the broadened *HST* image. We find the PSF to be well represented by an almost perfectly symmetric Gaussian with major axis oriented 4° east of north and FWHM $0.30'' \times 0.31''$– a good performance for laser guide star assisted adaptive optics without a tip-tilt star (Davies 2008b).

5.2.1.3 Spatial binning

In order to achieve a mininum signal-to-noise, we spatially binned each spectral plane of our reduced data cube using an optimal Voronoi tessellation (Cappellari et al. 2003), which bins pixels together into groups by accreting new pixels to each group until a pre-set signal-to-noise-cutoff is reached (cf. §4.2.1.3). The signal-to-noise cutoff was chosen such as not to compromise spatial resolution in the central regions (i.e. such that no binning was performed there), but at the same time extending the region in which meaningful analyses can be performed. As a result of this, the outer regions in e.g. the velocity maps appear in blocks, rather than individual pixels.

5.2.1.4 Extracting Stellar Kinematics

We extract the stellar kinematics using the method explained in §4.2.1.4. The resulting final maps of stellar velocity, dispersion, and EW_{CO} are displayed in Fig. 5.3.
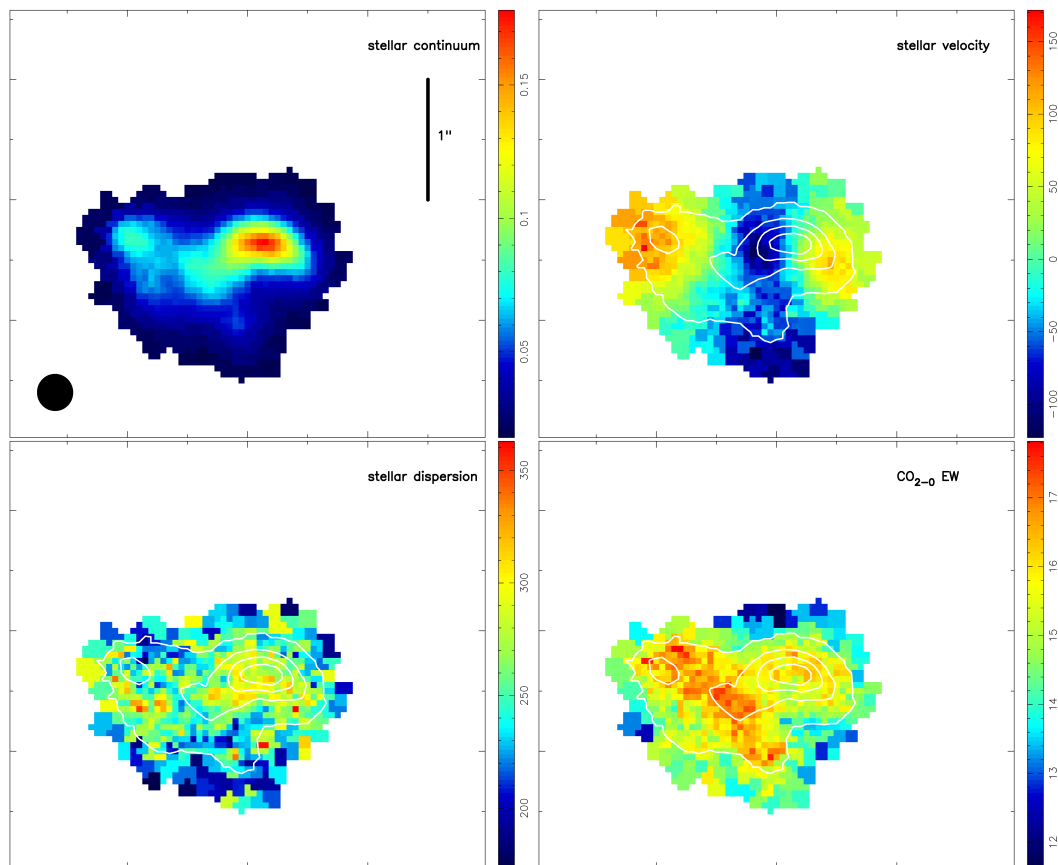
Figure 5.3: Stellar continuum, velocity, velocity dispersion, and EW_{CO} maps. White contours trace the continuum. The bar indicates $1''$, the PSF is displayed in the lower left of panel 1. North is up and east is to the left.

5.2.1.5 H- & K-band Gas Tracers

We derive emission, equivalent width, velocity, and velocity dispersion maps of H_2 1-0S(1) ($\lambda = 2.1218\,\mu$m), HeI ($\lambda = 2.0581\,\mu$m), Paα ($\lambda = 1.8751\,\mu$m), [FeII] ($\lambda = 1.6440\,\mu$m), Brγ ($\lambda = 2.1662\,\mu$m), and Brδ ($\lambda = 1.9445\,\mu$m), by fitting Gaussians to the lineshapes. The results are shown in Fig. 5.4.

5.2.2 Plateau de Bure Interferometer Data

We also analyse ^{12}CO(J = 2-1) line emission and 1.3 mm dust continumm emission observations from the IRAM millimetre interferometer, located on the Plateau de Bure, France, at an altitude of 2550 m (Guilloteau et al. 1992). These observations were first analysed and published by Downes & Eckart (2007), and we refer the reader to this publication for the technical details. These authors find evidence for hot dust emission from an AGN accretion disk in the western nucleus, the best evidence for a black hole in the central region of Arp 220 to date. Since the absolute astrometry between the PdBI and the SINFONI datasets is not precise, we anchor the SINFONI and PdBI data with respect to each other by assuming that the flux peaks of the western nucleus are coincident. This assumption is justified by the fact that in the western nucleus, all the K-band tracers coincide at the same location (unlike in the eastern nucleus), and hence it is to be expected that the cold gas emission also peaks at the same position. We derive a velocity map by fitting Gaussians to the line shapes, the result is displayed in Fig. 5.5.

5.3 Star Formation History & Stellar Populations

In this Section, we investigate the star formation history, and the composition of the stellar population, using observables and the stellar synthesis code STARS (Sternberg 1998; Sternberg et al. 2003; Förster Schreiber et al. 2003; Davies et al. 2003, 2005, 2006, 2007). In the following, we use spatially averaged measurements to investigate the composition of the stellar population. Since we are summing over a large spatial area, we can be sure to cover a large number of individual star clusters (which may have started forming stars at slightly different times), and hence to be probing the average star formation properties.

5.3.1 A 10 Myr old Starburst...

Our primary diagnostics are the EW_{CO} and the Brγ flux and EW. The EW_{CO} map is shown in the last panel of Fig. 5.3, the Brγ maps are displayed in Fig. 5.6. In Fig. 5.7, we show the evolution of EW_{CO}, $EW_{Br\gamma}$, and L_{bol}/L_K for a number of starbursts with different decay timescales. We observe EW_{CO} to be $\gtrsim 14\,\text{Å}$ everywhere,
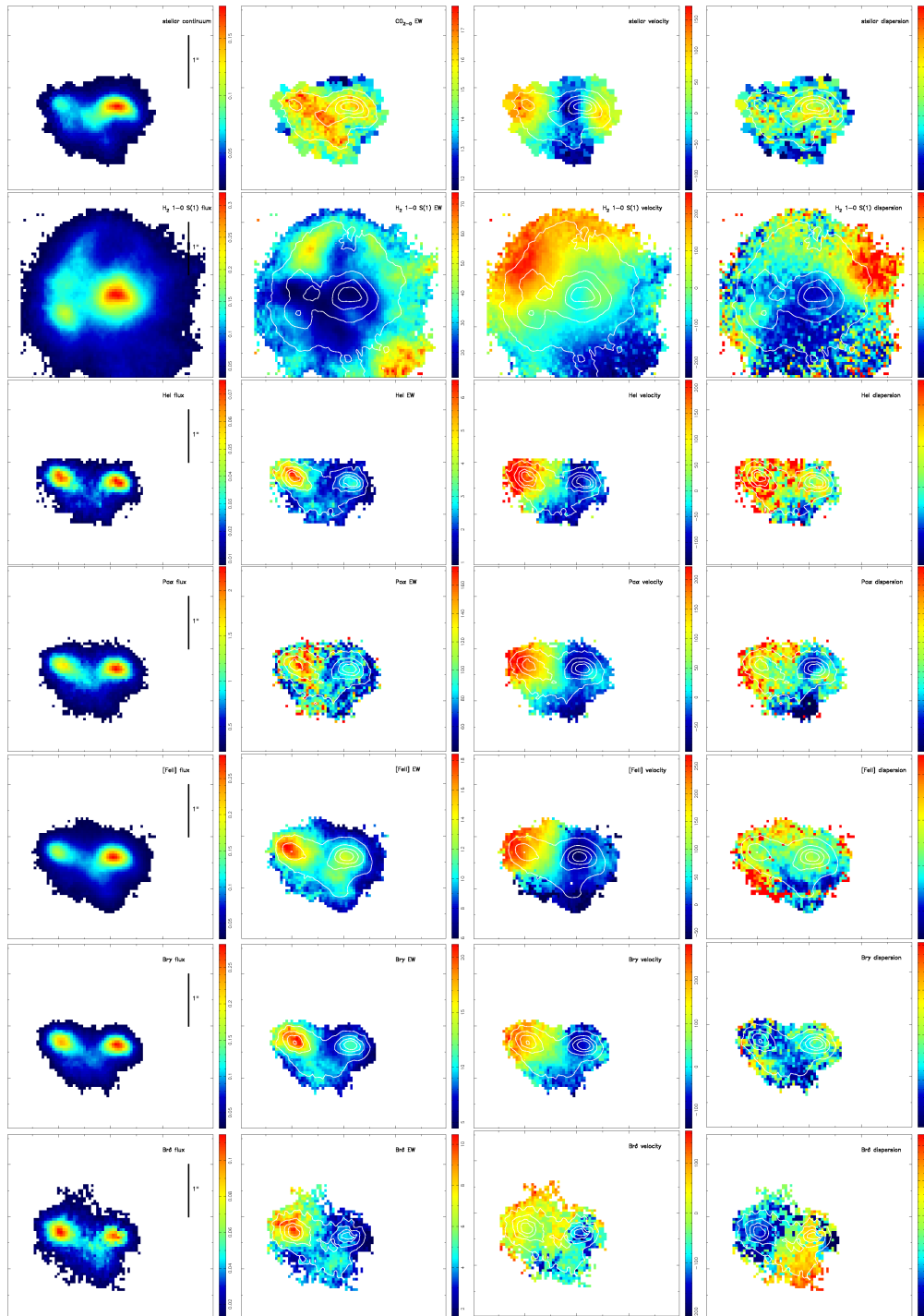
Figure 5.4: Flux, equivalent width, velocity, and velocity dispersion maps for a number of H- and K-band tracers (cf. §5.2.1.5).
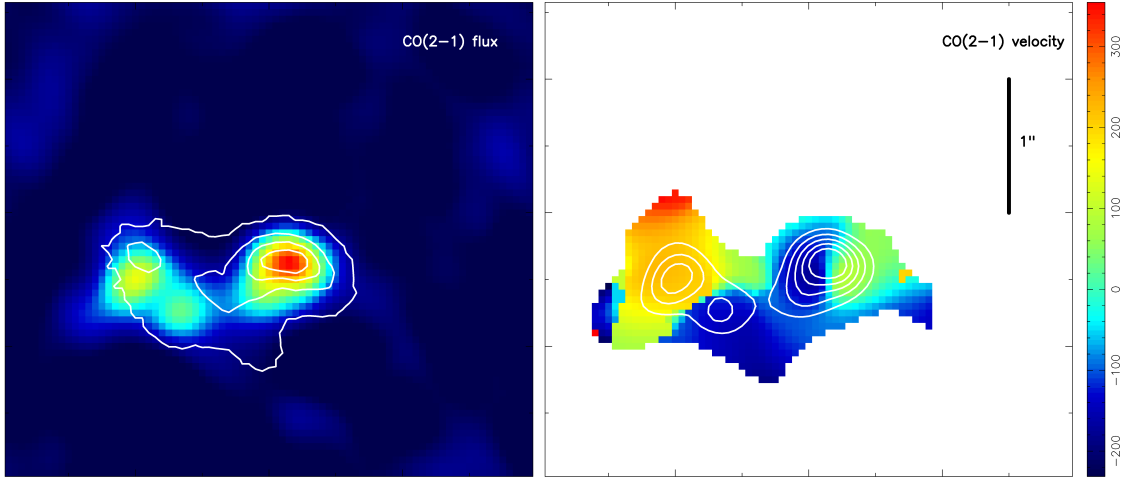
Figure 5.5: CO(2-1) flux (left, with contours showing the K-band continuum), and velocity map (right, contours tracing the CO(2-1) flux). The bar indicates $1''$. North is up and east is to the left.

and $\gtrsim 16\,\text{Å}$ on the nuclei; as can be seen from Fig. 5.7, only an instantaneously decaying ('delta'-) starburst $10\pm2\,\text{Myr}$ old can produce such large values of EW_{CO}. We begin by estimating the luminosity contribution of any stars not belonging to this 10 Myr old starburst population, by noting that the theoretically possible upper limit to EW_{CO} is $17\,\text{Å}$. This allows us to calculate the luminosity contribution from a stellar population with smaller EW_{CO} that may be diluting it. We note that this is strictly speaking only an upper limit, since we do not know the intrinsic EW_{CO} of the starburst population. However, this intrinsic value likely is quite close to $17\,\text{Å}$, since this is what is measured in between the two nuclei, where the dilution from any putative older stellar population associated with the nuclei would be minimal. Hence our 'upper limit' to the non-starburst luminosity is in fact more likely to be a reasonable estimate.

5.3.2   ... & 1) a younger stellar population?

Both the presence of radio supernovae (Parra et al. 2007) and our Brγ maps clearly indicate the presence of young stars – only very young ($\lesssim 8\,\text{Myr}$) stars are hot enough to excite hydrogen sufficiently to emit Brγ flux. We thus first investigate the possibility that a population of stars younger than 10 Myr may be diluting the CO bandheads of the 10 Myr starburst population; these stars would have $\text{EW}_{CO}=0\,\text{Å}$ (Fig. 5.7). In this case, the younger stars would contribute $\sim 10\%$ of the K-band luminosity. Below (§5.4), we calculate that if the assumption of younger ($<10\,\text{Myr}$) stars diluting the CO bandheads is correct, then we are only seeing $\approx 20\%$ of the actually emitted (no reddening-correction) K-band luminosity. For a 10 Myr old in-

stantaneously decaying starburst, STARS predicts a K-band mass-to-light ratio of $\approx 0.2\,M_\odot/L_\odot$ (Fig. 5.7). Correcting the measured K-band luminosity for the western nucleus for the missing light, and using our dynamical mass estimate (§5.5.3, corrected for a 10% gas fraction), the non-starburst stellar population of the western nucleus must have $M/L_K \sim 75\,M_\odot/L_\odot$. The same calculation for the eastern nucleus yields an even larger $M/L_K \sim 99\,M_\odot/L_\odot$. The expected M/L_K for stars $\lesssim 10\,Myr$ old is $\lesssim 0.1\,M_\odot/L_\odot$ – a divergence of three orders of magnitude. We therefore reject the assumption of a younger stellar population diluting the bandheads of the 10 Myr old starburst population.

5.3.3   ... & 2) an older stellar population!

Stars older than $\sim 20\,Myr$ have an $EW_{CO} \approx 12\,Å$; a fractional luminosity contribution of 26-44% would be required to achieve the bandhead dilution (Table 5.1 lists the results for both the western nucleus and the entire nuclear region). In this case, we are only seeing $\approx 7\%$ of the actually emitted K-band luminosity (§5.4), and the non-starburst stellar population of the western nucleus must have $M/L_K \approx 7.4\,M_\odot/L_\odot$ – which is what is expected for a several Gyr old stellar population. The same is found for the eastern nucleus, here an $M/L_K \approx 9.8\,M_\odot/L_\odot$ is required. We therefore conclude that the assumption of a significantly ($\gtrsim 1\,Gyr$) older stellar population alongside the 10 Myr old starburst in the central kpcs of Arp 220 is correct. We note that we still require a third population of stars younger than $\sim 7\,Myr$ (which would have $EW_{Br\gamma} \sim 600\,Å$, Fig. 5.7), to account for the Brγ emission. However, their luminosity contribution would be minimal; their intrinsic $EW_{Br\gamma} \sim 600\,Å$ has to be diluted by a factor $\gtrsim 75$ to reach the measured $EW_{Br\gamma} \lesssim 8\,Å$).

This is in good agreement with what Rodríguez Zaurin et al. (2008) find based on optical spectroscopy of the central region of Arp 220; namely near-equal contributions from a $\leq 0.1\,Gyr$ and a 0.5-0.9 Gyr old stellar population. Wilson et al. (2006) derive photometric age estimates of clusters from *HST UBVI* data and find two age classes; $\lesssim 10\,Myr$ and 70-500 Myr.
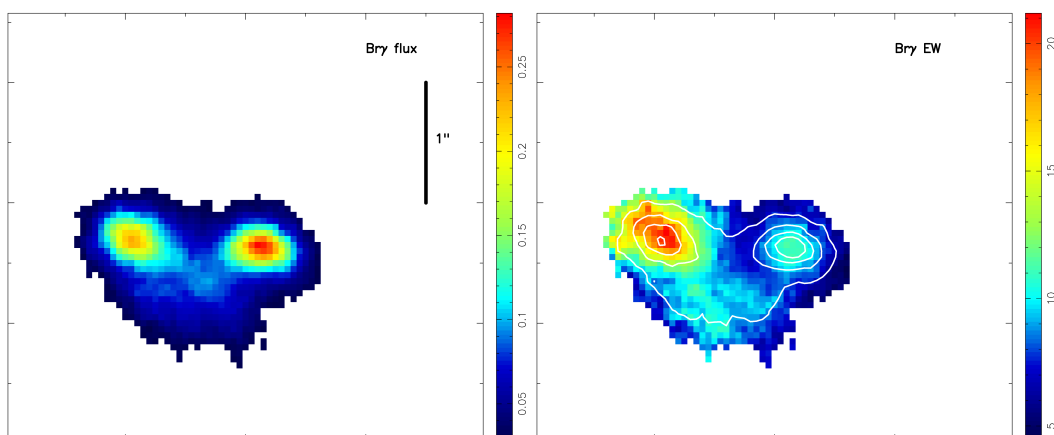
Figure 5.6: Brγ flux (left) and EW (right). Contours trace Brγ flux. The bar indicates 1″. North is up and east is to the left.

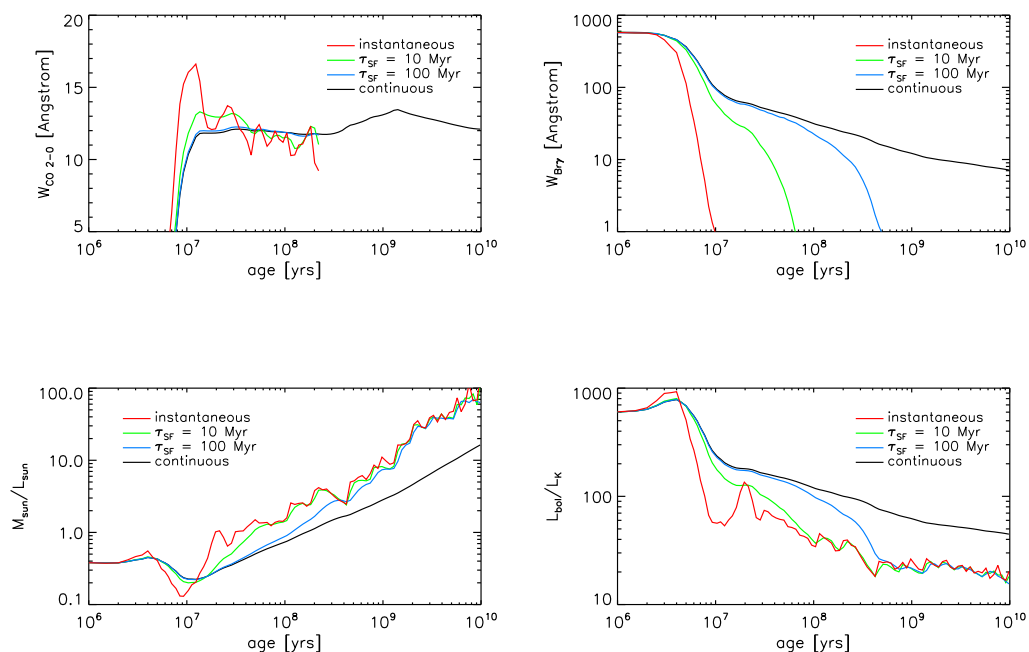**Figure 5.7:** Evolution of EW_{CO}, $EW_{Br\gamma}$, L_{bol}/L_K, and M/L_K, computed with STARS, for an instantaneously decaying starburst (red), starbursts with decay timescale 10 Myr (green) and 100 Myr (blue), and continuous star formation (black). As can be seen, only a ∼ 10 Myr old 'delta'-starburst can produce $EW_{CO} \gtrsim 14$ Å.

	L_K^{a}	$\mathrm{EW}_{CO}^{\mathrm{a}}$	$\mathrm{EW}_{Br\gamma}^{\mathrm{a}}$	$L_{K,non-SB}/L_K^{\mathrm{b}}$	L_{bol}/L_K^{b}	$L_{K,non-SB}/L_K^{\mathrm{c}}$	L_{bol}/L_K^{c}
SINFONI FoV	$3.25{\times}10^9 L_\odot$	14.78Å	7.09Å	0.13	151±25	0.44	49±9
western nucleus	$9.5{\times}10^8 L_\odot$	15.72Å	8.69Å	0.08	111±12	0.26	51±5

[a] measured

[b] assuming the non-starburst population to be $\lesssim 8\,\mathrm{Myr}$ old with $\mathrm{EW}_{CO}{=}\,0\,\text{Å}$

[c] assuming the non-starburst population to be $\gtrsim 20\,\mathrm{Myr}$ old with $\mathrm{EW}_{CO}{=}\,12\,\text{Å}$

Table 5.1: Stellar population analysis. We assume the starburst population to have $\mathrm{EW}_{CO}{=}\,17\,\text{Å}$, as measured between the two nuclei, and calculate the luminosity contribution of a younger ($\mathrm{EW}_{CO}{=}\,0\,\text{Å}$) or older ($\mathrm{EW}_{CO}{=}\,12\,\text{Å}$) stellar population required to dilute the CO absorption bandheads to the measured values. We furthermore calculate the expected L_{bol}/L_K for each case. The $\mathrm{EW}_{Br\gamma}$ furthermore indicates the presence of a very young ($\lesssim 7\,\mathrm{Myr}$) stellar population, the luminosity contribution of which however, at less than a few percent of the total, is negligible.

5.4 Reddening & Extinction

5.4.1 Reddening

Like most ULIRGs, Arp 220 contains significant amounts of dust. In the K-band, the effect of this is mostly a wavelength-dependend extinction due to scattering and absorption, with longer-wavelength radiation being less severely affected. The effect of this is 'reddening', a steepening of the continuum level towards longer wavelengths. Another effect pertaining to the presence of dust is the re-emission of dust-absorbed stellar light. However in the H- and K-band this would only be observable if very hot dust were present. Since any continuum emission due to hot dust would lead to dilution of the CO absorption bandheads, and since we are seeing absorption depths very near the theoretically possible maximum of $\sim 17\,\text{Å}$, we can exclude the possibility of any significant hot dust emission.

When accounting for the obscuring effects of dust, the dust is most commonly assumed to either be spatially uniformly mixed with the stars ('mixed model'), or to form a screen between the observed stars and the observer. Or one can use the empirically derived reddening law of Calzetti et al. (2000). In cases of strong obscuration, the mixed model may be insufficient to account for the reddening, since it saturates beyond a certain level of extinction. In order to determine which method is appropriate for Arp 220, we obtained archival *HST* images spanning a wavelength range of 0.45-$2.12\,\mu$m, and extracted photometric data points at a number of locations using $0.15''$ radius apertures. We then reddened a synthetic stellar population spectrum (corresponding to the star formation history determined in §5.3), using each reddening prescription outlined above, until it fit those data points. The results can be seen in Fig. 5.8 – as expected, the mixed model was insufficient to account for the strong extinction of Arp 220. The screen model results in a decent match, but the Calzetti et al. (2000) reddening law clearly produces the best results. We note that in Chapter 4 we arrive at the same conclusion for NGC 6240. Here, the screen extinction law also yields a somewhat lower F_{obs}/F_{em} than the Calzetti et al. (2000) reddening law.

In order to quantify the reddening in Arp 220, we fitted a stellar template to the line-free continuum, using the Calzetti et al. (2000) reddening law. In Fig. 5.9, we show the resulting map of F_{obs}/F_{em} at $2.12\,\mu$m, and of the corresponding optical extinction A_V; obtained by calculating F_{obs}/F_{em} at $0.55\,\mu$m and converting to extinction via $A_V = -2.5\log(F_{obs}/F_{em})$.

We also derived the reddening using molecular hydrogen emission lines. For case B recombination at $T = 10{,}000\,$K and $n_e = 10^4\,\text{cm}^{-3}$, the line flux ratio of Paα and Brγ is 12.2; by comparing this to the actually observed line ratio, the relative reddening can be deduced. Again using the Calzetti et al. (2000) reddening law, we thus measured F_{obs}/F_{em} and derived A_V, both shown in Fig. 5.10. As can be seen, the two extinction measurements agree well both in regard to strength and spatial variation
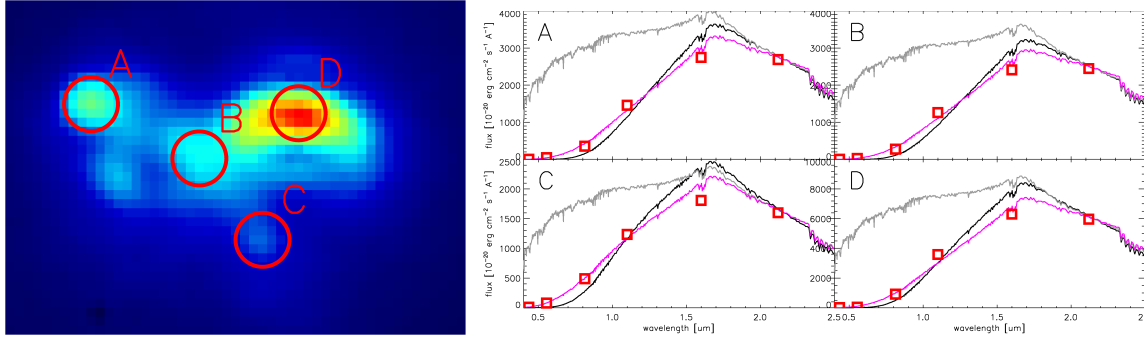
Figure 5.8: Comparison of different extinction models: We fitted a synthesised stellar population spectrum to *HST* photometric data points extracted in 0.15″ radius apertures in a range of locations across our field of view (4 examples shown), by reddening the synthetic SED until it matched the data. Grey: mixed extinction, black: screen extinction, magenta: Calzetti et al. (2000) reddening law. As can be seen, the Calzetti et al. (2000) reddening law produces the best fit to the data.

of the extinction. The 1.3 mm continuum map of Downes & Eckart (2007) could give us valuable information about the spatial distribution of the obscuring dust, however unfortunately only two barely resolved point sources are detected at their sensitivity level. Downes & Eckart (2007) estimate the optical depth for the western nucleus to be $\tau_{WN}(1.3\,\mathrm{mm}) \geq 0.7$; adopting their assumptions also for the eastern nucleus, we estimate $\tau_{EN}(1.3\,\mathrm{mm}) = 0.15$–$0.33$; this is by extension also an upper limit of the off-nuclear $\tau(1.3\,\mathrm{mm})$.

5.4.2 Extinction

The significant reddening quantified in §5.4.1 is indicative of a substantial amount of stellar light emitted in the near-infrared in the central region of Arp 220 which is completely absorbed, and re-emitted at longer wavelengths. Here, we attempt to quantify the amount of 'missing light' in the K-band, by comparing the infrared luminosity, calculated from *IRAS* flux measurements, to the stellar bolometric luminosity calculated from our measured L_K and the L_{bol}/L_K expected from our stellar population analysis (§5.3 & Table 5.1). We use the Sanders et al. (2003) *IRAS* fluxes from the Revised Bright Galaxy Sample, and calculate the infrared flux via $F_{IR,8-1000\mu m} = 1.8 \times 10^{-14} \times (13.48 \times f_{12} + 5.16 \times f_{25} + 2.58 \times f_{60} + f_{100})\,\mathrm{W\,m^{-2}}$, with f_{12} the IRAS flux density in Jy at 12 μm etc (Sanders & Mirabel 1996). We then convert this to infrared luminosity, $L_{IR} = 3.127\mathrm{e}7\,D^2\,F_{IR}\,L_\odot$ (D in pc). This yields $L_{IR,8-1000\mu m} = 1.37\mathrm{e}12\,L_\odot$. Nardini et al. (2010) perform a 5–8 μm spectral analysis of Arp 220 using the Infrared Spectrograph onboard *Spitzer*; they find a 17% AGN contribution to the bolometric luminosity of Arp 220, which we need to correct for in order to find the stellar bolometric luminosity. However, this is largely
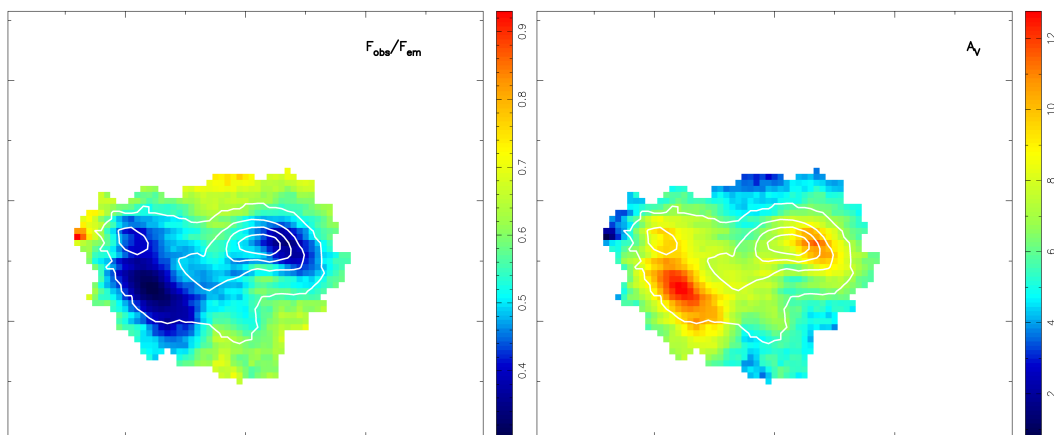
Figure 5.9: Left: F_{obs}/F_{em} in the K-band, derived by fitting a stellar template to the line-free continuum using the Calzetti et al. (2000) reddening law. Right: corresponding optical extinction A_V. Contours trace the continuum.
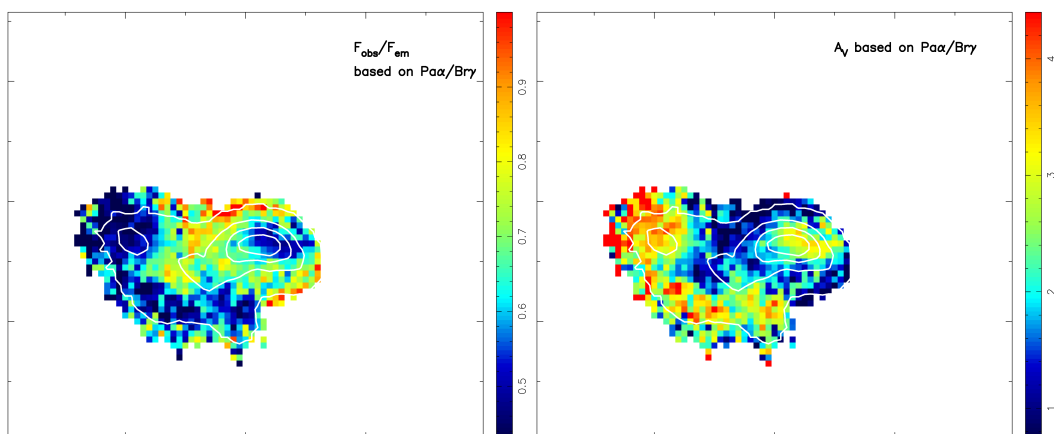

Figure 5.10: Left: F_{obs}/F_{em} in the K-band, derived by comparing the observed flux ratio of Paα and Brγ to the theoretically expected value, again using the Calzetti et al. (2000) reddening law. Right: corresponding optical extinction A_V. Contours trace the continuum.

offset by the translation of infrared to bolometric luminosity, which for ULIRGs is typically $L_{bol} = 1.15 \times L_{IR}$ (Kim & Sanders 1998). This yields a total stellar bolometric luminosity of $1.31 \times 10^{12} L_\odot$. We then measure the K-band luminosity of Arp 220 using the archival *HST* NICMOS images already utilised in §5.2.1.2, finding $L_K = (1.75 \pm 0.1) \times 10^9 L_\odot$ (for comparison, our SINFONI data yield $L_K = (1.34 \pm 0.07) \times 10^9 L_\odot$ for the SINFONI FoV, implying that $\sim 80\%$ of the total L_K are emitted in the nuclear region – cf. Wynn-Williams & Becklin 1993). This results in a L_{bol}/L_K of ~ 750, whereas our earlier stellar population analysis (§5.3) requires ~ 150 (theoretically expected for 10 Myr old starburst plus younger stellar population with the derived relative luminosity contributions; cf. Table 5.1) or ~ 50 (10 Myr old starburst plus older stellar population) – implying that in the K-band we are missing a factor of ~ 5 or ~ 15 of light, respectively. As we show in §5.3, the assumption of a population younger than 10 Myr is inconsistent with our dynamical mass estimate, and we can therefore exclude this alternative. We thus conclude that in the K-band, we are only observing $\sim 7\%$ of the actually emitted (no reddening-correction) stellar light. This is consistent with Rodríguez Zaurin et al. (2008), who find that the bolometric luminosity derived from optical wavelength observations is an order of magnitude smaller than the mid- to far-infrared luminosity, and are led to conclude that 'most of the on-going star formation in the nuclear region is hidden by dust'. Further support for our result is lend by the supernova rate estimates of Rovilos et al. (2005); these authors derive $SNR \sim 0.7 \, yr^{-1}$ for the western nucleus. STARS predicts a supernova rate of $10^{10}/L_K \, yr^{-1}$ for a 10 Myr old instantaneous starburst, which for our corrected K-band luminosity, of which $\sim 75\%$ are attributed to the 10 Myr old starburst, implies a supernova rate $\approx 1.0 \, yr^{-1}$.

5.5 Western Nucleus

5.5.1 Stellar & CO(2-1) Kinematics

As Fig. 5.3 shows, the stellar kinematics exhibit a clear rotational signatures around the western nucleus. In order to extract a rotation curve and find the kinematic centre of the stellar rotation, we fit an inclined disk model to the velocity map (Fig. 5.11). The best-fitting model has an inclination q = 62±6, and a position axis (PA hereafter) of -9.8±0.4deg south of east, with average residuals of $12.2 \, km \, s^{-1}$. We also derive a dispersion profile by azimuthally averaging the 2D dispersion map. We note that we do not suggest that the stars in the western nucleus are moving in a thin disk – we simply parameterise the rotation field in terms of circular orbits with a fixed centre, PA, and inclination, in order to derive a rotation curve and kinematic centre.

The CO(2-1) also displays a regular rotation pattern around the western nucleus, which we model analogous to the stellar velocity analysis. The best-fitting model (Fig. 5.12) indicates an inclination q ≈ 0.56 and PA ≈ -3deg south of east, with the kinematic centre coincident with that of the stellar velocity field within the uncertain-
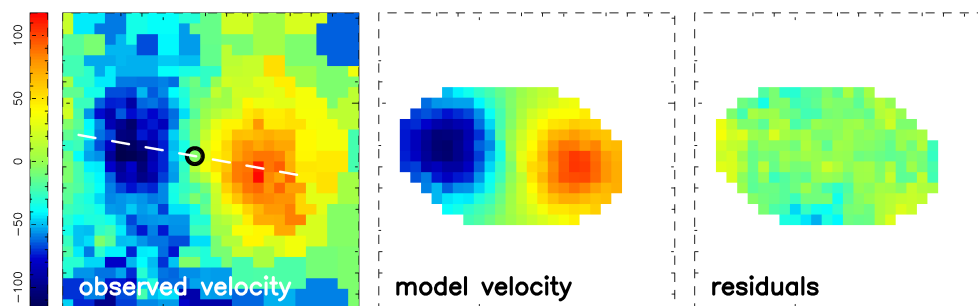
Figure 5.11: Western Nucleus: Velocity field, best-fitting disk model, and residuals. The kinematic centre is marked by a black circle, and the major axis is indicated with a white dashed line. 1 pixel corresponds to $0.05''$.

Figure 5.12: Western Nucleus: CO(2-1) velocity field, best-fitting disk model, and residuals. The kinematic centre is marked by a black circle, and the major axis is indicated with a white dashed line. 1 pixel corresponds to $0.05''$.
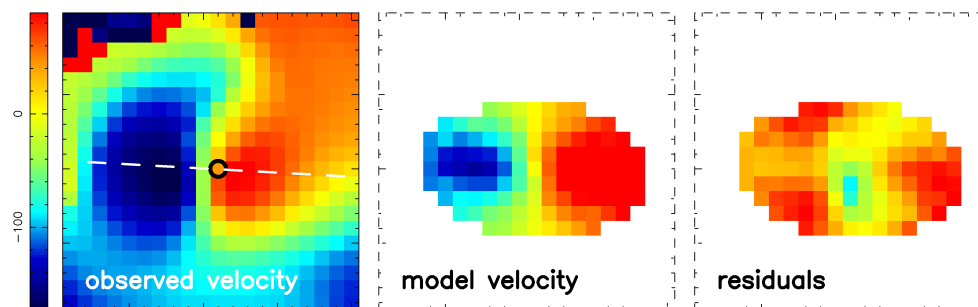
ties. The stellar and CO(2-1) kinematics in the western nucleus thus seem to agree well.

5.5.2 Kinematic Centre & Hot Dust Emission

Downes & Eckart (2007) detect emission from a hot, compact dust ring just south of the CO(2-1) emission peak of the western nucleus, which they interpret as being heated by an AGN accretion disk. We locate the position of the continuum emission using the relative position of the dust emission peak and the CO(2-1) emission, and assuming that the peak of the stellar continuum in the western nucleus is coincident with that of the CO(2-1) emission (as outlined in §5.2.2). Intriguingly, the putative AGN position thus derived is coincident with the kinematic centre of the stellar and CO(2-1) rotation found in §5.5.1. This strongly suggests that the stars in the western nucleus are moving in a gravitational potential with either a supermassive black hole (Downes & Eckart 2007) or an extremely dense, young starburst (Sakamoto et al.

2008) at its centre.

5.5.3   Dynamical Mass Estimate

In principle, our data are of high enough quality to derive the dynamical mass via Jeans modelling. However, as we found in §5.4, Arp 220 is severely affected by extinction in the K-band. Since we do not know the relative three-dimensional distribution of the obscuring material, it is impossible to derive the intrinsic kinematics from the observed two-dimensional line of sight projections. We therefore have to content ourselves with a simpler estimate of the dynamical mass. We adopt the approach taken by Bender et al. (1992), which is based on the tensor virial theorem (Binney & Tremaine 1987), and refer the reader to appendix B of Bender et al. (1992) for a detailed discussion. According to this, the appropriate dynamical mass formula for the relative stellar velocities and dispersions of the western nucleus is $M_{dyn} = 1.12 \times 3 \times \sigma_0^2 \times R/G$. Using the rotation and dispersion profiles derived in §5.5.1, this yields an enclosed dynamical mass out to $\sim 100\,\mathrm{pc}$ (180 pc) of $6.3 \times 10^9 M_\odot$ ($9.0 \times 10^9 M_\odot$).

Downes & Solomon (1998) estimate a gas mass for the western nucleus of $6 \times 10^8 M_\odot$, based on 1.3 mm dust emission, implying a gas fraction of $\sim 10\%$, wich agrees well with what is expected for ULIRGs and starburst galaxies (Hicks et al. 2009 and references therein).

5.6   Eastern Nucleus

5.6.1   Stellar & Gas Kinematics

The stellar kinematics of the eastern nucleus are more difficult to interpret; although a strong velocity gradient is clearly present, pinning down a rotational major axis is much less obvious. The CO(2-1) kinematics are even more intriguing; the velocity map appears as a step-function, with the velocity changing abruptly from -135 to $+205\,\mathrm{km\,s^{-1}}$. In order to investigate this, and any differences to the western nucleus, we produced P-V diagrams across each nucleus, also mapping the 1.3 mm continuum emission. As can be seen (Fig. 5.13), the P-V diagram of the western nucleus is fairly typical of a rotating disk or spheroid, with only a slight flux gap in velocity-space near the centre of rotation. The eastern nucleus however appears markedly different, with a gap of almost $200\,\mathrm{km\,s^{-1}}$ between the two emission regions. To understand this, we construct a model of the eastern nucleus, using the simple *ansatz* that we are seeing two unresolved sources at different velocities (we note that at this stage we do not make any assumptions about the actual gas distribution, only the actually observed emission). After convolving a model data cube with the PSF of the CO observations, we extract a flux map and P-V diagram and compare it to the data. As Fig. 5.14 shows, the match achieved is striking – supporting our hypothesis that we are indeed seeing two compact, unresolved emission sources. Moreover, as Fig. 5.13

shows, the peak of the continuum emission lies at the centre of rotation, and hence the gravitational potential. We constrain the mass enclosed, by assuming that the two sources are on circular orbits, and calculating the enclosed mass for a range of inclinations of the rotation plane. Excluding the most extreme inclinations ($q < 0.25$ & $q > 0.9$), we derive a dynamical mass of $1.8 \pm 0.5 \times 10^9 M_\odot$ within $0.22''$, or $81\,\mathrm{pc}$. Downes & Eckart (2007) present evidence for an AGN in the western nucleus; it is tempting to speculate that in fact both nuclei of Arp 220 are host to a supermassive black hole, akin to NGC 6240 – this dynamical mass can be regarded as an upper limit on the mass of a putative black hole in Arp 220's eastern nucleus.

This appears strongly suggestive of a gas disk or ring orbiting the centre of the continuum emission. However, one might wonder why in this case we are not seeing any CO(2-1) emission from the centre. Sakamoto et al. (2009) find the CO(3-2) emission lines from the nuclei to be indicative of rotation, and the $^+$HCO emission to display P-Cygni profiles. They furthermore detect the signature of blueshifted mm continuum emission. This, as they elaborate, is indicative of gas in rotational motion and outflowing absorbing gas away from the continuum peak towards the observer. The most plausible explanation for the observations is therefore a rotating gas mass centered on the mm-continuum emission, with the lack of CO line emission from the nuclear core due to self-absorption by outflowing gas along the line of sight.

5.6.2 Dynamical Mass Estimate

The stellar kinematics of the eastern nucleus do not allow a straightforward measurement of a rotation major axis, we therefore instead use the kinematic centre and PA of the CO(2-1) velocity field (Fig. 5.5) to measure the stellar rotational velocity and dispersion at a radius of $\sim 230\,\mathrm{pc}$ ($100\,\mathrm{pc}$). Analogous to §5.5.3, this yields an enclosed mass of $11.2 \times 10^9 M_\odot$ ($5.8 \times 10^9 M_\odot$). Downes & Solomon (1998) estimate a gas mass of $1.1 \times 10^9 M_\odot$ for the eastern nucleus, again implying a gas fraction of $\sim 10\%$.

5.6.3 Nature of Eastern Nucleus

Different tracers display different morphologies at the eastern nucleus; raising the question whether we are seeing a kinematically coherent structure, or something different (a gas streamer, e.g.). The 2D velocity fields of the CO(2-1) and various K-band tracers all appear broadly similar, suggesting that they are all governed by the same gravitational potential. One way to look at this is to directly compare the velocities of the different tracers. Fig. 5.15 plots the velocity of the emission peak of a number of tracers along the CO(2-1) rotation major axis; as can be seen, the velocity differential is largest for CO(2-1), followed by the K-band gas tracers, and somewhat smaller still for the stars. Since the 2D velocity fields of these all appear qualitatively broadly similar, these differences are most likely due to the different depths probed
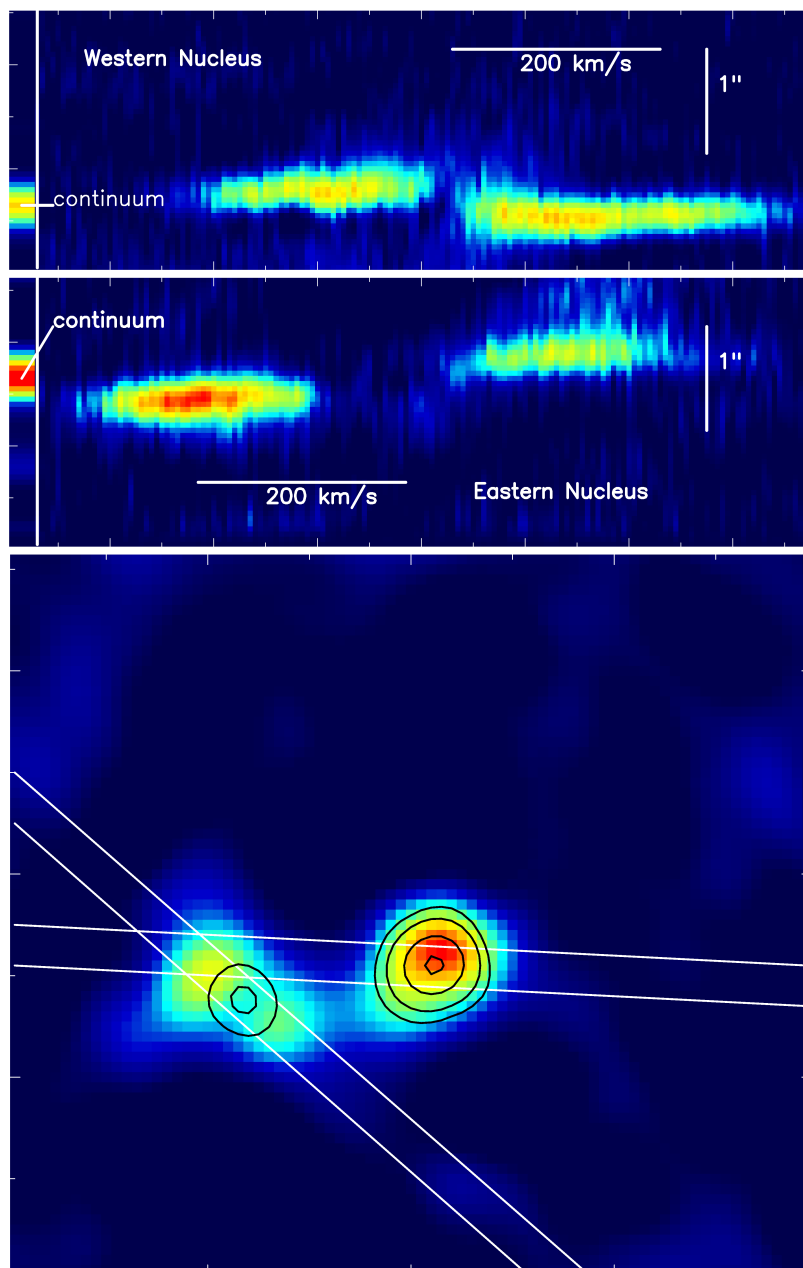
Figure 5.13: Position-Velocity diagrams across the western and eastern nucleus. The bottom figure shows a CO(2-1) flux map indicating the position of the slits, with 1.3 mm continuum emission overlaid in contours. Above are the P-V diagrams for western (top) and eastern (bottom) nucleus. As can be seen, there is no line emission in the central region of the eastern nucleus, coincident with the peak in dust emission.
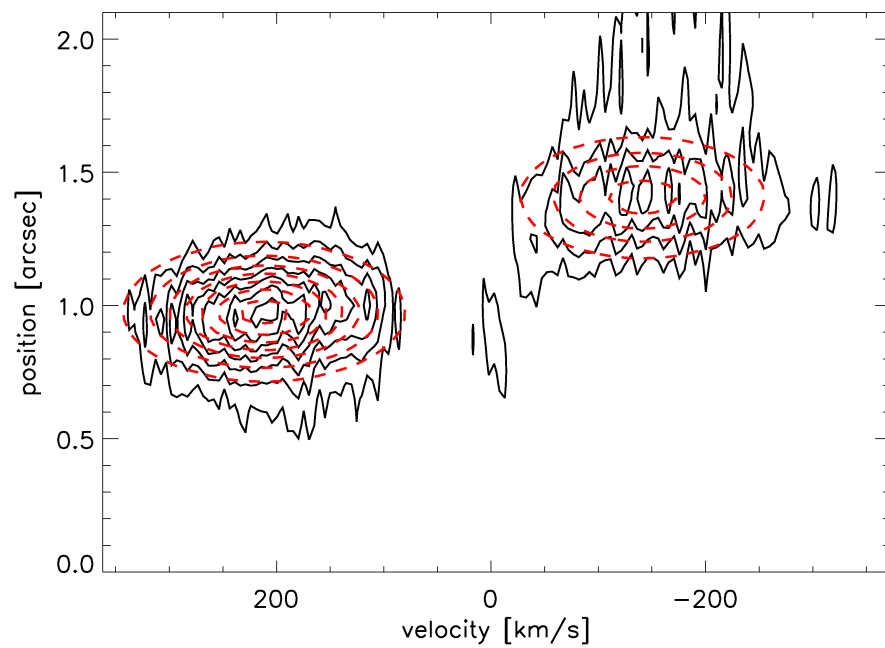
Figure 5.14: Position-Velocity diagram across the eastern nucleus (solid black contours) and from model (dashed red contours). Both sets of contours are displaying the same flux levels. As can be seen, the model (two unresolved point sources orbiting the continuum emission peak) provides an excellent fit to the data.

by the CO(2-1) and the K-band tracers, rather than inherently different 3D velocity structures. The slightly smaller stellar velocities are expected, since rotating gas quickly collapses to a disk, whereas the stars are likely in a more spheroidal distribution, and hence have a larger fraction of their kinetic energy locked up in dispersion, rather than rotation. We therefore conclude that the eastern nucleus, like the western nucleus, is a kinematically coherent structure. This, in conjunction with our stellar population analysis (§5.3), leads to the obvious conclusion that most likely the nuclei are (remnants of) the progenitor galaxies' bulges.

Since mm-wavelength CO(2-1) observations are significantly less affected by extinction than K-band tracers, and given that our analysis above clearly shows that our CO(2-1) observations are probing deeply into the eastern nucleus, we can use these to assess the depth to which our K-band tracers are probing. We do this by utilising our model from §5.6.1 again, and making the simplifying assumption that the gas and stars we are observing in the K-band are also moving in a (thick) disk structure in the same gravitational potential as the cold gas. From this starting assumption, we then calculate at what distance above the disk midplane the different K-band emitters must be rotating to have velocities as observed. We find that generally they are 0.5–1 times as high above the disk midplane as their radial distance from the rotation axis – implying that we are only probing the outer regions of the eastern nucleus in the K-band, in agreement with the large extinction we found earlier (§5.4).

Fig. 5.16 shows the extinction map, with the emission peaks of the various tracers, and the regions of high $\mathrm{EW}_{Br\gamma}$ ($> 16\,\text{Å}$, black) and EW_{CO} ($> 16\,\text{Å}$, white) which indicate regions with large flux contributions from recent star formation. As can be seen, both the region with lots of recent star formation and the region with high extinction are elongated along the major axis of the CO(2-1) rotation, but offset from each other, with one either side of the major axis. This suggests that we are seeing a thick disk/spheroid embedded in the larger scale gas disk, with the northwestern half in front, and the southeastern half behind the gas disk; leading to the offset regions of high extinction (lower half of nucleus obscured by gas disk) and high star formation (nucleus above disk plane). We have indicated the suggested outline of the nucleus in Fig. 5.16. We note that this is supported by Fig. 8 of Sakamoto et al. (2008), which shows the location of the radio supernovae/supernova remnants (Parra et al. 2007) in relation to the $860\,\mu\text{m}$ continuum emission.

5.7   Nuclei & Large-Scale Gas Disk

As Scoville et al. (1997); Downes & Solomon (1998); Mundell et al. (2001) show, the two nuclei are embedded in a larger-scale gas disk, with an estimated gas mass of $\sim 3 \times 10^9 M_\odot$ (Downes & Solomon 1998). Our observations are consistent with this; the H_2 kinematics clearly show rotational motion across the full SINFONI field of view (Fig. 5.4).
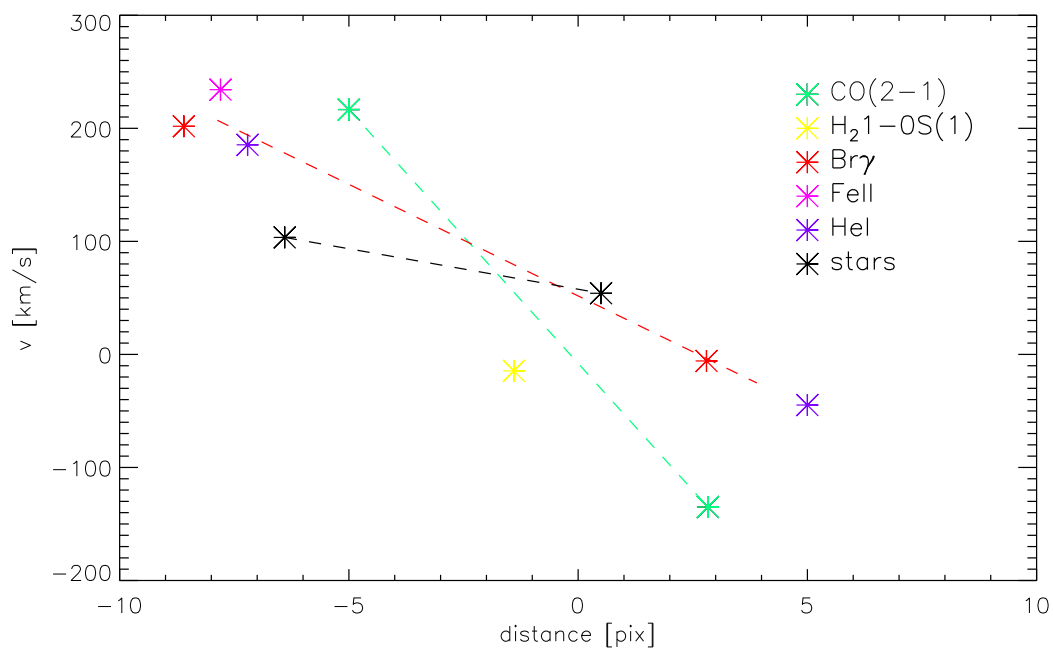
Figure 5.15: Emission peak positions (stars) and velocities of CO(2-1) and various K-band tracers in the eastern nucleus, along the CO(2-1) rotation major axis. The data points are connected by dashed lines, to facilitate comparison of the velocity differentials of the various tracers. CO(2-1) displays the largest velocity differential, followed by the K-band gas tracers, and finally the stars. This is interpreted as arising due to the different depths probed by the various tracers.
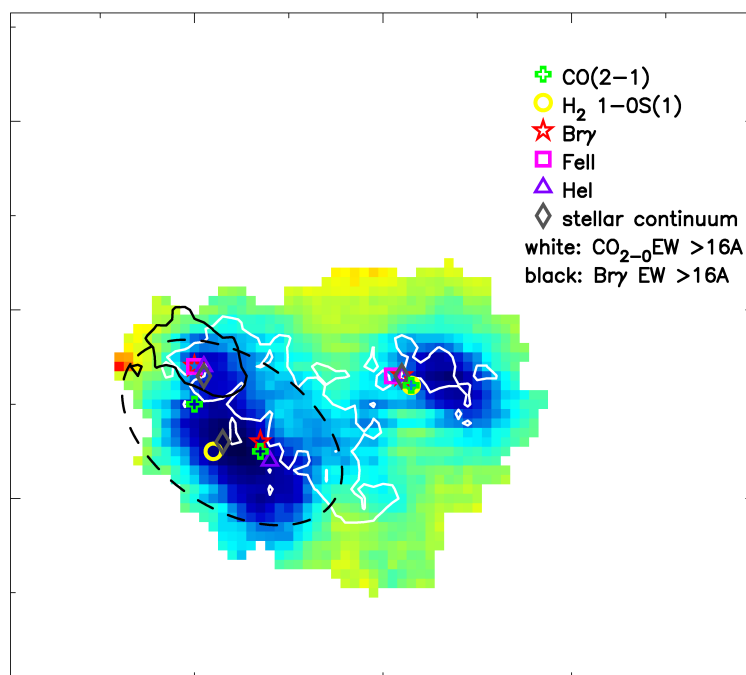
Figure 5.16: Extinction map (cf. Fig. 5.9), with the emission peaks of the various tracers, and the regions of high $EW_{Br\gamma}$ ($> 16\,\text{Å}$, black contours) and EW_{CO} ($> 16\,\text{Å}$, white contours). The latter indicate regions with large flux contributions from recent star formation. As can be seen, both the region with lots of recent star formation and the region with high extinction are elongated along the major axis of the CO(2-1) rotation, but offset from each other, with one either side of the major axis. This suggests that we are seeing a thick disk/spheroid embedded in the larger scale gas disk, with the northwestern half above, and the southeastern half below the gas disk; leading to the offset regions of high extinction (nucleus obscured by gas disk) and high star formation (nucleus above disk plane). The black dashed line is a suggested outline of the nucleus.

As outlined in §5.5 & §5.6, the western nucleus is quite compact, whereas the eastern nucleus appears more extended. Scoville et al. (1998) propose that the crescent-like K-band continuum morphology of the western nucleus is due to an embedded opaque dust disk, which absorbs the stellar light from the southern half of the nucleus (their Fig. 6). This is supported by the stellar velocity map presented here (Fig. 5.3), which shows that the stellar rotation field is regular and extends to the proposedly extincted lower half. The embedded dust disk appears limited in extent, since in the Scoville et al. (1998) NICMOS data, emission from the southernmost tip of the western nucleus is visible. Turning to the eastern nucleus, as we argue in §5.6.3, the extinction pattern and EW_{CO} suggest that here we are seeing a more extended spheroid, the south-eastern half of which is more strongly reddened due to being embedded in the larger-scale gas disk. This therefore confirms the picture put forward by Mundell et al. (2001) (cf. their Fig. 7), in which the eastern nucleus is coplanar with the main CO disk, and the western nucleus lies above it.

5.8 Summary

We present new adaptive optics integral field spectroscopy near-infared data, and re-analyse interferometric mm CO(2-1) and continuum emission observations of the prototypical ULIRG Arp 220. Our main conclusions are:

- We show that in the central kpc, a 10 Myr old starburst provides the majority of the K-band luminosity, with a $\gtrsim 1$ Gyr old stellar population accounting for the remainder. There is also a small contribution by stars $\lesssim 8$ Myr old, which are responsible for the Brγ emission.

- The Calzetti et al. (2000) reddening law is found to provide the best fit to photometric data points spanning $0.45\,\mu$m to $2.12\,\mu$m.

- Estimating the system's bolometric luminosity from *IRAS* fluxes, we find that we only see $\sim 7\%$ of the observed (non-reddening corrected) K-band luminosity. Since a reddening correction would only increase the observed flux by a factor ~ 2–3, this implies that there is significant amount of emitted K-band light which is completely obscured.

- Assuming the CO(2-1) emission and the K-band continuum peaks of the western nucleus to coincide, we find that the stellar kinematic centre is coincident with the mm continuum emission peak. This indicates that the mm continuum emission marks the centre of the gravitational potential in which the stars and gas are moving. The CO(2-1) and the stellar kinematics agree well, and all the K-band tracers peak at the same position; this indicates that the western nucleus is a compact, coherent structure.

- The eastern nucleus displays a markedly different morphology. Two emission peaks are seen in CO(2-1). We model the CO(2-1) data as two unresolved sources orbiting around the centre of continuum emission; this produces an excellent match. Comparison of the velocities of the mm and K-band tracers shows that the CO(2-1) has a larger velocity gradient, which is expected since mm observations probe deeper into the obscured nucleus. We therefore conclude that the eastern nucleus also is a coherent structure, albeit more extended than the western nucleus. This, in conjunction with our stellar population analysis, strongly suggests that the nuclei are (remnants of) the progenitors' bulges.

- In general, we agree with the geometry suggested by Mundell et al. (2001), and can refine it further. Comparison of the extinction map, and EW_{CO} and $EW_{Br\gamma}$ maps suggests that the lower half of the eastern nucleus is much more obscured than the upper half. This can plausibly be explained, if the eastern nucleus is coplanar with the larger-scale gas disk, and its lower half is buried in, and hence observed through, this gas disk.

Chapter 6

Conclusions

The aim of this thesis was to investigate major mergers; their posited role in triggering the prodigious luminosities of a class of high-redshift galaxies known as submillimetre-galaxies – and hence, by extension, of the most luminous galaxies in the high-redshift universe –; and the details of the merger process itself, through investigation of the two prototypical nearby major mergers NGC 6240 and Arp 220.

The analysis of near-infrared adaptive optics assisted integral field spectroscopy data and millimetre-wavelength CO line emission interferometry data has allowed us to obtain important scientific results pertaining to these issues, which are summarised below.

SMGs

Our analysis of sub-arcsecond resolution interferometric CO line observations of 12 SMGs yielded the following results:

- SMG size measurements (Gaussian FWHM) from radio and CO fluxes are both consistent with diameters ~ 5 kpc.

- Morphologically, SMGs are either early-stage mergers – in most cases, binaries –, or compact, rotating systems which could be either isolated disk galaxies or coalesced merger products.

- Our data indicate that the binary SMGs are *major* mergers; the mass ratios of the four systems for which we can measure individual masses for each component all have mass ratios of 1:3 or closer, within the errors.

- The majority ($\sim 64\%$) of local infrared-luminosity-selected major mergers (ULIRGs) are coalesced or have nuclear separations ≤ 2 kpc. This suggests that the large fraction of binary SMGs in our sample also implies a major merger origin for at least some of the compact/coalesced SMGs. Due to the uncertain difference in merger stage sampling of $L_{IR} \geq 10^{12} L_{\odot}$ and $S_{850\mu m} \geq 5$ mJy selection, we can

only estimate the corresponding ratio of binary/coalesced mergers expected in our SMG sample. However, even very conservative assumptions indicate that *at most* 3 of the 7 compact/coalesced sources in our sample could plausibly be isolated disk galaxies, rather than end-stage major mergers. Their very large inferred mass densities further support a merger interpretation.

- Our gas and dynamical mass estimates are physically consistent with the lower end of the range of stellar masses in the literature, those of Hainline (2008) adjusted to a Chabrier (2003) IMF. This supports hierarchical merger models, whereas it disfavours cold accretion flow models of SMG formation.

In recent years, research into galaxy evolution at high redshifts has become a key area of research, with new state-of-the-art instruments allowing detailed observations of these distant early galaxies. High-resolution observations of large samples of optically-selected galaxies (e.g. Förster-Schreiber et al. 2009; these have generally lower luminosities than the SMGs discussed here, and hence represent the lower-luminosity bulk of the galaxy population) have uncovered many intriguing phenomena – such as large fractions of galaxies with clumpy, turbulent disks – which we are only beginning to understand. Deep, high-resolution follow-up observations of prototypical examples may be the best way forward to help us understand the physics behind these observations, and to ultimately lead to a coherent picture of high-redshift galaxy evolution. The above results constitute a key stepping stone towards the goal of understanding the processes at work when the universe was about half its current age: we have been able to show that the most luminous high-redshift galaxies are major mergers.

NGC 6240

Our main conclusions from the analysis of new adaptive optics integral field spectroscopy near-IR data and CO(2-1) interferometric line observations of the nearby merger system NGC 6240 are:

- The Calzetti et al. (2000) reddening law provides the best fit to photometric data points between 0.45μm and 2.22μm. The spatially resolved extinction is generally moderate, with $A_K \sim 2$–4.

- The stellar kinematic centres are consistent with the black hole locations proposed by Max et al. (2007).

- The localised increase in the stellar velocity dispersion plausibly is caused by an additional stellar population along the line of sight perturbing the velocity field of the southern nucleus.

- Jeans modelling of the stellar kinematics yields $M = 2.5 \times 10^9 M_\odot$ and $M/L_K = 5.0\,M_\odot/L_\odot$ for the northern nucleus (out to $250\,\mathrm{pc}$), and $M = 1.9 \times 10^{10}\,M_\odot$ and $M/L_K = 5.0\,M_\odot/L_\odot$ for the southern nucleus (out to $320\,\mathrm{pc}$).

- The presence of tidal arms, and the still-separated nuclei indicate that NGC 6240 must be between first encounter and final coalescence. The stellar velocity field, and strength and prominence of the tidal arms indicate that the merger geometry is not perfectly, but reasonably close to prograde coplanar.

- The observed peak of CO(2-1) emission between the nuclei is vexing. Since only perfectly prograde coplanar mergers can produce a pronounced gas bridge between the two merging galaxies, effects such as spatial differences in CO-to-H_2 conversion factor or CO abundance are needed to explain this.

- Star formation histories from numerical simulations display generic features. We use two star formation histories from numerical simulations, in combination with our constraints on the merger stage and measurements of $EW_{Br\gamma}$, to calculate the properties of the young starburst population. We find that recent star formation accounts for only about 1/3 of the total K-band luminosity. Thus the stellar luminosity is dominated by stars predating the merger.

- We discuss the implications of adopting different star formation histories. Whereas the differences between the starburst properties inferred from our two different merger star formation histories are markedly small, adopting a constant star formation rate yields very different results. We conclude that, when characterising the star formation properties of a merger, a 'generic' merger star formation history should be adopted in preference to either instantaneous or constant star formation histories.

- After accounting for the recent star formation, the mass-to-light ratios of the remaining stellar population are $5.2\,M_\odot/L_\odot$ and $1.8\,M_\odot/L_\odot$ for the northern and southern nuclei respectively. This implies that a population of stars older than $\sim 1\,\mathrm{Gyr}$ contributes the majority of the nuclear stellar masses and luminosities. Combined with the measured size and V/σ, as well as results from the simulations, it implies that the two nuclei are the remnants of the bulges of the progenitor galaxies.

Arp 220

As with NGC 6240, we utilise adaptive optics integral field spectroscopy near-IR, and CO(2-1) interferometric line data to investigate this nearby major merger. In particular, our findings are:

- A $\sim 10\,\text{Myr}$ old quickly decaying starburst contributes at least $\sim 50\%$ of the K-band luminosity. Combining the unaccounted-for luminosity with an estimate of the dynamical mass of the western nucleus indicates that the remainder is most likely due to a population $\gtrsim 1\,\text{Gyr}$ old.

- The Calzetti et al. (2000) reddening law is found to provide the best fit to photometric data points spanning $0.45\,\mu\text{m}$ to $2.12\,\mu\text{m}$.

- Arp 220 is severely affected by extinction in the K-band. Comparison of the K-band luminosity with what is expected from far-infrared luminosity measurements shows that in the near-infrared we are only seeing less than 10% of the actually emitted stellar light. This implies that there is a significant amount of emitted K-band light which is completely obscured.

- In the western nucleus, the kinematic centre of the stellar and CO(2-1) kinematics is coincident with the hot dust emission posited to be the signature of an accreting central black hole. The eastern nucleus appears to be more severely affected by extinction effects – different K-band tracers display different morphologies and, to an extent, kinematics. Its interpretation from the K-band observations is thus difficult. However, mm-wavelength CO(2-1) data of the eastern nucleus, probing much deeper than near-infrared observations, are found to be best fitted by two unresolved compact sources rotating around localised hot dust emission, akin to the western nucleus. We therefore interpret the eastern nucleus also as a gravitationally bound structure. Therefore, we conclude that the nuclei are remnants of the progenitor galaxies' bulges, similar to what we find for NGC 6240.

- In general, we agree with the geometry suggested by Mundell et al. (2001), and can refine it further. Comparison of the extinction map, and EW_{CO} and $\text{EW}_{Br\gamma}$ maps suggests that the lower half of the eastern nucleus is much more obscured than the upper half. This can plausibly be explained, if the eastern nucleus is coplanar with the larger-scale gas disk, and its lower half is buried in, and hence observed through, this gas disk.

Bringing together our individual results for these two prototypical major mergers, we can infer a number of things. It is now clear that the bulges of the progenitors have at most their outer layers stripped off in the earlier stages of merging, but generally survive as gravitationally bound structures well into the advanced merger stages. Arp 220 is most likely just beyond the peak of the merger-induced star formation activity – at least half its luminosity is emitted from a $\sim 10\,\text{Myr}$ old starburst. NGC 6240 on the other hand has yet to experience this big starburst; currently only about a third of its luminosity is due to recent star formation. This implies that the

most pronounced peak in the merger-induced star formation, which from simulations is expected to occur at the 'final coalescence' of the two nuclei, in fact more likely occurs when the nuclei are close to, but not yet merged. Our analysis of the stellar populations makes clear that even in a 'starburst'-galaxy, the old stellar populations still contribute a significant, or even dominant, fraction of the total stellar luminosity and mass.

It has also become clear that even near-infrared observations may not probe deeply into these gas-rich mergers; in NGC 6240 we likely see to significant depths, but in Arp 220 extinction and obscuration impose severe limits. The Calzetti et al. (2000) reddening law is the appropriate formalism to use for both systems; resembling screen extinction at short, and mixed extinction at long wavelengths. At moderate levels of extinction, this transition occurs between near-infrared and optical; at higher levels it moves beyond the near-infrared.

It has long been recognised that major mergers are a key mechanism of galaxy evolution. As we have shown, this is also true for galaxies in the early universe. Our in-depth study of two prototypical nearby major mergers has furthered our understanding of the details of the merger process. One of the next logical steps from the second half of this work would be an in-depth investigation of post-coalescence mergers – in particular, searching for signatures of posited feedback mechanisms –, and a quantification of the AGN content of pre-, current, and post-merger systems through a comprehensive sample; to understand the interplay between, and temporal sequence of, black hole accretion and star formation, and the exact nature and workings of the feedback processes terminating each. Such causalities gleaned from nearby systems would doubtless also enhance our understanding of high-z galaxy evolution processes, if the limitations to the validity of such transfers (e.g. differing gas fractions) were carefully kept in mind.

As with many areas of astrophysics, progress in this field has to a large extent been instrumentation-driven – it is only through the utilisation of state-of-the-art instrumentation and telescopes that this work has been possible. As Arp 220 exemplifies, longer wavelength observations (probing deeper into dust-obscured systems) are needed; however beyond $\sim 5\,\mu$m ground-based sensitivity is poor – in this regard, the 0.6–5 μm IFU (0.1″ sampling) on the *James Webb Space Telescope* is one of the exciting instruments going online in the near future. Technological advancement will continue to drive scientific progress, in particular in the field of high-redshift galaxy evolution; higher resolution observations e.g. will allow a more detailed understanding of disk creation and the vexing clumps seen in current observations. Generally, here the emphasis will be on understanding the lower-luminosity galaxies making up the bulk of the stellar mass and luminosity, and the processes governing secular evolution.

Exciting developments are also taking place in the field of numerical simulations of galaxy interactions, with radiative transfer codes beginning to enable a more direct comparison between observations and simulations (statistical comparisons of samples being arguably the most promising way forward, in order to achieve coverage of the

large merger parameter space, and due to the excessively time-consuming process of producing exact simulation matches of prototypical example observations). However, the skilled analysis and interpretation of observational data will remain the mainstay of progress towards a coherent picture of how galaxies interact and evolve through the aeons.

Bibliography

Abuter R., et al., 2006, NewAR, 50, 398

Adelberger M. G., et al., 2004, ApJ, 607, 226

Agüero E. L., Díaz R. J., Paolantonio S., 2001, PASP, 113, 1515

Alexander D. M., et al., 2005, ApJ, 632, 736

Alexander D. M., et al., 2008, AJ, 135, 1968

Alonso-Herrero A., et al., 2006, ApJ, 650, 835

Aretxaga I., et al., 2007, MNRAS, 379, 1571

Armus L., Heckman T. M., Miley G. K., 1990, ApJ, 364, 471

Armus L., et al., 2006, ApJ, 640, 204

Arp H., 1966, ApJS, 14, 1

Bahcall N. A., et al., 2003, ApJ, 585, 182

Bahcall N. A., Bode P., 2003, ApJ, 588, 1

Barnes J. E., 1988, ApJ, 331, 699

Barnes J. E., 1992, ApJ, 393, 484

Barnes J. E., Hernquist L., 1992, ARA&A, 30, 705

Barnes J. E., Hernquist L., 1996, ApJ, 471, 115

Barnes J. E., 2002, MNRAS, 333, 481

Bastian N., Covey K. R., Meyer M. R., 2010, arXiv1001.2965

Bell E. F., et al., 2006, ApJ, 652, 270

Bell E. F., 2008, ApJ, 680, 295

Bender R., Burstein D., Faber, S. M., 1992, ApJ, 399, 462

Benson A. J., Bower R., 2010, arXiv1004.1162

Beswick R., Pedlar A., Mundell C., Gallimore J., 2001, MNRAS, 325, 151

Biggs A. D., Ivison R. J., 2008, MNRAS, 385, 893

Binney J., Tremaine S., 1987, Galactic Dynamics, Princeton University Press, Princeton

Binney J., Tremaine S., 2008, Galactic Dynamics: Second Edition, Princeton University Press, Princeton

Birnboim Y., Dekel A., 2003, MNRAS, 345, 349

Blain A. W., et al., 2002, Phys. Rep., 369, 111

Bland-Hawthorn J., Wilson A. S., Tully R. B., 1991, ApJ, 371, L19

Blumenthal G. R., et al,, 1984, Nature, 311, 517

Boger G., Sternberg A., 2005, ApJ, 632, 302

Boggess N. W., et al., 1992, ApJ, 397, 420

Bonacini Calia et al., 2006, in *Advances in Adaptive Optics II*, eds Ellerbroek B., Bonaccini Calia D., Proc. SPIE, 6272, 627207

Bondi H., Hoyle F., 1944, MNRAS, 104, 273

Bonnet H., et al., 2004, The ESO Messenger, 117, 17

Borys C., et al., 2005, ApJ, 635, 134

Bothwell M. S., et al., 2010, MNRAS, 405, 219

Bournaud F., Duc P.-A., Emsellem E., 2008, MNRAS, 389, 8

Braine J., Davoust E., Zhu M., Lisenfeld U., Motch C., Seaquist E., 2003, A&A, 408, L13

Brandl B. R., et al., 2009, ApJ, 699, 1982

Brinchmann J., Ellis R. S., 2000, ApJ, 536, 77

Bundy K., Ellis R. S., Conselice C. J., 2005, ApJ, 625, 621

Calzetti D., et al., 2000, ApJ, 533, 682

Canalizo G., Stockton A., 2001, ApJ, 555, 719

Cappellari M., Copin Y., 2003, MNRAS, 342, 345

Cappellari M., et al., 2009, ApJ, 704, 34

Cappellari M., et al., 2009, MNRAS, 394, 660

Caputi K. I., et al., 2007, ApJ, 660, 97

Casey C. M., et al., 2009a, MNRAS, 399, 121

Casey C. M., et al., 2009b, arXiv0910.5756

Casoli F., Dupraz C., Combes F., 1992, A&A, 264, 55

Chabrier G., 2003, ApJ, 586, 133

Chapman S. C., et al., 2003, Nature, 422, 695

Chapman S. C., et al., 2004, ApJ, 611, 732

Chapman S. C., et al., 2005, ApJ, 622, 772

Chary R., Elbaz D., 2001, ApJ, 556, 562

Clements D. L., et al., 1996, MNRAS, 279, 477

Clements D. L., et al., 2002, ApJ, 581, 974

Colberg J. M., et al., 2000, MNRAS, 319, 209

Colbert D. T., et al., 1994, ApJ, 436, 89

Cole S., et al., 2000, MNRAS, 319, 168

Condon J. J. & Yin Q. F., 1990, ApJ, 357, 97

Condon J. J., 1992, ARA&A, 30, 575

Conselice C. J., 2003, ApJS, 147, 1

Conselice C. J., Rajgor S., Myers R., 2008, MNRAS, 386, 909

Coppin K., et al., 2006, MNRAS, 372, 1621

Cowie L. L., Barger A. J., Kneib J. P., 2002, AJ, 123, 2197

Cox T., Jonsson P., Primack J., Somerville R., 2006, MNRAS, 373, 1013

Cox T., et al., 2008, MNRAS, 384, 386

Cram L. E., 1998, ApJ, 506, 85

Cresci G., et al., 2009, ApJ, 697, 115

Daddi E., et al., 2004a, ApJ, 617, 746

Daddi E., et al., 2004b, ApJ, 600, L127

Daddi E., et al., 2007, ApJ, 670, 156

Daddi E., et al., 2010, ApJ, 713, 686

Danielson A. L. R., et al., 2010, arXiv1008.3183

Dasyra K. M., et al., 2006a, ApJ, 638, 745

Dasyra K. M., et al., 2006b, ApJ, 651, 835

Dasyra K. M., et al., 2008, ApJ, 680, 232

Davé R., et al., 2010, MNRAS.404.1355

Davis M., et al., 1985, ApJ, 292, 371

Davies R. I., et al., 2003, ApJ, 597, 907

Davies R. I., et al., 2005, ApJ, 633, 105

Davies R. I., et al., 2006, ApJ, 646, 754

Davies R. I., 2007, MNRAS, 375, 1099

Davies R. I., et al., 2007, ApJ, 671, 1388

Davies R. I., 2008a, in *The 2007 ESO Instrument Calibration Workshop*, eds Kaufer
   A., Kerber F., (Springer-Verlag Berlin Heidelberg), p. 249

Davies R. I., 2008b, ESO Messenger, vol. 131, p. 7-10

Dejonghe H., 1986, PhR, 133, 217

Dekel A., Sari R., Ceverino D., 2009, ApJ, 703, 785

Di Matteo T., Springel V., Hernquist L., 2005, Nature, 433, 604

Di Matteo P., et al., 2007, A&A, 468, 61

Di Matteo P., et al., 2008, A&A, 492, 31

Djorgovski S., Davis M., 1987, ApJ, 313, 59

Downes D., Solomon P. M., 1998, ApJ, 507, 615

Downes D., Solomon P. M., 2003, ApJ, 582, 37

Downes D., Eckhart A., 2007, A&A, 468, 57

Doyon R., et al., 1994, ApJ, 437, 23

Drilling J., Landolt A., 2000, in *Allen's Astrophysical Quantities*, ed Cox A., (4th ed.; Berlin: Springer)

Dunkley J., et al., 2009, ApJS, 180, 306

Dwek E., et al., 1998, ApJ, 508, 106

Einstein A., 1915, *Sitzungsberichte der Koeniglich-Preussischen Akademie der Wissenschaften zu Berlin*, 844

Einstein A., 1917, *Sitzungsberichte der Koeniglich-Preussischen Akademie der Wissenschaften zu Berlin*, 142

Eisenstein D. J., et al., 2005, ApJ, 633, 560

Eisenhauer F., et al., 2003, in Instrument Design and Performance for Optical/Infrared Ground-based Telescopes, eds Masanori I., Moorwood A., Proc. SPIE, 4841, 1548

Elbaz D., et al., 2007, A&A, 468, 33

Elmegreen D. B., et al., 2007, ApJ, 658, 763

Engel H., et al., 2010a, A&A, in press

Engel H., et al., 2010b, ApJ, in press

Fakhouri O., Ma C.-P., 2008, MNRAS, 386, 577

Falcon-Barroso J., et al., 2006, MNRAS, 369, 529

Fall S. M., 1979, Nature, 281, 200

Fall S. M., Efstathiou G., 1980, MNRAS, 193, 189

Ferrarese L., Merritt D., 2000, ApJ, 539, 9

Förster-Schreiber N., 2000, AJ, 120, 2089

Förster-Schreiber N., et al., 2003, ApJ, 599, 193

Förster-Schreiber N., et al., 2006, ApJ, 645, 1062

Förster-Schreiber N., et al., 2009, ApJ, 706, 1364

Frayer D. T., et al., 2008, ApJ, 680, 21

Frieman J. A., Turner M. S., Huterer D., 2008, ARA&A, 46, 385

Gallimore J. F., Beswick R., 2004, AJ, 127, 239

Gebhardt K., et al., 2000, ApJ, 539, 13

Genzel R., Lutz D., Tacconi L. J., 1998a, Nature, 395, 859

Genzel R., et al., 1998b, ApJ, 498, 579

Genzel R., Cesarsky C. J., 2000, ARA&A, 38, 761

Genzel R., et al., 2001, ApJ, 563, 527

Genzel R., et al., 2003, ApJ, 584, 633

Genzel R., et al., 2006, Nature, 442, 786

Genzel R., et al., 2008, ApJ, 687, 59

Genzel R., et al., 2010, MNRAS.tmp.1296

Gerssen J., et al., 2004, AJ, 127, 75

Gladders M. D., et al., 2007, ApJ, 655, 128

Graham A. W., Worley, C. C., 2008, MNRAS, 388, 1708

Grazian A., et al., 2007, A&A, 465, 393

Greve T. R., et al., 2004, MNRAS, 354, 779

Greve T. R., et al., 2005, MNRAS, 359, 1165

Greve T. R., et al., 2009, ApJ, 692, 1432

Guilloteau S., et al., 1992, A&A, 262, 624

Häring N. & Rix H.-W., 2004, ApJ, 604, 89

Häring-Neumayer N., et al., 2006, ApJ, 643, 226

Hainline L. J., 2006, ApJ, 650, 614

Hainline L. J., 2008, Caltech Ph.D. Thesis

Hainline L. J., et al., 2009, ApJ, 699, 1610

Hainline L. J., et al., 2010, arXiv.1006.0238

Hauser M. G., et al., 1998, ApJ, 508, 25

Heckman T. M., Armus L., Miley G. K., 1987, AJ, 93, 276

Heckman T. M., Armus L., Miley G. K., 1990, ApJS, 74, 833

Heckman T. M., et al., 1996, ApJ, 457, 616

Hernquist L., 1990, ApJ, 356, 359

Hernquist L., Barnes J. E., 1991, Nature, 354, 210

Hernquist L, Spergel D. N., 1992, ApJ, 399, 117

Hernquist, L., 1993, ApJ, 409, 548

Hibbard J. E., Mihos J. C., 1995, AJ, 110, 140

Hibbard J. E., Vacca W. D., Yun M. S., 2000, AJ, 119, 1130

Hicks E. K. S., et al., 2009, ApJ, 696, 448

Ho L. C., 2008, ARA&A, 46, 475

Hogbom J., Brouw W., 1974, A&A, 33, 289

Holland W. S., et al., 1999, MNRAS, 303, 659

Hopkins A. M., 2004, ApJ, 615, 209

Hopkins A. M., Beacom J. F., 2006, ApJ, 651, 142

Hopkins P. F., et al., 2006, ApJS, 163, 1

Hopkins P. F., et al., 2008a, ApJS, 175, 356

Hopkins P. F., et al., 2008b, ApJS, 175, 390

Ikebe Y., et al., 2000, MNRAS, 316, 433

Ivison R. J., et al., 2002, MNRAS, 337, 1

Ivison R. J., et al., 2007, MNRAS, 380, 199

Ivison R. J., et al., 2010, MNRAS, 404, 198

Iwasawa K., et al., 2001, MNRAS, 326, 894

Iwasawa K., et al., 2005, MNRAS, 357, 565

Jahnke K., Kuhlbrodt B., Wisotzki L., 2004, MNRAS, 352, 399

Jesseit R., et al., 2007, MNRAS, 376, 997

Jogee S., 2004, in Alloin D., Johnson R., Lira P., eds, AGN physics on All Scales,
    Springer, Berlin, ch.6

Johansson P. H., Naab T., Burkert A., 2009, ApJ, 690, 802

Joseph R. D., Wright G. S., Wade R., 1984, Nature, 311, 132

Joseph R. D., Wright G. S., 1985, MNRAS, 214, 87

Karl S. J., et al., 2008, AN, 329, 1042K

Karl S. J., et al., 2010, ApJ, 715, 88

Kauffmann G., White S. D. M., Guiderdoni B., 1993, MNRAS, 264, 201

Kauffmann G., White S. D. M., 1993, MNRAS 261, 921

Kauffmann G., et al., 2003, MNRAS, 341, 54

Kauffmann G., et al., 2003b, MNRAS, 346, 1055

Kerěs D., et al., 2005, MNRAS, 363, 2

Kesser M. F., et al., 1996, A&A, 315, 27

Khochfar S., Burkert A., 2006, A&A, 445, 403

Kim D.-C., Sanders D. B., 1998, APJS, 119, 41

Kim D.-C., Veilleux S., Sanders D. B., 2002, ApJS, 143, 277

Kleinmann S., Hall D., 1986, ApJS, 62, 501

Knierman, K. A., et al., 2003, AJ, 126, 1227

Kolmogorov A. N., 1941, *Comptes rendus (Doklady) de l'Académie des Sci-
    ences de l'U.R.S.S.*, 30, 301

Komatsu E., et al., 2009, ApJS, 180, 330

Komossa S., Schulz H., Greiner J., 1998, A&A, 334, 110

Komossa S., et al., 2003, ApJ, 582, L15

Kormendy J., Illingworth G., 1982, ApJ, 256, 460

Kormendy J., 1987, in *Nearly Normal Galaxies*, ed Faber S. M., (Springer-Verlag, New York), p. 163

Kormendy J., Sanders D. B., 1992, ApJ, 390, 53

Kormendy J., Richstone D., 1995, ARA&A, 33, 581

Kormendy J. & Kennicutt, R. C., 2004, ARA&A, 42, 603

Kormendy J., et al., 2009, ApJS, 182, 216

Krajnovic D., et al., 2006, MNRAS, 366, 787

Kreysa E., et al., 1998, SPIE, 3357, 319

Kroupa P., 2001, MNRAS, 322, 231

Lagache G., et al., 1999, A&A, 344, 322

Lagache G., Dole H., Puget J.-L., 2003, MNRAS, 338, 555

Landini M., et al, 1984, A&A, 134, 284

Le Floc'h E., et al., 2005, ApJ, 632, 169

Lester D., Harvey P., Carr J., 1988, ApJ, 329, 641

Lester D. F. & Gaffney N. I., 1994, ApJ, 431, 13

Lonsdale C. J., et al., 2006, ApJ, 647, 185

Lotz J. M., et al., 2006, ApJ, 636, 592

Lutz D., et al., 1996, A&A, 315, 269

Lutz D., et al., 1998, ApJ, 505, 103

Lutz D., et al., 2003, A&A, 409, 867

Lutz D., et al., 2005, ApJ, 632, 13

Magnelli B., et al., 2009, A&A, 496, 57

Magnelli B., et al., 2010, A&A, 518, 28

Magorrian J., et al., 1998, AJ, 115, 2285

Maiolino R., et al., 2007, A&A, 468, 979

Maller A. H., et al., 2006, ApJ, 647, 763

Mamon G. A., Boué G., 2010, MNRAS, 401, 2433

Marconi A., Hunt L. K., 2003, ApJ, 589, 21

Max C. E., et al., 2005, ApJ, 621, 738

Max C. E., Canalizo, G., de Vries W. H., 2007, Science, 316, 1877

Mazure A., Capelato H. V., 2002, A&A, 383, 384

McDowell J. C., et al., 2003, ApJ, 591, 154

McLure R. J., Dunlop J. S., 2002, MNRAS, 331, 795

Medling A., et al., in preparation

Melnick J., Mirabel I. F., 1990 A&A, 231, 19

Menéndez-Delmestre K., et al., 2009, ApJ, 699, 667

Michałowski M. J., Hjorth J., Watson D., 2010, A&A, 514, 67

Mihos J. C., Hernquist L., 1994, ApJ, 437, 47

Mihos J. C., 1995, ApJ, 438, 75

Mihos J. C., Hernquist L., 1996, ApJ, 464, 641

Mihos J. C., 1999, Ap&SS, 266, 195

Mo H. J., White S. D. M., 1996, MNRAS, 282, 347

Mo H. J., Mao S., White S. D. M., 1998, MNRAS, 295, 319

Moriondo G., Giovanelli R., Haynes M., 1999, A&A, 346, 415

Mueller Sánchez F., et al., 2006, A&A, 454, 481

Mundell C. G., Ferruit P., Pedlar A., 2001, ApJ, 560, 168

Murphy T. W., et al., 1996, AJ, 111, 1025

Murray N., Quataert E., Thompson T. A., 2005, ApJ, 618, 569

Naab T., Burkert A., Hernquist L., 1999, ApJ, 523, 133

Naab T., Burkert A., 2003, ApJ, 597, 893

Naab T., Jesseit R., Burkert A., 2006, MNRAS, 372, 839

Narayanan D., et al., 2009, MNRAS, 400, 1919

Narayanan D., et al., 2010a, MNRAS, 401, 1613

Narayanan D., et al., 2010b, MNRAS.tmp.950

Nardini E., et al., 2010, MNRAS, 405, 2505

Neri R., et al., 2003, ApJ, 597, 113

Netzer H., et al., 2005, ApJ, 629, 739

Netzer H., Trakhtenbrot B., 2007, ApJ, 564, 754

Neugebauer G., et al., 1984, ApJ, 278, 83

Neugebauer G., et al, 1984, Science, 224, 14

Neumayer N., et al., 2007, ApJ, 671, 1329

Newton I., 1687, *Philosophiae Naturalis Principia Mathematica*

Noeske K. G., et al., 2007, ApJ, 660, L43

Ockham W., 1495, in *Quaestiones et decisiones in quattuor libros Sententiarum Petri Lombardi*, ed. Lugd.

Ohyama Y., Yoshida M., Takata T., 2003, AJ, 126, 2291

Origlia L., Moorwood A., Oliva E., 1993, A&A, 280, 536

Parra R., et al., 2007, ApJ, 659, 314

Pasquali A., de Grijs R., Gallagher J., 2003, MNRAS, 345, 161

Pei Y. C., et al., 1999, ApJ, 522, 604

Peletier, R. F., et al., 2007, MNRAS, 379, 445

Percival W. J., et al., 2007, MNRAS, 38, 1053

Perlmutter S., et al., 1999, ApJ, 517, 565

Pollack L., Max C., Schneider G., 2007, ApJ, 660, 288

Pope A., et al., 2005, MNRAS, 358, 149

Pope A., et al, 2008, ApJ, 675, 1171

Press W. H., Schechter P., 1974, ApJ, 187, 425

Puget J.-L., et al., 1996, A&A, 308, 5

Quinn P. J., 1984, ApJ, 279, 596

Rabien S., et al., 2004, in *Advancements in Adaptive Optics*, eds Bonaccini Calia D., Ellerborek B., Ragazzoni R., Proc. SPIE, 5490, 981

Reddy N. A., et al., 2005, ApJ, 633, 748

Rees M. J., Ostriker J. P., 1977, MNRAS, 179, 541

Richstone D., et al., 1998, Nature, 395, 14

Riess A. G., et al, 1998, AJ, 116, 1009

Riess A. G., et al., 2004, ApJ, 607, 665

Riess A. G., et al., 2007, ApJ, 659, 98

Robertson B., et al., 2006, ApJ, 645, 986

Rodríguez Zaurin J., Tadhunter C. N., González Delgado R. M., 2008, MNRAS, 384, 875

Rovilos E., et al., 2005, MNRAS, 359, 827

Rudnick G., et al., 2006, ApJ, 650, 624

Sakamoto K., et al., 1999, ApJS, 124, 403

Sakamoto K., et al., 2008, ApJ, 684, 957

Sakamoto K., et al., 2009, ApJ, 700, 104

Salpeter E. E., 1955, ApJ, 121, 161

Sanders D. B., et al., 1988a, ApJ, 325, 74

Sanders D. B., et al., 1988b, ApJ, 328, L35

Sanders D. B., 1992, in Relationships between active galactic nuclei and starburst galaxies, ed. A. V. Filippenko, ASP Conference Series (ASP: San Francisco), vol. 31, p. 303.

Sanders D. B., Mirabel I. F., 1996, ARA&A, 34, 749

Sanders D. B., et al., 2003, AJ, 126, 1607

Schiminovich D., et al., 2005, ApJ, 619, 47

Schmitt H. R., Bica E., Pastoriza M. G., 1996, MNRAS, 278, 965

Schweizer F., Seitzer P., 1992, AJ, 104, 1039

Scoville N. Z., Yun M. S., Bryant P. M., 1997, ApJ, 484, 702

Scoville N. Z., et al., 1998, ApJ, 492, 107

Semelin B., Combes F., 2002, A&A, 388, 826

Shapiro K. L., et al., 2008, ApJ, 682, 231

Shier, L. M., Fischer, J., 1998, ApJ, 497, 163

Silge J. D., Gebhardt K., 2003, AJ, 125, 2809

Silge J. D., et al., 2005, AJ, 130, 406

Silk J., 1977, ApJ, 211, 638

Smail I. R., Ivison R. J., Blain A. W., Kneib J.-P., 2002, MNRAS, 331, 495

Smail I. R., et al., 2004, ApJ, 616, 71

Smail I. R., Smith G. P., Ivison R. J., 2005, ApJ, 631, 121

Soifer B. T., Neugebauer G., Houck J. R., 1987, ARA&A, 25, 187

Soifer B. T., Neugebauer G., 1991, AJ, 101, 354

Solomon P. M., Downes D., Radford S. J. E., Barrett J. W., 1997, ApJ, 478, 144

Soltan A., 1982, MNRAS, 200, 115

Somerville R. S., et al., 2008, MNRAS, 391, 481

Spergel D. N., et al., 2007, ApJS, 170, 377

Spergel D. N., et al., 2003, ApJS, 148, 175

Spitzer L. Jr., 1987, in Dynamics and Evolution of Globular Clusters, Princeton University Press

Spoon H. W. W., et al., 2004, A&A, 414, 873

Springel V., Di Matteo T., Hernquist L., 2005b, ApJ, 620, 79

Springel V., et al., 2005, Nature, 435, 629

Springel V., Di Matteo T., Hernquist L., 2005, MNRAS, 361, 776

Springel V., 2005, MNRAS, 364, 1105

Steffen A., et al. 2006, AJ, 131, 2826

Steidel C. C., et al., 2004, ApJ, 604, 534

Sternberg A., 1998, ApJ, 506, 721

Sternberg A., Hoffman T., Pauldrach A., 2003, ApJ, 599, 1333

Stewart K .R., et al., 2008, ApJ, 683, 597

Strateva I., et al., 2001, AJ, 122, 1861

Sturm E., et al., 1996, A&A, 315, 133

Sugai H., et al., 1997, ApJ, 481, 186

Swinbank A. M., et al., 2004, ApJ, 617, 64

Swinbank A. M., et al., 2006, MNRAS, 371, 465

Swinbank A. M., et al., 2008, MNRAS, 391, 420

Swinbank A. M., et al., 2010, MNRAS, 405, 234

Tacconi L. J., et al., 1999, ApJ, 524, 732

Tacconi L. J., et al., 2002, ApJ, 580, 73

Tacconi L. J., et al., 2006, ApJ, 640, 228

Tacconi L. J., et al., 2008, ApJ, 680, 246

Tacconi L. J., et al., 2010, Nature, 463, 781

Tecza M., et al., 2000, ApJ, 537, 178

Teyssier R., Chapon D., Bournaud, F., 2010, ApJ, 720, 149

Thomas J., et al., 2004, MNRAS, 353, 391

Thornton K., et al., 1998, ApJ, 500, 95

Tokunaga, A., 2000, in *Allen's Astrophysical Quantities*, ed Cox A., (4th ed.; Berlin: Springer)

Toomre A., Toomre J., 1972, ApJ, 178, 623

Toomre A., 1977, in Tinsley B. M., Larson R. B., eds, Evolution of Galaxies and Stellar Populations, Yale Univ. Obs., New Haven, p.401

Trager S. C., Faber S. M., Worthey G., Gonzalez J. J., 2000, AJ, 120, 165

Tremaine S., et al., 2002, ApJ, 574, 740

Tremonti C. A., Moustakas J., Diamond-Stanic A. M., 2007, ApJ, 663, 77

Valiante E., et al., 2007, ApJ, 660, 1060

Vanden Berk D., et al., 2006, AJ, 131, 84

van der Marel R. P., van Dokkum P. G., 2007, ApJ, 668, 738

van der Werf P. P., et al., 1993, ApJ, 405, 522

Veilleux S., Kim D.-C., Sanders D. B., 2002, ApJS, 143, 315

Veilleux S., et al., 2009, ApJS, 182, 628

Vignati P., et al., 1999, A&A, 349, L57

Vikhlinin A., et al, 2009, ApJ, 692, 1060

Weiss A., 2007, in ASP Conf. Ser. 375, From z-Machines to ALMA: Sub-millimetre-spectroscopy of Galaxies, eds. A. J. Baker et al. (San Francisco: ASP), 25

Werner M. W., et al., 2004, ApJS, 154, 1

Wetzstein M., Naab T., Burkert A., 2007, MNRAS, 375, 805

White S. D. M., Rees M. J., 1978, MNRAS, 183, 341

White S. D. M., Frenk C. S., 1991, ApJ, 379, 52

White S. D. M., et al., 1993, Nature, 366, 429

Whitmore B., McElroy D., Tonry J., 1985, ApJS, 59, 1

Wiedner M. C., et al., 2002, ApJ, 581, 229

Wilson C. D., et al., 2006, ApJ, 641, 763

Winge C., Riffel R. A, Storchi-Bergmann T., 2009, ApJS, 185, 186

Wolf J., et al., 2009, MNRAS, 406, 1220

Woo J.-H., Urry C. M., 2002, ApJ, 579, 530

Wynn-Williams C. G., Becklin E. E., 1993, ApJ, 412, 535

Xu C., 2000, ApJ, 541, 134

Younger J. D., et al., 2008, ApJ, 688, 59

Younger J. D., et al., 2010, MNRAS, 407, 1268

Yun M. S., Hibbard J. E., 2001, in Hibbard J. E., Rupen M., van Gorkom J. H., eds, Gas and Galaxy Evolution, ASP Conference Proceedings, Vol. 240, p.866

Acknowledgements

I'm not entirely sure how I ended up writing a dissertation on far-away ensembles of stars that career about in the vast emptiness of space and occasionally manage to crash into another galaxy. It doesn't seem like the most obvious thing to do, in retrospect. But, here I am, at yet another turning point of the trail, and it is time to reflect and pay homage to the people that walked with me for shorter or longer parts of it. Who offered a guiding hand, inspiration, challenge, friendship, laughter on a rainy day, and all those other little things that make life worth living.

First and foremost, my parents and siblings. For their love and unconditional support. Danke, für alles!

Rüdiger Clausen, for his support and encouragement. Without you, this dissertation wouldn't have been written. Requiescat in pace.

Higgs at CK, for sharing his passion for astronomy, and Nort, for academic challenges and introducing me to the beauty of physics.

My friends at home, making me feel like I'd never left every time I suddenly turned up after having been away for months. From escalating Monday evenings to impromptu beach trips in the Höckmobil, it's been epic.

The Munich crew – Thorti, Payel, Tom&Paula&Damian, Peter, Mario, Fabian & Nicole, Matthias & Steffi, and many more. For getting me out of the 'extragalactic' mindset, fun times, all those 'quiet mid-week nights' that ended at 5am, and many good conversations. And Tom, for all this and for much-needed escapes into and across the Alps in your trusty old Volvo with argentinian punk blasting away the frustration of yet another failed analysis; for adventures from Easy Afternoon to Stromboli.

All the members of the MPE Infrared Group, for your help and for making this a fun place to work at.

Prof. Reinhard Genzel for giving me the opportunity to undertake my doctoral research in his group at MPE.

And of course Ric, for unbridled enthusiasm; for always having or making time for me; for your support and advice, scientific and otherwise.

Thank you all.